Geodesic Theory and Inherent Dynamics of Hard Sphere Liquids

by

Qingqing Ma

M. A., Brown University, 2011

B. S., University of Science and Technology of China, 2009

A Dissertation submitted in partial fulfillment of the
requirements for the Degree of Doctor of Philosophy
in the Department of Chemistry at Brown University

Providence, Rhode Island

May 2015

This dissertation by Qingqing Ma is accepted in its present form
by the Department of Chemistry as satisfying the
dissertation requirement for the degree of Doctor of Philosophy.

Date _____ _____

Richard M. Stratt, Director

Recommended to the Graduate Council

Date _____ _____

Jimmie D. Doll, Reader

Date _____ _____

Robert A. Pelcovits, Reader

Approved by the Graduate Council

Date _____ _____

Peter M. Weber, Dean of the Graduate School

Curriculum Vitæ

Born December 22, 1987, Anqing, Anhui, China

Education

Ph.D.	Theoretical Chemistry, Brown University, Providence, RI, US, 2015
M.A.	Chemistry, Brown University, Providence, RI, US, 2011
B.S.	Chemical Physics, University of Science and Technology of China, Hefei, Anhui, China, 2009

Publications

Qingqing Ma and Richard M. Stratt, *Potential energy landscape and inherent dynamics of a hard-sphere fluid*, Physical Review E, 90(4):042314, October 2014.

Conferences

Richard M. Stratt and Qingqing Ma, *Potential energy landscapes of hard-sphere liquids*, 244^{th} ACS National Meeting, Philadelphia, PA, August, 2012.

Awards

Outstanding Students Scholarship 2005 - 2008

Dedicated to my family

Acknowledgement

I would like to take this opportunity to thank the people who have supported me and inspired me over the years in my graduate life.

First of all, I would like to express my great appreciation to my advisor, Professor Richard Stratt. Professor Stratt is an incredible mentor. He is brilliant, kind, passionate for science. He is the most important person for this work to be done. I cannot thank him enough for being patient with me and allowing me to grow to be a scientist. I have learned a lot from working with him. He exemplifies both consciously and subconsciously how to analyze problems scientifically, how to think in a logical and critical way, how to come up with feasible solutions, how to convey ideas clearly to others. His passion for science also influenced me, for always keeping curiosity and discovering interesting aspects of things. His kindness and humor also brighten up research. It is my honor to have Richard as my graduate advisor. Working with him is a great experience of my life and I will always cherish it.

I also would like to thank Professor Jimmie Doll and Professor Robert Pelcovits for being my committee members, and for taking the time reading my thesis and providing helpful insights and comments. I also thank them for being committee members of my original research proposal.

I also thank my group members Vale-Cofer Shabica, Yan Zhao, Layne Frechette for useful discussions about science and technical issues. I thank Vale for his help in Linux and Latex, and for organizing the group webpage with useful resources. I would like to thank Margaret Doll for maintaining the computer cluster TED and for

helping me whenever I run into problems with TED.

My sincere thanks also go to former group member Chengju Wang for his discussion on the project. I also would like to thank Gengqi Wang for his encouragement for my research. A special thanks to Lian Xiong for his encouragement and support especially during the difficult times.

Last but not least, I would like to thank my family and friends. They have always supported me and are always a source of comfort for me.

Contents

List of Figures

List of Tables

List of Algorithms

Abstract of "Geodesic Theory and Inherent Dynamics of Hard Sphere Liquids"

by Qingqing Ma, Ph.D., Brown University, May 2015

What defines the intrinsic dynamics of liquids? By studying the hard sphere liquids, whose potential energy landscape is so singular that traditional landscape approaches do not apply without approximation, we show that an important topological feature of the potential energy landscape - the geodesic pathways - successfully predicts dynamics of hard sphere liquids, without any coarse-graining or softening the potential. The geodesic pathways quantitatively capture the fast drop of diffusion coefficients upon increasing packing fraction. They also contain other dynamical information such as dynamical heterogeneity. By comparing the geodesics of both hard and soft sphere liquids, we show that the singularity of the potential energy landscape influences the details of the geodesics. There are more to explore about the potential energy landscape than its minima and saddle points. The geodesics define the inherent dynamics of liquids.

Chapter 1

Supercooled Liquids and Potential Energy Landscape

When a liquid is cooled fast enough under certain conditions, instead of becoming crystal, it enters a supercooled phase [1]. A supercooled liquid is a thermodynamically metastable state [1]. Supercooled liquids demonstrate a wide range of dynamical phenomena different from those of normal liquid or solid, such as fast slowing down of dynamics [1], dynamic heterogeneity [1], cooperative regions [1], increasing dynamic correlation length [1]. A deeply supercooled liquid experiences glass transition, the glass transition temperature T_g conventionally defined as the temperature at which the viscosity of the liquid reaches $10^{12}\ Pa{\cdot}s$ upon cooling [1]. Whether glass transition is a pure dynamical event or there is a thermodynamic phase transition underlying is still under research. Although there is not yet any agreed conclusions through extensive research on supercooled liquid by simulation, experiments or theories, the dynamics itself is unique and worth studying.

This chapter introduces briefly the dynamic phenomena of supercooled liquid, then the widely-used potential energy landscape approach for explaining the slowing down of supercooled liquids. After that the chapter introduces the hard sphere liquid and points out the limits of the traditional landscape approach, then proposes a new

approach to studying the dynamics, which is the theme of the thesis.

1.1 Dynamic Phenomena of Supercooled Liquids

1.1.1 Dynamic Slowing Down

The fast slowing down of dynamics is the most common feature of supercooled liquids. Although a supercooled liquid maintains the unordered liquid structure, the dynamics slow down drastically as the temperate decreases. Upon lowering the temperature, the diffusion coefficient drops, the relaxation time increases, the viscosity increases, all by several orders of magnitude, as illustrated in Fig. 1.1.

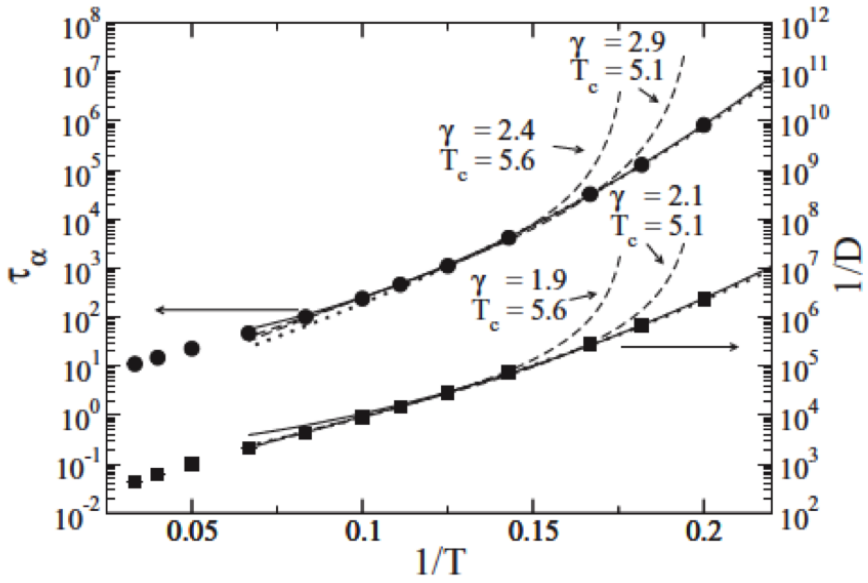

Figure 1.1: Illustration of dynamic slowing down of a glass-forming harmonic sphere liquid. Figure taken from [2]. With decreasing temperature T in a small range, the relaxation time τ_α increases and the diffusion coefficient D decreases, both by several orders of magnitude. The dashed lines are different fitting curves.

The diffusion equation is [1]

$$\frac{\partial \rho(\mathbf{r},t)}{\partial t} = \nabla \cdot [D(\rho,\mathbf{r})\nabla\rho(\mathbf{r},t)] \tag{1.1}$$

where D is the diffusion coefficient, $\rho(\mathbf{r}, t)$ is the density of the diffusing system at position $\mathbf{r}$ and time t.

Assuming D is a constant, diffusion coefficient D has the following relation with particle velocity microscopically [3],

$$D = \frac{1}{3}\int_0^\infty \mathrm{d}t \langle \mathbf{v}_i(t) \cdot \mathbf{v}_i(0) \rangle \tag{1.2}$$

where $\mathbf{v}_i(t)$ is the velocity of the centre of mass of particle i at time t, and $\langle \dots \rangle$ denotes ensemble average.

At long time limits, the Einstein relation holds [3]

$$2tD = \frac{1}{3}\langle |\mathbf{r}_i(t) - \mathbf{r}_i(0)|^2 \rangle \tag{1.3}$$

where $\mathbf{r}_i(t)$ is the position of the centre of mass of particle i at time t. This equation is commonly used in experimental measurement of diffusion coefficients.

1.1.2 Dynamic Heterogeneity

Supercooled liquids demonstrate heterogeneity both structurally and dynamically [4], rather than being homogenous. The particles can be divided into "fast" and "slow" groups by relaxation rates based on their mean square displacements in a given time interval [5]. The mobile particles increase the mobilities of the particles around them, a process termed "dynamic facilitation" [5]. At longer times certain regions of the system tend to have more mobile particles while certain regions have slow particles. These close to each other particles are denoted as clusters [5], as shown in Fig. 1.2.

The non-Gaussian parameter α_2 [7] quantifies how much a distribution of single particle displacements is away from Gaussian.

$$\alpha_2(t) = \frac{3}{5}\frac{\langle \delta r_j^4(t) \rangle}{\langle \delta r_j^2(t) \rangle^2} - 1 \tag{1.4}$$

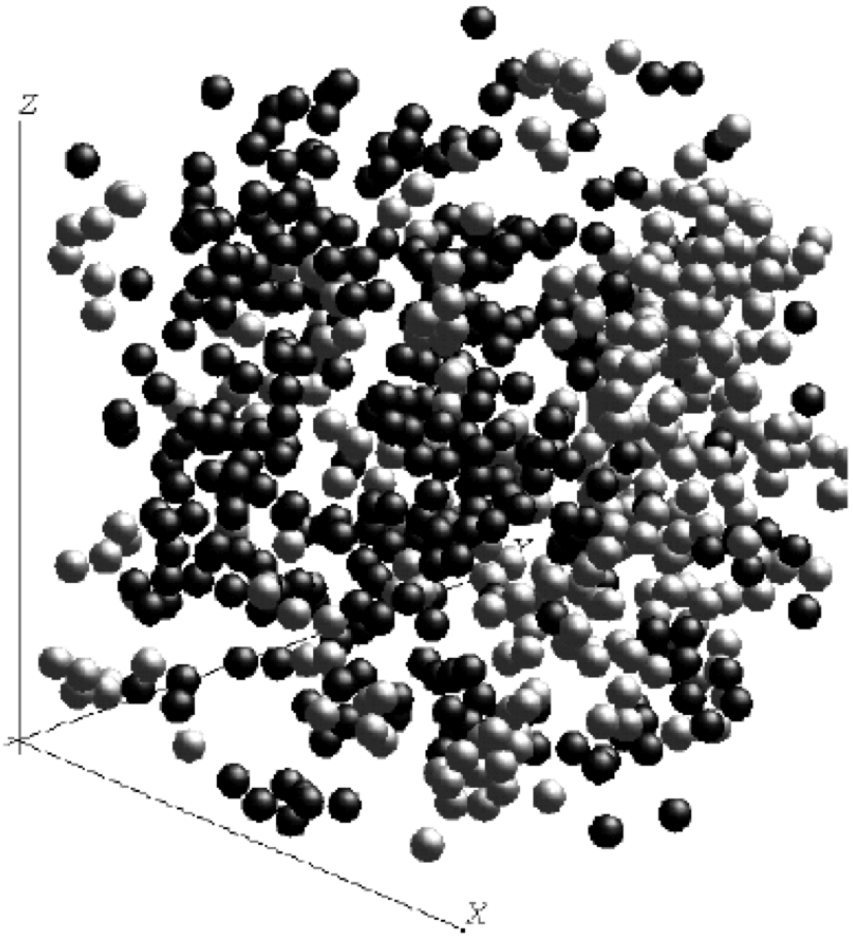

Figure 1.2: Illustration of clusters in a glass-forming Lennard-Jones liquid. Figure taken from [6]. It shows the 5% most mobile particles (light grey) and 5% least mobile particles (dark grey) in a time interval comparable to early α relaxation time. Particles with similar mobility tend to be spatially closer to each other, forming clusters.

where $\delta r(t) = |\mathbf{r}_j(t) - \mathbf{r}_j(0)|$ is the displacement of particle j during time t.

If the distribution of single particle displacements is perfectly Gaussian, $\alpha_2(t) = 0$. The non-zero value of α_2 is correlated with dynamic heterogeneity.

Dynamical heterogeneity is also related to stretched exponential relaxation decay [8] and the breakdown of Stokes-Einstein relation [9].

1.1.3 Growing Length Scale

A length scale can be extracted from the mobility correlation of dynamic facilitation. In computer simulations, the length scale is often determined from the four point

susceptibility $\chi_4(t)$ [10], which characterizes the spatial and temporal correlation of dynamic heterogeneity, as shown in Fig. 1.3.

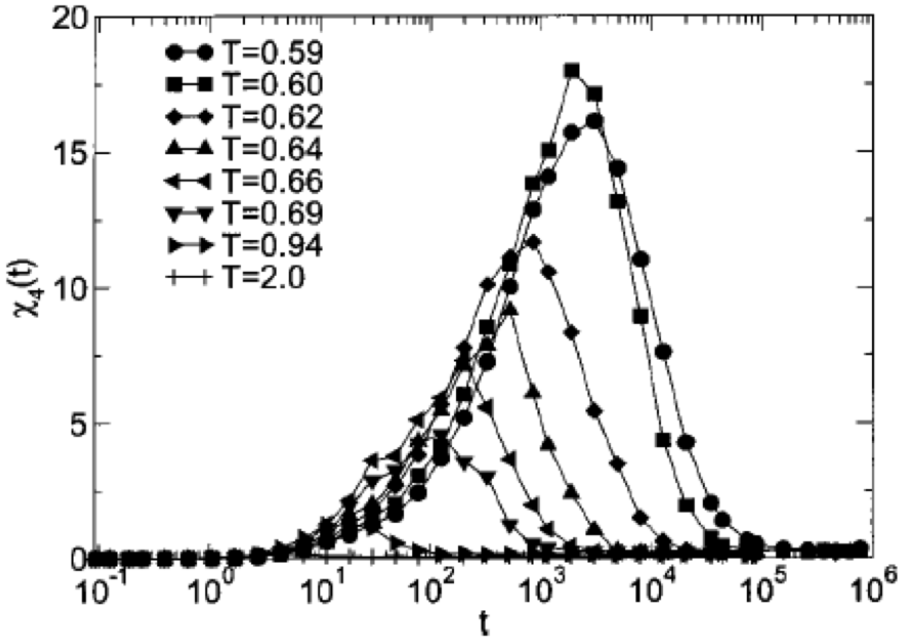

Figure 1.3: Behavior of χ_4 of a binary Lennard-Jones liquid. Each curve describes the dependence of χ_4 on time t at the temperature T. As T lowers, the peak of χ_4 increases monotonically as well as the time t where the peak is, signaling a stronger correlation and a slower decay of dynamics at lower temperatures.

The static correlation length, on the other hand, such as the pair correlation function, does not grow with supercooling [10], as shown in Fig. 1.4.

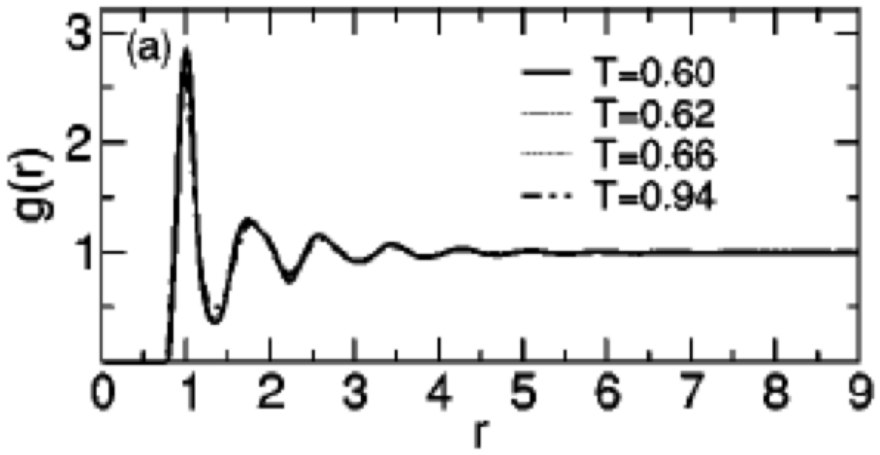

Figure 1.4: Pair correlation function $g(r)$ of a binary Lennard-Jones liquid. It has a weak temperature T dependence.

1.1.4 Cooperative Motion

When the dynamic is very slow, relaxation occurs by cooperative motion of particles. The earliest idea is that of cooperative rearranging regions by Adam and Gibbs [11], defined as the smallest region that can rearrange independently [1]. String motion [12] is the elementary structure of relaxation. An illustration of string motion is given in Fig. 1.5.

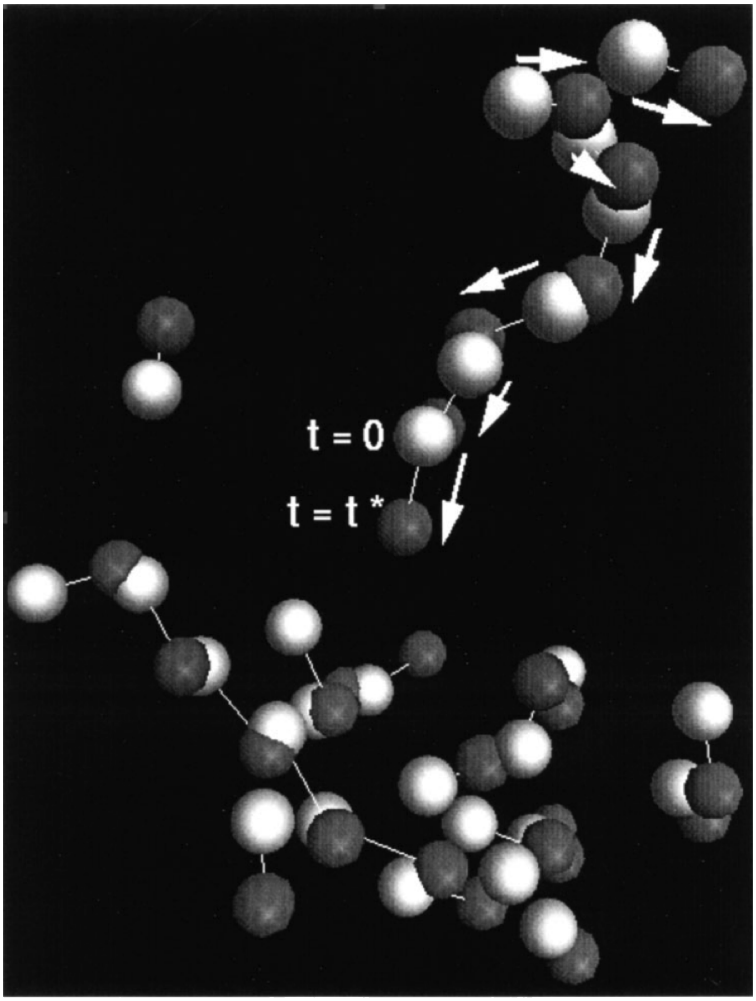

Figure 1.5: String motion of a glass-forming Lennard-Jones liquid. Figure taken from [13]. It shows the positions of the same particles at time 0 (white) and a later time t^* (dark grey), with white segments connecting two positions of the same particle. The white arrows show the movements of some particles.

1.2 Potential Energy Landscape and Dynamics

Many theories attempt to explain one or more of the above phenomena, inherent structure analysis, normal mode analysis, iso-configurational ensemble,mode coupling theory, to name a few. Among them, inherent structure analysis based on potential energy landscape [14] is widely used. A system composed of N particles in Cartesian coordinates has configuration $\mathbf{R}$, which is a $3N$ dimensional vector, and potential energy $V(\mathbf{R})$, which is a scalar function of configuration $\mathbf{R}$. The surface of the function V forms the potential energy landscape.

For a system with continuous potential energy, the Hessian matrix of V defines the local saddle points and minima of the landscape [15]. The inherent structures are the local minima. The landscape can ben seen as a map of basins of inherent structures and barriers between them [16]. A molecular dynamic trajectory can be mapped to a series of inherent structures by finding the nearest inherent structures of selected configurations on the trajectory through steepest descent method on the potential energy [1]. The motion of the system from the point of view of inherent structure is therefore a combination of vibrations around inherent structures and hops over the barrier to another basin of a different inherent structure [1]. The vibrations around inherent structures are seen as "noise" because they do not contribute much to the relaxation. The hopping motion between different inherent structures is the main contribution of dynamics. In the traditional landscape approach, the distribution and characters of inherent structures govern the dynamics [17], and the hopping motion between different inherent structures is considered to be "inherent dynamics" of a liquid.

Fig. 1.6 illustrates the procedure of finding inherent structures and the inherent dynamics of a system.

For a usual liquid at constant pressure, the controlling parameter of dynamics is the temperature T. At high temperature, the system, seen as one point diffusing on the potential energy landscape, has enough energy fluctuation to explore almost freely all the regions of the landscape. Upon decreasing the temperature, the local barriers begin to influence the propagation of the system. The system needs to wait longer times to accumulate enough energy fluctuation in order to overcome barriers to reach to another basin. Further cooling down the system, the motion of the system is confined in some basin within the experimental time frame. The system is said to be out of equilibrium.

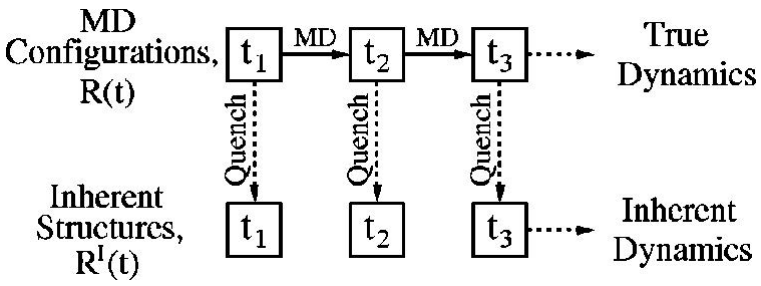

(a)

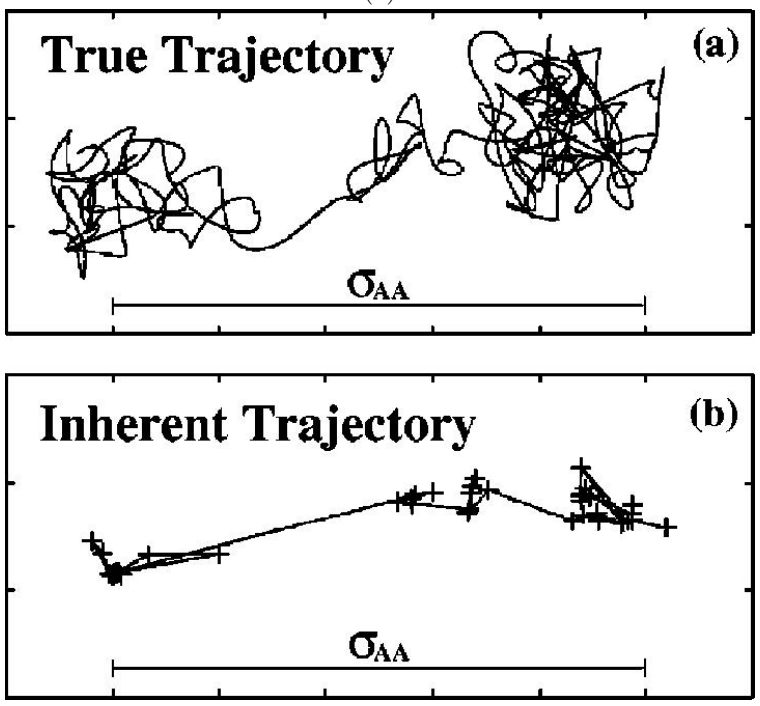

(b)

Figure 1.6: (a) Method of obtaining inherent structures from molecular dynamics trajectory of a glass forming binary Lennard-Jones mixture. Figure taken from [18]. Each selected configurations along MD trajectory is quenched to the corresponding local minima (inherent structure). (b) Inherent dynamics of a glass forming binary Lennard-Jones mixture. Figure taken from [18]. The trajectory of inherent structures excludes the "noise" of molecular dynamics trajectory, revealing inherent dynamics of the system.

1.2.1 Mode Coupling Transition

Mode coupling theory [19] successfully predicts the dynamic slowing down of a system in a certain region $T > T_{MCT}$, where T_{MCT} is the mode coupling temperature. The

decreasing diffusion coefficient D can be fitted by

$$D(T) \propto (T - T_{MCT})^{-\gamma} \tag{1.5}$$

The divergence at $T > T_{MCT}$ is artificial because the original theory does not include activated dynamics [2], which is the main mechanism of relaxation at $T < T_{MCT}$. However, T_{MCT} itself may be the temperature at which the ergodicity of the system is firstly broken [16] - the phase space breaks up into disconnected pieces and the system is confined in one of them .

Other fittings exist, one better than others depends on the temperature range of the system. The Vogel-Fulcher-Tamman law [1] without any theoretical framework fits the relaxation time $\tau(T)$ even for $T_g < T < T_{MCT}$.

$$\tau(T) \propto \exp(\frac{1}{T - T_0}) \tag{1.6}$$

T_0 is close to 0, or at least close to T_g in some systems [1]. The divergence of the relaxation time may be real and indicates a dynamical phase transition [1].

1.3 Hard Sphere Liquid

Hard sphere system is a theoretical model to study liquids. The pair potential energy μ_{ij} between sphere i with diameter σ_i and sphere j with diameter σ_j is defined as

$$\mu_{ij} = \begin{cases} 0 & : r_{ij} \geq \sigma_{ij} \\ \infty & : r_{ij} < \sigma_{ij} \end{cases} \tag{1.7}$$

$$\sigma_{ij} = \frac{1}{2}(\sigma_i + \sigma_j) \tag{1.8}$$

where r_{ij} is the distance between the center of sphere i and the center of sphere j, and σ_{ij} is sum of the radius of sphere i and j.

Hard sphere system is a pure theoretical model. In experiment colloids are often used to mimic the behavior of hard spheres [20]. The controlling parameter for a hard sphere liquid, as the counterpart of temperature T for usual liquid, is the density, usually described in packing fraction ϕ, defined as the fraction of the total volume of the system occupied by all the hard spheres. A system containing N spheres with a total volume V_{box} has a packing fraction

$$\phi = \frac{V_{spheres}}{V_{box}} = \frac{\pi}{6V_{box}} \sum_{i=1}^{N} \sigma_i^3 \tag{1.9}$$

where σ_i is the diameter of sphere i.

1.3.1 Dynamic Phenomena of Hard Sphere Liquids

Hard sphere liquids behave similarly in many ways as usual liquids with continuous potential [21, 22]. The single component hard sphere liquid is a simple liquid that crystalizes easily. It has a freezing point at $\phi_f = 0.49$ [20].

For studying supercooled liquids, a binary hard sphere mixture which does not crystalize easily is widely used. The mixture contains N_b big spheres and N_s small spheres, with number ration $N_b : N_s = 1 : 1$ and diameter ratio $\sigma_b : \sigma_s = 1.4\sigma : \sigma$ [23]. This system exhibits many properties as those of supercooled liquids [24] when ϕ is high, such as dynamic slowing down [24], dynamic heterogeneity [24], growing length scale [24]. The empirical mode coupling transition for the system is $\phi_c = 0.590$ [24].

Both the single component hard sphere liquid and the binary mixture are studied in the thesis.

Fig. 1.7 shows the dynamics slowing down for the binary hard sphere mixture.

Fig. 1.8 and Fig. 1.9 show dynamical heterogeneity for the binary hard sphere mixture.

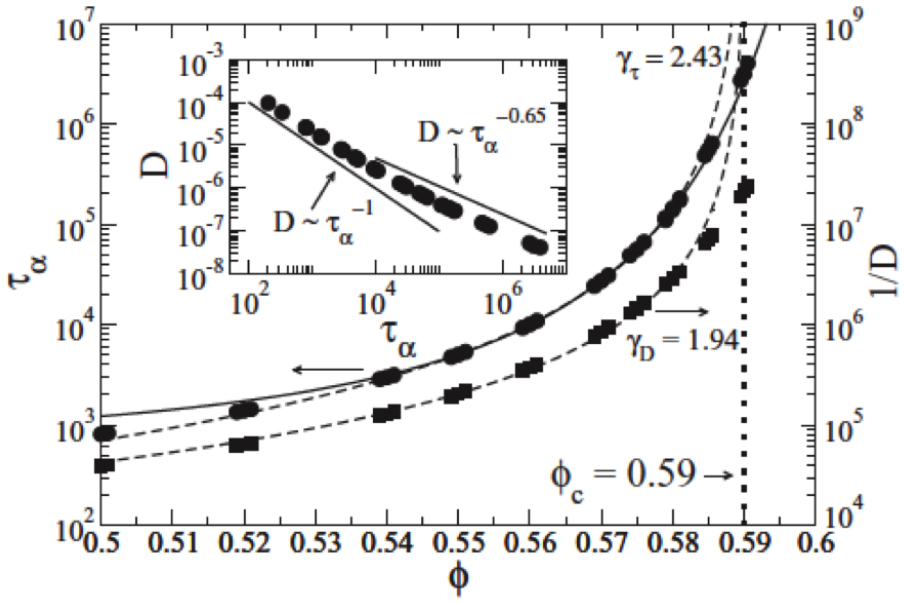

Figure 1.7: Dynamic slowing down of the binary hard sphere liquid. Figure taken from [24]. The diffusion coefficient D drops while the relaxation time τ_α increases both by several orders of magnitude as the density ϕ approaches the mode coupling density $\phi_c = 0.59$. The dashed lines are different fitting curves.

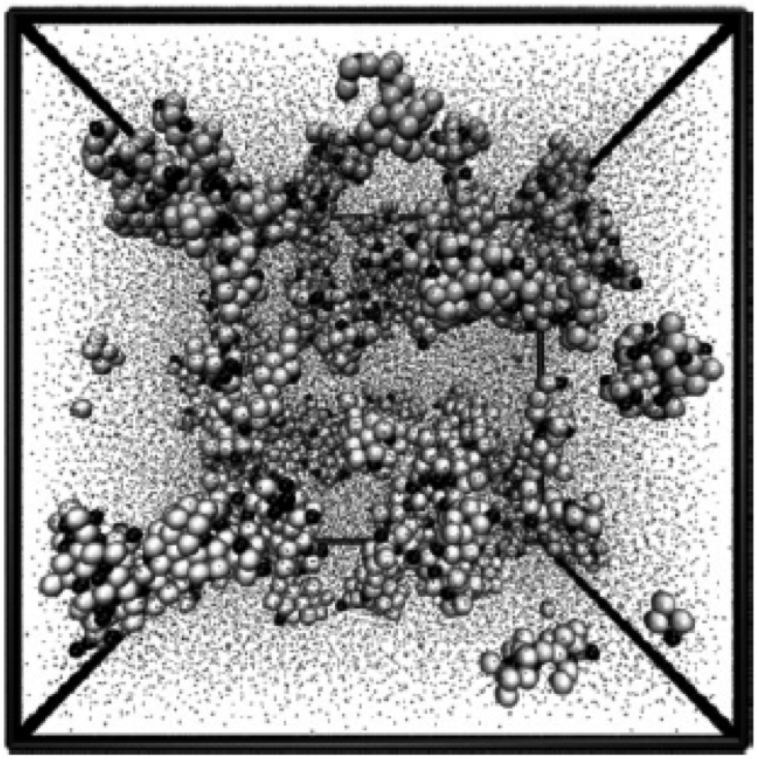

Figure 1.8: Clusters of slow particles of the binary hard sphere liquid. Figure taken from [24]. The white and black spheres are slow particles of the system, with the white representing big particles and the black representing small particles. The rest of particles of the system are the black tiny dots. This figure demonstrates the existence of spatial dynamic heterogeneity in the hard sphere liquid that particles with similar mobilities tend to form clusters.

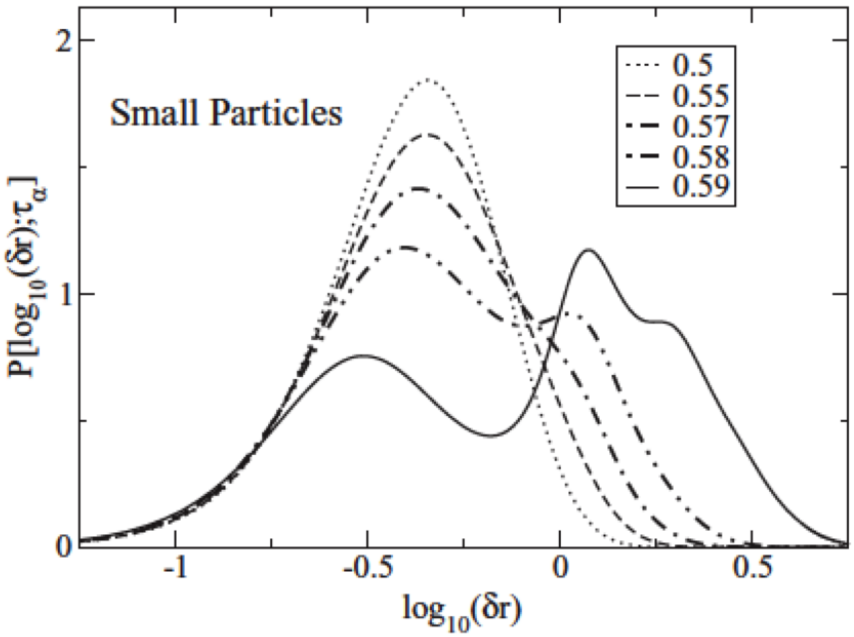

Figure 1.9: The probability density distribution of the logarithm of single particle displacements $\delta(r)$ of small particles during a time interval of relaxation time τ_α of the binary hard sphere liquid. Figure taken from [24]. As the density ϕ increases from 0.5 to 0.59, the distribution gets broader and eventually forms a bimodal shape, showing that there are "slow" and "fast" groups of particles. The figure demonstrates dynamic heterogeneity by showing that there are different subgroups of particles with different mobilities in the system.

1.3.2 Potential Energy Landscape for Hard Sphere Liquids

The traditional analysis of potential energy landscape based on basins and transition barriers is no longer applicable to hard sphere liquids, because of the singularity of the potential energy, which is either 0 or infinity. There is no inherent structures defined as the local minima of the potential energy. One can define a generalized notion of inherent structure of hard sphere liquids as locally jammed packing configuration obtained by compressing the volume of the system [25]. Other methods of analysis can be generalized and applied to hard sphere liquids too. For example, normal mode analysis is applied to hard sphere liquids by defining a fictitious force with information of the momentum exchange per collision and time interval between collisions [26], or by the covariance matrix of displacement [27]. Alternatively, ideas of free energy landscape can be used for hard sphere liquids, in which case the barrier of free energy landscape has a pure entropic origin [28].

But, is there anything the potential energy landscape can tell about dynamics of hard sphere liquids? As hard sphere liquids capture the essential dynamics of soft particle liquids (liquids composed of particles with continuous pair potentials) [22, 29, 30, 31], is there anything common between the potential energy landscapes of both kinds of liquids? What are the features of the landscape that are dominating the dynamics of both systems? Here we present a unified theory based on potential energy landscape - geodesic theory, which focuses on the global length scale of the landscape instead of local variance. We show that the geodesics can predict dynamics slowing down for both soft particle liquids and hard particle liquids, as well as contain information about some other dynamical features. Geodesics represent the inherent dynamics of a system.

Chapter 2

Geodesic Theory

This chapter first introduces the potential energy landscape ensemble [32], a natural framework to define paths through the potential energy landscape and to develop geodesic theory. It then presents geodesic theory [33], a unified approach to study dynamics of liquid based on potential energy landscape. The end of the chapter shows some previous results [33] to demonstrate how geodesics predict the dynamics of soft particle liquids .

2.1 Potential Energy Landscape Ensemble

The potential energy landscape ensemble is defined as the set of all configurations $\mathbf{R}$ that have a potential energy $V(\mathbf{R})$ no bigger than some landscape energy E_L [32].

$$\mathbf{R} : V(\mathbf{R}) \leq E_L \tag{2.1}$$

An illustration of the potential energy landscape ensemble is in Fig. 2.1.

The potential energy landscape ensemble is thermodynamically equivalent to the canonical ensemble [32]. The landscape energy E_L in the potential energy landscape ensemble is the counterpart of temperature T in the canonical ensemble.

In the potential energy landscape ensemble, one can show by maximizing the

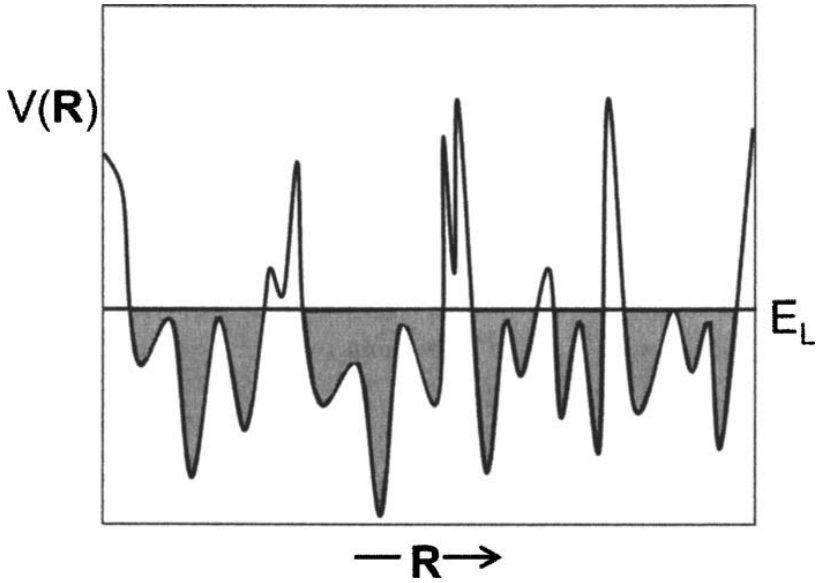

Figure 2.1: Illustration of the potential energy landscape ensemble. Figure taken from [32]. The jagged curve is the potential energy $V(\mathbf{R})$ of a system, and the horizontal direct line represents the landscape energy E_L. Only configurations satisfying $V(\mathbf{R}) \leq E_L$ are allowed in the potential energy landscape ensemble, marked by the grey area in the figure.

entropy that every allowed configuration has the same probability density $\rho(\mathbf{R})$ [32].

$$\rho(\mathbf{R}) = \theta[E_L - V(\mathbf{R})]/G(E_L) \tag{2.2}$$

$$G(E_L) = \int \mathrm{d}\mathbf{R}\ \theta[E_L - V(\mathbf{R})] \tag{2.3}$$

where $\theta(x) = (1, x \geq 0; 0, x < 0)$ is the Heaviside step function.

Each configuration, within the potential energy landscape ensemble, is either disallowed or allowed with the same probability density as every other allowed configuration. In the canonical ensemble, different configurations have different probability densities. The system has to wait to accumulate large enough energy fluctuation to overcome energy barriers for propagation. In the potential energy landscape ensemble, however, the system has free propagation, because each allowed configuration has the same probability density, but the propagation problem has more complex boundary conditions $V(\mathbf{R}) \leq E_L$.

The disallowed configurations $V(\mathbf{R}) > E_L$ form forbidden regions in the 3N-dimensional configuration space, where system cannot travel in the context of potential energy landscape ensemble. The system can be seen as a point diffusing outside these forbidden regions in the $3N$ dimensional space, which enables the use of Green's function to develop geodesic theory, as shown in Section 2.2.

2.2 Geodesic Theory

In a high-dimensional space, the volume of a hyper-sphere is dominated by the volume of the thin shell near the surface [32]. Therefore, it is reasonable to expect in the $3N$ dimensional configuration space, most of the allowed configurations lie close to the boundary $V(\mathbf{R}) = E_L$. The trajectories of the system evolving should then be paths close to the constant-potential-energy contours of these boundaries in potential energy landscape ensemble.

When the dynamic is slow, what is the most important trajectory that dominates the dynamics of the system?

A system has free propagation in the potential energy landscape ensemble. For free propagation, the probability density of a system going from some initial configuration $\mathbf{R}_i$ to some final configuration $\mathbf{R}_f$ in a time t is described by the solution of Fokker-Planck equation in the form of path integral [34, 35, 36, 37], given by Green's function [32]:

$$G(\mathbf{R}_i \to \mathbf{R}_f|t) = \int \exp\big\{ -\frac{1}{4D}\int (\frac{\mathrm{d}\mathbf{R}}{\mathrm{d}\tau})^2 \mathrm{d}\tau \big\} \mathrm{d}\mathbf{R}(\tau) \tag{2.4}$$

The action S along the path is

$$S[\mathbf{R}(\tau)] = \int (\frac{\mathrm{d}\mathbf{R}}{\mathrm{d}\tau})^2 \mathrm{d}\tau = \int (2T(\tau))\mathrm{d}\tau \tag{2.5}$$

where T is the kinetic energy

$$T = \frac{1}{2}\sum_{\mu\nu} g_{\mu\nu}\frac{\mathrm{d}x^{\mu}}{\mathrm{d}\tau}\frac{\mathrm{d}x^{\nu}}{\mathrm{d}\tau} \tag{2.6}$$

with μ and ν labeling all degrees of freedom, and $g_{\mu\nu}$ is the kinematical metric.

In the limit of $D \to 0$ (slow dynamics), the dominant paths are those minimizing the path-integral action S. These paths also obey the principle of least action in classical mechanics.

$$\delta S[\mathbf{R}(\tau)] = 0 \tag{2.7}$$

At the same time, the kinematic path length l is

$$l = \int \mathrm{d}s = \int_0^t \sqrt{2T(\tau)}\mathrm{d}\tau \tag{2.8}$$

$$(\mathrm{d}s)^2 = \sum_{\mu\nu} g_{\mu\nu}\mathrm{d}x^{\mu}\mathrm{d}x^{\nu} = 2T(\mathrm{d}\tau)^2 \tag{2.9}$$

The path with the shortest kinematic path length l, the geodesic we refer to, also minimizes the path-integral action S. Therefore when dynamics is slow, the dominant path is the geodesics for the metric $g_{\mu\nu}$.

Some examples:

- Single component system with only translational diffusion [32]

  The kinematic metric

  $$g_{\mu\nu} = M\delta_{\mu\nu} \tag{2.10}$$

  where all the particles have the same mass M, $\delta_{\mu\nu} = (1, \text{if } \mu = \nu\ ;\ 0, \text{otherwise})$.

  The kinetic energy

  $$T = \frac{1}{2}\sum_{j=1}^{N} M(\frac{\mathrm{d}\mathbf{r}_j}{\mathrm{d}\tau})^2 \tag{2.11}$$

  where j labels the j-th particle, $\mathbf{r}$ is the position of the center of mass of particle.

  The kinematic path length is then proportional to the actual path length in

Cartesian coordinates.

$$l = \int \mathrm{d}s = M^{1/2} \int \sqrt{\sum_{j=1}^{N} (\mathrm{d}\mathbf{r}_j)^2} \tag{2.12}$$

So the dominant path is at the same time the shortest path.

- Single component system with both translational and rotational diffusion [38]

  The kinetic energy T includes both translation and rotation.

$$T = \sum_{j=1}^{N} \left(M(\frac{\mathrm{d}\mathbf{r}_j}{\mathrm{d}\tau})^2 + I(\frac{\mathrm{d}\hat{\mathbf{\Omega}}_j}{\mathrm{d}\tau})^2 \right) \tag{2.13}$$

  where j labels the j-th particle, M is the mass , $\mathbf{r}$ is the position of the center of mass, I is the moment of inertia, $\hat{\mathbf{\Omega}}$ is the orientational unit vector.

  The dominant paths are those minimizing the action S as well as the kinematic length l [38].

$$S[\mathbf{R}(\tau)] = \int (2T(\tau))\mathrm{d}\tau = \int \sum_{j=1}^{N} \left(M(\frac{\mathrm{d}\mathbf{r}_j}{\mathrm{d}\tau})^2 + I(\frac{\mathrm{d}\hat{\mathbf{\Omega}}_j}{\mathrm{d}\tau})^2 \right) \mathrm{d}\tau \tag{2.14}$$

$$l = \int \sqrt{2T(\tau)}\mathrm{d}\tau = \int \sqrt{\sum_{j=1}^{N} \left(M(\frac{\mathrm{d}\mathbf{r}_j}{\mathrm{d}\tau})^2 + I(\frac{\mathrm{d}\hat{\mathbf{\Omega}}_j}{\mathrm{d}\tau})^2 \right)} \mathrm{d}\tau \tag{2.15}$$

2.2.1 Diffusion

What information do these paths tell about the dynamics of a system? One natural quantity is the diffusion coefficient. In the context of potential energy landscape ensemble, the system is a free diffusing point around impenetrable obstacles ($V(\mathbf{R}) > E_L$) in $3N$ dimensional space. Lieb pointed out that the action of diffusion with a spherical obstacle depends on the shortest path g between end points [33]. The greatest contribution to diffusion comes from the shortest path with minimum

action.

$$G(\mathbf{R}_i \to \mathbf{R}_f|t) \sim (4\pi D_0 t)^{-\frac{d}{2}} \exp\Big\{ - \frac{g^2}{4D_0 t}\Big\} \tag{2.16}$$

where g is the length of the geodesic path, d is the spacial dimension, D_0 is the diffusion coefficient without any obstacles.

The phenomenological diffusion constant D is still predicted by Green's function

$$G(\mathbf{R}_i \to \mathbf{R}_f|t) \sim (4\pi D t)^{-\frac{d}{2}} \exp\Big\{ - \frac{|\mathbf{R}_f - \mathbf{R}_i|^2}{4Dt}\Big\} \tag{2.17}$$

Combining equations 2.16 and 2.17 shows that

$$D = \lim_{\Delta R \to \infty} D_0 \overline{(\Delta R/g)^2} \tag{2.18}$$

where the overbar means an average over multiple pairs of end points $\mathbf{R}_i$ and $\mathbf{R}_f$ with equilibrium distribution, and ΔR is the distance between configuration $\mathbf{R}_f$ and configuration $\mathbf{R}_i$,

$$\Delta R = |\mathbf{R}_f - \mathbf{R}_i| = \sqrt{\sum_{j=1}^{N} (\mathbf{r}_j^f - \mathbf{r}_j^i)^2} \tag{2.19}$$

$$\mathbf{R}_f = (\mathbf{r}_1^f, \cdots, \mathbf{r}_N^f), \mathbf{R}_i = (\mathbf{r}_1^i, \cdots, \mathbf{r}_N^i) \tag{2.20}$$

Equation 2.18 demonstrates that the experimental diffusion constant can be obtained by using only information about the global path lengths in the potential energy landscape, without any regard to local features such as transition barriers (as needed in the canonical ensemble). In fact, there is no local barrier in the potential energy ensemble because every allowed configuration is equally likely. Moreover, since Equation 2.18 does not rely on finding the maxima or minima of the potential energy landscape, it can in principle be applied to any system, including systems with singular potential such as hard sphere liquids.

The point of view is that the dynamics is slowing down not because of the increasing difficulty in local barrier crossing, but because the forbidden regions are getting

bigger and the accessible paths around these regions are getting more convoluted and longer. There may be a point when these growing forbidden regions divide the allowed portion of configuration space into separate parts, which corresponds to the mode coupling transition [33].

In the limit of high mobility (high temperature for soft particle systems and low density for hard sphere systems), $D = \sigma_0$. In calculation, the absolute value of σ_0 is unknown, but the trend of D can still be predicted by

$$D \propto \overline{(\Delta R/g)^2} \tag{2.21}$$

Other dynamical problems such as preferential solvation can also be studied through geodesic theory [39].

2.3 Previous Results

Previous research [33] shows how geodesic theory predicts dynamics slowing down for soft particle liquids. Both a simple monoatomic Lennard-Jones liquid and a binary glass-forming Kob-Andersen liquid have been studied in [33]. For both liquids, the diffusion constants from landscape predictions agree with molecular dynamics calculations over a wide range.

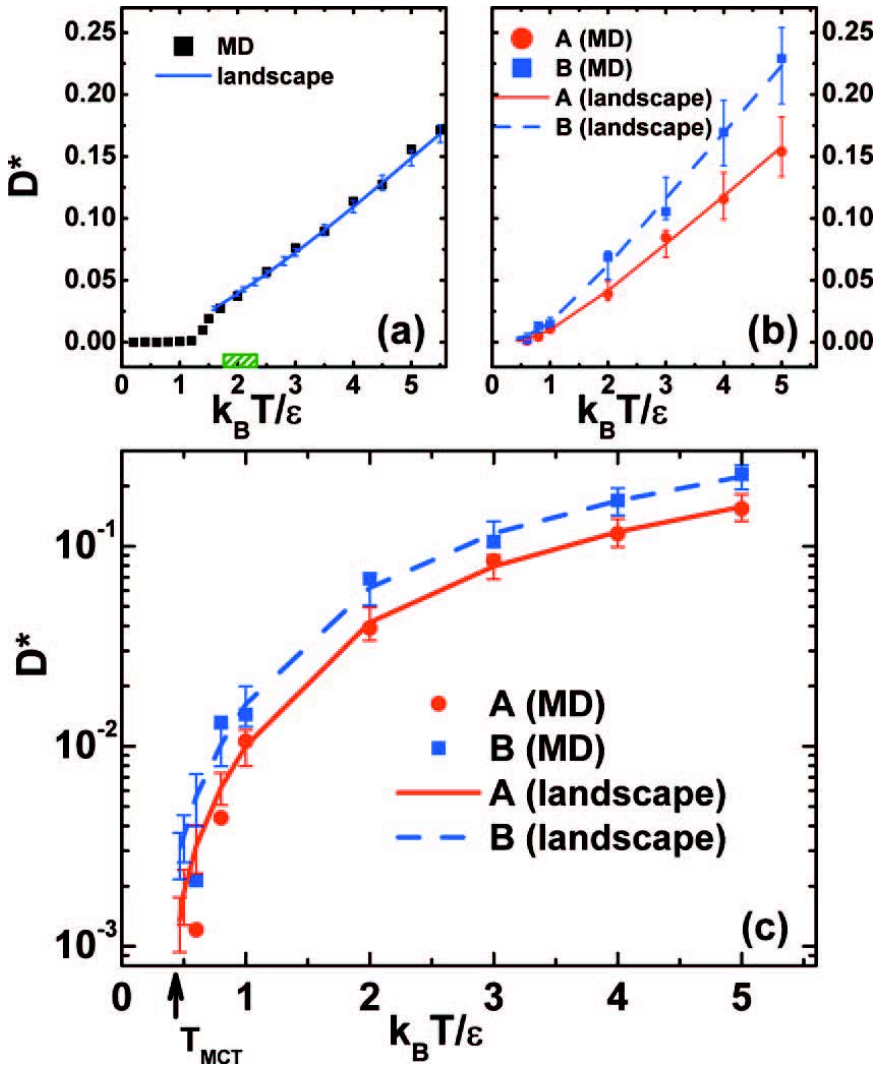

Figure 2.2: Reduced diffusion coefficient $D^* = D\sqrt{m/\epsilon\sigma^2}$ as a function of reduced temperature k_BT/ϵ of a simple monoatomic Lennard-Jones liquid (a) and a glass-forming Kob-Andersen liquid (b,c). Figure taken from [33]. "MD" means results from molecular dynamics calculation and "landscape" means geodesic-landscape theory prediction. A and B are the two species of particles in the binary Kob-Andersen liquid. T_{MCT} is the location of the literature empirical mode-coupling transition for the Kob-Andersen liquid. As the temperature T approaches T_{MCT}, the dynamics slows down dramatically, shown by the decrease of diffusion coefficients over several orders of magnitude. The predictions from geodesic theory agree very well with the molecular dynamics calculations across several orders of magnitude.

Chapter 3

Methods

This chapter first presents the method of finding geodesics for soft particle liquids from previous research [33]. Then the newly developed geodesics finding method for hard sphere liquids is given, followed by the method of molecular dynamics calculation of diffusion coefficients of hard sphere liquids.

3.1 Soft Particle Liquid

3.1.1 Models

Kob-Andersen liquid is used as a model of soft particle liquid system. This binary mixture is a widely-studied glass-forming model liquid [40, 41, 42, 13, 43]. It is used in [33] as an example of geodesic theory on soft particle glass-forming liquids. The mixture has a empirical mode coupling transition at reduced temperature $k_BT/\epsilon = 0.435$ [44, 45]. The pair potential energy $\mu_{\alpha\beta}$ between two particles α and β is

$$\mu_{\alpha\beta}(r) = \begin{cases} \mu^{LJ}_{\alpha\beta}(r) - \mu^{trunc}_{\alpha\beta}(r) & r < r_c = 2.5\sigma_{\alpha\beta} \\ 0, & r > r_c = 2.5\sigma_{\alpha\beta} \end{cases} \tag{3.1}$$

$$\mu^{LJ}_{\alpha\beta}(r) = 4\epsilon_{\alpha\beta}[(\frac{\sigma_{\alpha\beta}}{r})^{12} - (\frac{\sigma_{\alpha\beta}}{r})^{6}] \tag{3.2}$$

$$\mu_{\alpha\beta}^{trunc}(r) = \mu_{\alpha\beta}^{LJ}(r_c) \tag{3.3}$$

with parameters

$$\epsilon_{AA} = \epsilon, \quad \epsilon_{BB} = 0.5\epsilon, \quad \epsilon_{AB} = 1.5\epsilon \tag{3.4}$$

$$\sigma_{AA} = \sigma, \quad \sigma_{BB} = 0.88\sigma, \quad \sigma_{AB} = 0.8\sigma \tag{3.5}$$

where $\alpha, \beta = A \; or \; B$ denote species of particles, r is the distance between the two particles.

In this thesis, the calculation of geodesics of Kob-Andersen liquid uses $N = 108$ ($N_A = 87$, $N_B = 21$) at total reduced density $\rho\sigma^3 = 1.2$.

$$\rho\sigma^3 = \frac{N}{V_{box}}\sigma^3 \tag{3.6}$$

where V_{box} is the volume of simulation box. The range of temperature studied is from $k_BT/\epsilon = 5.0$ to $k_BT/\epsilon = 0.7$.

3.1.2 Geodesics Finding of Soft Particle Liquids

3.1.2.1 Kuhn-Tucker Theorem

The geodesic problem in the potential energy landscape ensemble is :

$$optimization : the \; shortest \; path \; g \; between \; two \; end \; points \; \mathbf{R}_i \; and \; \mathbf{R}_f \tag{3.7}$$

$$constraints : V(\mathbf{R}) \leq E_L \; along \; the \; path \tag{3.8}$$

The Kuhn-Tucker theorem [46] states that an optimization problem with inequality constraints has a solution that is a combination of unconstrained segments and segments satisfying the constraints as equalities. Thus the geodesic should be a combination of free propagation steps ($V(\mathbf{R}) < E_L$) and steps along the boundary ($V(\mathbf{R}) = E_L$) [33].

The path finding procedure includes three parts: finding the appropriate pairs of end points with equilibrium distribution, finding paths between pairs of end points, and optimizing the paths.

3.1.2.2 Finding End Points

To ensure connectness between each pair of end points, molecular dynamics based on Verlet algorithm [47] is used to generate pairs of end points. The reduced time step for integrating equation of motion in Verlet algorithm is $\frac{\delta t}{\sigma\sqrt{m/\epsilon}} = 0.001$ for all temperatures, where m is the mass per particle.

The initial configuration of the system is set up as a face centered crystal. The initial velocities are assigned by random numbers drawn from Maxwell-Boltzman distribution then adjusted to remove the net momentum of the system. To melt the system fast from a crystal structure into an equilibrium liquid state, the velocities are first scaled according to $\sum_{i=1}^{N} \frac{1}{2}m\mathbf{v}_i^2 = \frac{3}{2}Nk_BT_{in}$, $k_BT_{in}/\epsilon = 5.0$. The high temperature allows faster relaxation. Then $2 * 10^5$ molecular dynamic steps are performed, rescaling the velocities every 1000 steps according to $\sum_{i=1}^{N} \frac{1}{2}m\mathbf{v}_i^2 = \frac{3}{2}Nk_BT_{in}$.

After this, the crystal structure has melted. The system then needs to be cooled down gradually to the desired temperature. This is done by running another 10^6 molecular dynamic steps, rescaling the velocity every 1000 steps according to $\sum_{i=1}^{N} \frac{1}{2}m\mathbf{v}_i^2 = \frac{3}{2}Nk_BT$, where T is the desired final temperature of the system.

To check whether the system has reached the desired temperature, we run another 10^6 molecular dynamics steps without any velocity rescaling. The temperature of the system is recorded every 100 steps then the average temperature is calculated. If the difference between the average temperature and the desired temperature is less than $0.005\epsilon/k_B$, the system is considered to have reached the desired temperature. Otherwise we rescale the velocities then check again. This process is repeated until the desired temperature is reached. Afterwards there is no more rescaling of velocity.

We run another 10^6 MD steps before collecting pairs of end points. We record

a configuration as the first end point of the first pair, propagate the system until it is away from the first end point by a desired distance ΔR. This configuration is recorded as the second configuration of the pair. We propagate 10^5 MD steps before collecting next pair of end points to avoid correlations among different pairs. The process is repeated until desired number of pairs are collected.

The distance ΔR between two configurations $\mathbf{R}_a = (\mathbf{r}_1^a, \cdots, \mathbf{r}_N^a)$ and $\mathbf{R}_b = (\mathbf{r}_1^b, \cdots, \mathbf{r}_N^b)$ is

$$\Delta R = |\mathbf{R}_b - \mathbf{R}_a| = \sqrt{\sum_{j=1}^{N} (\mathbf{r}_j^b - \mathbf{r}_j^a)^2} \tag{3.9}$$

where the 3 dimensional vector $\mathbf{r}_j$ denotes the position of particle j.

3.1.2.3 Finding Geodesics

The method of finding geodesics for soft particle system is from [33]. Given a pair of end points denoted as $\mathbf{R}_i$ and $\mathbf{R}_f$, the landscape energy E_L is the higher value of $V(\mathbf{R}_i)$ and $V(\mathbf{R}_f)$. $E_L = \max(V(\mathbf{R}_i), V(\mathbf{R}_f))$. According to Kuhn-Tucker theorem, the path consists of direct steps (free propagation steps) and escape steps (steps along the boundaries) [33].

1. Direct Step

   Direct steps implement the free propagation segments of a path based on Kuhn-Tucker theorem. The system starts from the initial configuration $\mathbf{R}_i$, always tries to move from its current position $\mathbf{R}(t)$ directly towards the final configuration $\mathbf{R}_f$, with a small step size δ_{di}. The trial configuration $\mathbf{R}^0(t+1)$ is

   $$\mathbf{R}^0(t+1) = \mathbf{R}(t) + \delta_{di} \frac{\mathbf{R}_f - \mathbf{R}(t)}{|\mathbf{R}_f - \mathbf{R}(t)|} \tag{3.10}$$

   In calculation $\delta_{di} = 0.001\sigma$ is used.

   If the trial configuration is in the allowed regions of configuration space ($V(\mathbf{R}^0(t+1)) \leq E_L$), this $\mathbf{R}^0(t+1)$ is accepted as the new configuration of the system

along the path. The system will proceed from there.

2. Escape Step

   Escape steps implement the segments of a path that are along the boundaries based on Kuhn-Tucker theorem. If the trial configuration $\mathbf{R}^0(t+1)$ is in the forbidden region of configuration space ($V(\mathbf{R}^0(t+1)) > E_L$), an escape step is performed. A gradient descend procedure is employed to direct the system from the disallowed trial location to its nearest allowed point ($V(\mathbf{R}(t+1)) \leq E_L$), according to

$$\mathbf{R}^{n+1}(t+1) = \mathbf{R}^n(t+1) - \frac{V(\mathbf{R}^n(t+1)) - E_L}{|\nabla V(\mathbf{R}^n(t+1))|^2} \nabla V(\mathbf{R}^n(t+1)) \tag{3.11}$$

   where n is the index of iteration step, $\mathbf{R}^0(t+1)$ is the initial disallowed configuration, and ∇V represents the $3N$ dimentional gradient of potential energy function V respect to $\mathbf{R}$ in the configuration space. The iteration stops when $V(\mathbf{R}^{n+1}(t+1)) \leq E_L$, and this $\mathbf{R}^{n+1}(t+1)$ is taken to be the new configuration of the system along the path. The system will proceed from there.

   In calculation, a tolerance δV for the system is needed due to numerical errors in each step. For example, the iteration of equation 3.11 would never stop without a cutoff tolerance. Thus in implementation a configuration is considered allowed if $V(\mathbf{R}) \leq (E_L + \delta V)$, $\delta V = 10^{-4}\epsilon$. This is equivalent to raising a tiny amount of landscape energy for computational convenience.

3. A path is found when the distance between the current configuration of the system $\mathbf{R}(t)$ and the second end point $\mathbf{R}_f$ is smaller than δ_{di}.

$$|\mathbf{R}_f - \mathbf{R}(t)| < \delta_{di} \tag{3.12}$$

   The path length l is the sum of the length of every successful steps (steps con-

necting two consecutive allowed configurations) along the path.

$$l = \sum_{t=0}^{t=P} |\mathbf{R}(t+1) - \mathbf{R}(t)| \tag{3.13}$$

where P is the total number of steps along the path, $\mathbf{R}(0) = \mathbf{R}_i$, $\mathbf{R}(P{+}1) = \mathbf{R}_f$.

An illustration of the path finding method is in Fig. 3.1. The algorithm is shown in Algorithm 1.

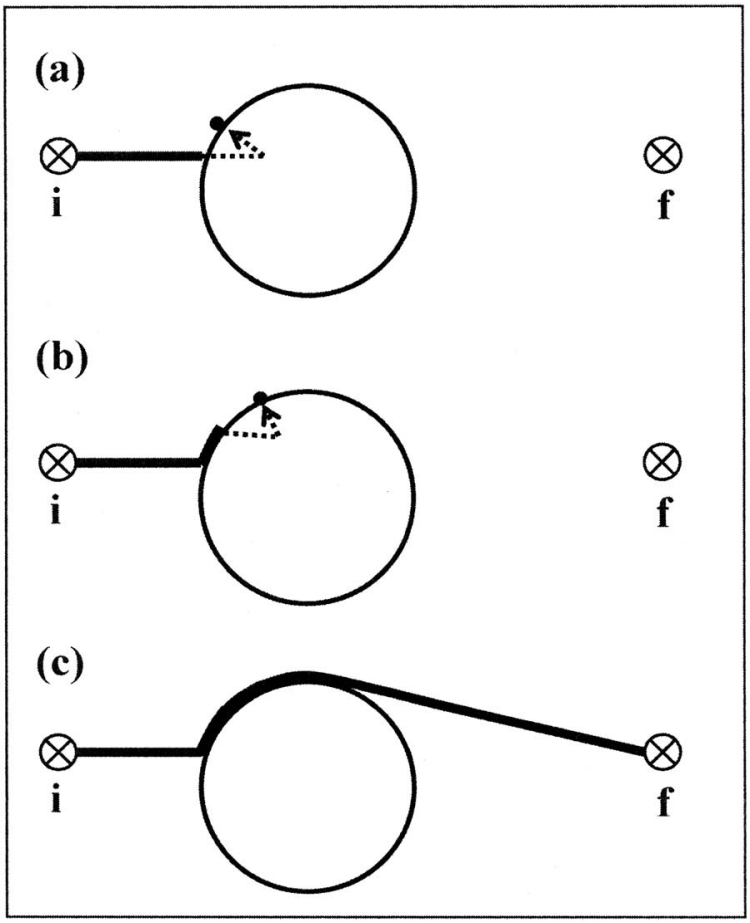

Figure 3.1: Illustration of path finding algorithm for soft particle systems. Figure taken from [33]. The small circles with **i** and **f** denote initial and final configurations respectively in the configuration space. The big circle in the middle is a forbidden region. The system always tries to head toward the final point directly (a,c) unless it meets an obstacle and has to move around the obstacle (b).

Algorithm 1 Path finding for soft particle systems

$E_L \leftarrow MAX(V(\mathbf{R}_i), V(\mathbf{R}_f))$
$l \leftarrow 0$ ▷ path length
$\mathbf{R}_t$ ▷ current configuration of the system
$\mathbf{R}_o$ ▷ previous allowed configuration of the system
$\mathbf{R}_t \leftarrow \mathbf{R}_i$, $\mathbf{R}_o \leftarrow \mathbf{R}_i$
while $|\mathbf{R}_f - \mathbf{R}_t| > \delta_{di}$ **do** ▷ $\delta_{di} = 0.001\sigma$
$\mathbf{R}_o \leftarrow \mathbf{R}_t$
$\mathbf{R}_t \leftarrow \mathbf{R}_t + \delta_{di}\dfrac{\mathbf{R}_f - \mathbf{R}_t}{|\mathbf{R}_f - \mathbf{R}_t|}$ ▷ direct step
  while $V(\mathbf{R}_t) > (E_L + \delta V)$ **do** ▷ $\delta V = 10^{-4}\epsilon$
    $\mathbf{R}_t \leftarrow \mathbf{R}_t - \dfrac{V(\mathbf{R}_t) - E_L}{|\nabla V(\mathbf{R}_t)|^2}\nabla V(\mathbf{R}_t)$ ▷ escape step
  end while
$l \leftarrow l + |\mathbf{R}_t - \mathbf{R}_o|$
end while
return l

3.1.2.4 Optimization

As illustrated in Fig. 3.1, a path found from above procedure is not necessarily the shortest possible. Optimization is needed on these geodesics candidates. This can be done by trials of local adjustments in search for shorter paths.

Given a path found from $\mathbf{R}_i$ to $\mathbf{R}_f$ as the original geodesic candidate, a configuration $\mathbf{R}$ along the path is picked by random, and given a small displacement to a new allowed configuration $\mathbf{R}'$. A new path of two segments is generated by the same path finding procedure, one from $\mathbf{R}_i$ to $\mathbf{R}'$, and the other from $\mathbf{R}'$ to $\mathbf{R}_f$. The new path length is the sum of the lengths of the two segments. If the new path is shorter than the original geodesic candidate, the new path is taken to be the new candidate for the geodesics, and the same optimization procedure is used on this new candidate path. If the original candidate is shorter, the optimization repeats on the original path. In principle this procedure continues until the path length converges. Due to the limitation of computational time, the optimization stops when the trial on a geodesic candidate path for finding shorter paths fails five times consecutively, and the final path is taken to be the geodesic.

The detailed procedure is listed below:

1. Record 10^3 configurations along the path equally distanced according to their distances to the final end point.

2. Select one configuration $\mathbf{R} = (\mathbf{r}_1, \cdots, \mathbf{r}_N)$ by random from the recorded configurations, select one particle k by random in this configuration and move it by a random amount $\delta\mathbf{r} = (\delta x, \delta y, \delta z)$, which satisfy $-0.10\sigma \leq \delta x \leq 0.10\sigma$, $-0.10\sigma \leq \delta y \leq 0.10\sigma$, $-0.10\sigma \leq \delta z \leq 0.10\sigma$. The move $\mathbf{r}'_k = \mathbf{r}_k + \delta\mathbf{r}$ is accepted only if the new configuration $\mathbf{R} = (\mathbf{r}_1, \cdots, \mathbf{r}'_k, \cdots, \mathbf{r}_N)$ is an allowed one in the potential energy ensemble. It means the potential energy of the new configuration does not exceed the landscape energy.

3. Repeat the process until the distance between the original configuration $\mathbf{R}$ and the new allowed configuration $\mathbf{R}'$ is bigger than 0.10σ.

4. Find a path from $\mathbf{R}'$ to $\mathbf{R}_i$, and a path from $\mathbf{R}'$ to $\mathbf{R}_f$. This forms a new path between $\mathbf{R}_i$ and $\mathbf{R}_f$. If the new path is shorter than the original path, set the new path as our geodesic candidate which we will optimize. Otherwise optimize the original path again.

5. Keep this process until 5 consecutive fails of finding a shorter path than the current geodesic candidate.

6. The final geodesic candidate is taken to be the geodesic path.

The algorithm of optimization is in Algorithm 2.

Algorithm 2 Optimization of paths

```
l_c                                              ▷ original candidate for geodesic
l_n                                                              ▷ new path
counter ← 0                                  ▷ count the number of consecutive fails
pick randomly R
R' ← MonteCarlo(R)                          ▷ Monte Carlo, |R' − R| ≥ 0.10σ
l_n ← PathLength(R', R_i) + PathLength(R', R_f)
while counter < 5 do                                  ▷ allow 5 consecutive fails
    if l_n < l_c then
     l_c ← l_n
     counter ← 0
    else
     counter ← counter + 1
    end if
end while
return l_c                                                       ▷ final geodesic
```

3.2 Hard Sphere Liquid

3.2.1 Models

The models used for hard sphere liquids are the two system discussed in Chapter 1, the simple mono disperse hard sphere liquid, and the glass-forming binary hard sphere system with diameter ratio $\sigma_b : \sigma_s = 1.4\sigma : \sigma$ and number ratio $N_b : N_s = 1 : 1$.

The pair potential energy μ_{ij} between sphere i and j is

$$\mu_{ij} = \begin{cases} 0 & : r_{ij} \geq \sigma_{ij} \\ \infty & : r_{ij} < \sigma_{ij} \end{cases} \tag{3.14}$$

$$\sigma_{ij} = \frac{1}{2}(\sigma_i + \sigma_j) \tag{3.15}$$

where r_{ij} is the distance between the center of sphere i and the center of sphere j, and σ is the diameter of each sphere. σ_{ij} is the minimum distance between the centers of two spheres without any overlapping.

The calculation of geodesics of hard sphere liquids use various system sizes N. In the binary liquid case $N = N_b + N_s$. The calculation of MD results of diffusion

coefficients of hard sphere liquids use $N = 108$ for both the mono-disperse system and the binary system. The range of densities studied is from low values $\phi = 0.05$ to values close to the freezing point $\phi_f = 0.49$ for the mono disperse system and the empirical mode coupling transition $\phi_c = 0.59$ for the binary system.

3.2.2 Geodesics Finding of Hard Sphere Liquids

The path finding of hard sphere liquid also includes three parts: finding the appropriate pairs of end points with equilibrium distribution, finding paths between end points, and optimizing the paths.

3.2.2.1 Finding End Points

To ensure connectness between pairs of end points, molecular dynamics based on collision dynamics [47] is used to generate end points. Details of setting up the molecular dynamics run and equilibrating the system is given in section 3.2.3.

After the system has equilibrated, we record a configuration as the first end point of the first pair, then propagate the system until it is away from the first end point by a desired distance ΔR. This configuration is recorded as the second end point of the pair. We propagate 10^5 MD steps before collecting next pair of end points to avoid correlations among different pairs. This procedure is repeated until desired number of pairs are collected.

3.2.2.2 Finding Geodesics

Due to the singularity of hard sphere potential, there is no gradient to utilize for the escape step. Moreover, unlike the soft sphere case, two overlapping hard spheres are enough to make a configuration disallowed, and there is nothing other spheres can do to compensate the potential energy violation. So every overlapping pair of hard spheres needs to be treated individually. Although the basic idea of always trying

moving towards the end point and away from the obstacles applies, the path finding algorithm of hard sphere liquids has to be different from that of soft particle liquids.

The idea of free volume turns out to be a useful guidance for path finding for hard sphere liquids. Free volume is defined as the space the center of a given hard sphere can move independently from the surrounding spheres [48]. Free volume is known to affect the dynamics of liquids [49, 50, 51, 52]. Here, instead of utilizing gradient to find the nearest allowed configuration from the disallowed trial configuration as in the case of soft particle liquids, the system goes back to where it was before the failed trial step, then moves away from the forbidden region for a small distance. This move creates more free volume for the spheres that are potentially causing potential energy violation, thus allowing more freedom for the system to reorientate itself in configuration space and move towards the second end point without going into the forbidden region.

The path consists of direct steps and collision avoidance steps.

1. Direct Step

   In direct step, the system always tries to go from its current position $\mathbf{R}(t)$ to the second end point $\mathbf{R}_f$, with a small step size δ_{di}. This step employs the same idea of free propagation step as in the soft particle liquid. Direct steps implement the free propagation segments of a path based on Kuhn-Tucker theorem.

$$\mathbf{R}^0(t+1) = \mathbf{R}(t) + \delta_{di}\frac{\mathbf{R}_f - \mathbf{R}(t)}{|\mathbf{R}_f - \mathbf{R}(t)|} \tag{3.16}$$

$$\delta_{di} = 10^{-2}\sigma \tag{3.17}$$

   where $\sigma = \sigma_s$ in the binary liquid case. The trial location $\mathbf{R}^0(t+1)$ is accepted as the new configuration of the system along the path if $V(\mathbf{R}^0(t+1)) \leq E_L = 0$. In hard sphere case this means there is no overlapping in the system between any particles. The system will proceed from the new configuration.

2. Collision Avoidance Step

What's different though, for the hard sphere liquids, is what to do once a trial direct step takes the system to a forbidden region in the configuration space. As discussed above, the gradient descend method for escape step in the soft sphere liquid is no longer applicable to the hard sphere liquid. Instead, the collision avoidance step is performed to cancel the overlaps and reposition the system.

First the failed direct step is rescinded and the system is back to its last allowed configuration $\mathbf{R}(t)$ before the failed direct step. Then the overlapped particles in the disallowed trial configuration $\mathbf{R}^0(t+1)$ are further moved away from each other in the allowed configuration $\mathbf{R}(t)$, according to the following procedure.

Define a fictitious pair potential μ_{ij} that is zero between non-overlapping particles i and j, but has a finite and positive value when particle i and j overlap.

$$\mu_{ij} = \begin{cases} 0 & : r_{ij} \geq \sigma_{ij} \\ \nu(r_{ij}/\sigma_{ij}) & : r_{ij} < \sigma_{ij} \end{cases} \tag{3.18}$$

$$\nu(x) > 0 \quad if\ 0 < x < 1 \tag{3.19}$$

This fictitious potential imposes the same constraints on the configuration space as the original singular potential, because both potentials require and only require configurations to have no overlapping.

A fictitious force $\mathbf{f}$ can be defined from μ_{ij} if the derivative of $\nu(x)$ with respect to x, denoted as $\nu'(x)$, is negative for $0 < x < 1$.

$$\nu'(x) < 0 \quad if\ 0 < x < 1 \tag{3.20}$$

$$\mathbf{f}_i = -\nabla_i\ \mu_{ij} = \begin{cases} 0 & : r_{ij} \geq \sigma_{ij} \\ \dfrac{1}{\sigma_{ij}}\nu'_{ij}\hat{\mathbf{r}}_{ij} & : r_{ij} < \sigma_{ij} \end{cases} \tag{3.21}$$

$$\hat{\mathbf{r}}_{ij} = \frac{\mathbf{r}_j - \mathbf{r}_i}{|\mathbf{r}_j - \mathbf{r}_i|} \tag{3.22}$$

For a failed trial configuration $\mathbf{R}^0(t+1)$, define the weighed force vector on each sphere j,

$$\mathbf{F}_j^0(t+1) = \left[c_j \hat{f}_j\right]_{\mathbf{R}^0(t+1)} \tag{3.23}$$

$$c_j = \frac{|\mathbf{f}_j|}{\sqrt{\sum_1^N |\mathbf{f}_i|^2}} \tag{3.24}$$

$$\hat{f}_j = \frac{\mathbf{f}_j}{|\mathbf{f}_j|} \tag{3.25}$$

$$\hat{\mathbf{g}}_j^0 = \frac{\mathbf{F}_j^0(t+1)}{|\mathbf{F}_j^0(t+1)|} \tag{3.26}$$

Then each particle in the system is moved according to

$$\mathbf{r}_j^1(t+1) = \mathbf{r}_j(t) + \delta_{ca}\hat{\mathbf{g}}_j^0 \tag{3.27}$$

$$\delta_{ca} = 10^{-4}\sigma \tag{3.28}$$

where δ_{ca} is the step size for each particle, $\sigma = \sigma_s$ in the binary liquid case. Note $\hat{\mathbf{g}}_j^0 = \mathbf{0}$ for particles without any overlapping in configuration $\mathbf{R}^0(t+1)$.

However, this simple $\hat{\mathbf{g}}_j^0$ may not accomplish the task of avoiding overlapping in the whole system, because new overlapping may be introduced by Equation 3.27. For example, if particle i and j are overlapped in configuration $\mathbf{R}^0(t+1)$, although pulling them apart in configuration $\mathbf{R}(t)$ increases the free space among those two particles, this move may make particle i and some other particle k overlap. Denote this new failed trial configuration as $\mathbf{R}^1(t+1)$. In this situation,

another fictitious force is calculated from this disallowed configuration $\mathbf{R}^1(t+1)$ as well and the final fictitious force is a combination of forces from all failed trial configurations. The iteration repeats until a successful trial configuration is found. This procedure allows the system to "detect" the obstacles around it in configuration space then finds the best direction to move.

Suppose m iterations is needed,

$$\hat{\mathbf{g}}_j^m = \frac{\sum_{T=1}^{m} \mathbf{F}_j^T(t+1)}{|\sum_{T=1}^{m} \mathbf{F}_j^T(t+1)|} \tag{3.29}$$

$$\mathbf{F}_j^T(t+1) = \left[c_j \hat{f}_j\right]_{\mathbf{R}^T(t+1)} \tag{3.30}$$

where the superscript T denotes the index of each failed trial.

Each particle j is moved from the allowed configuration $\mathbf{R}(t)$ to the newly allowed configuration $\mathbf{R}^{m+1}(t+1)$, according to

$$\mathbf{r}_j^{m+1}(t+1) = \mathbf{r}_j(t) + \delta_{ca}\hat{\mathbf{g}}_j^m \tag{3.31}$$

$$\delta_{ca} = 10^{-4}\sigma \tag{3.32}$$

This $\mathbf{R}^{m+1}(t+1)$ is taken to be the new configuration of the system along the path, and the system will proceed from there.

The fictitious potential used in calculation for main results is

$$\nu_{ij}(x) = \sigma_{ij}^2(1-x) \tag{3.33}$$

Trials with an alternate potential $\nu_{ij}(x) = \sigma_{ij}^3(\frac{1}{3}x^3 - \frac{1}{2}x^2 + \frac{1}{6})$ show no discernible numerical differences (shown in Chapter 4).

3. A path is found when the distance between the current configuration of the

system $\mathbf{R}(t)$ and the second end point $\mathbf{R}_f$ is smaller than δ_{di}.

$$|\mathbf{R}_f - \mathbf{R}(t)| < \delta_{di} \tag{3.34}$$

The path length l is the sum of individual successful step lengths.

$$l = \sum_{t=0}^{t=P} |\mathbf{R}(t+1) - \mathbf{R}(t)| \tag{3.35}$$

where P is the total number of steps along the path, $\mathbf{R}(0) = \mathbf{R}_i$, $\mathbf{R}(P{+}1) = \mathbf{R}_f$.

The algorithm of path finding for hard sphere liquids is shown in Algorithm 3.

3.2.2.3 Optimization

Optimization is also needed for paths of hard sphere liquids for the same reason as that of soft particle liquids. The procedure is the same as in section 3.1.2.4.

Algorithm 3 Path finding for hard sphere systems

$E_L \leftarrow 0$
$l \leftarrow 0$ ▷ path length
$\mathbf{R}_t$ ▷ current configuration of the system
$\mathbf{R}_o$ ▷ previous allowed configuration of the system
$\mathbf{R}_t \leftarrow \mathbf{R}_i$, $\mathbf{R}_o \leftarrow \mathbf{R}_i$
while $|\mathbf{R}_f - \mathbf{R}_t| > \delta_{di}$ **do** ▷ $\delta_{di} = 0.01\sigma$
$\mathbf{R}_o \leftarrow \mathbf{R}_t$
$\mathbf{R}_t \leftarrow \mathbf{R}_t + \delta_{di}\dfrac{\mathbf{R}_f - \mathbf{R}_t}{|\mathbf{R}_f - \mathbf{R}_t|}$ ▷ direct step
  while $V(\mathbf{R}_t) > 0$ **do**
   $\mathbf{R}_t \leftarrow$ CollisionAvoidanceStep$(\mathbf{R}_o, \mathbf{R}_t)$ ▷ collision avoidance step
  end while
$l \leftarrow l + |\mathbf{R}_t - \mathbf{R}_o|$
end while
return l

procedure CollisionAvoidanceStep$(\mathbf{R}_o, \mathbf{R}_t)$
  $\mathbf{R}_o$ ▷ Previous allowed configuration
  $\mathbf{R}_t$ ▷ Configuration after the failed direct step
  $\mathbf{F}_j \leftarrow \vec{0}$ ▷ Fictitious force on particle j
  $\hat{\mathbf{g}}_j \leftarrow \vec{0}$ ▷ particle j's direction to move
  repeat
   $\mathbf{F}_j \leftarrow \mathbf{F}_j +$ FictitiousForce$(\mathbf{R}_t)$
   $\hat{g}_j = \dfrac{\mathbf{F}_j}{|\mathbf{F}_j|}$
   $\mathbf{R}_t \leftarrow \mathbf{R}_o + \delta_{ca}(\hat{\mathbf{g}}_1, ..., \hat{\mathbf{g}}_j, ..., \hat{\mathbf{g}}_N)$ ▷ $\delta_{ca} = 10^{-4}\sigma$
  until $V(\mathbf{R}_t) = 0$
return $\mathbf{R}_t$
end procedure

3.2.3 MD Calculation of Diffusion Coefficients

The diffusion coefficient D has the following relation with velocity autocorrelation function [3]

$$D = \frac{1}{3}\int_0^\infty \mathrm{d}t\langle \mathbf{v}_i(t)\cdot\mathbf{v}_i(0)\rangle \tag{3.36}$$

In calculation, the implementation for mono-disperse hard sphere liquid is

$$D = \frac{1}{3}\int_0^{t_{max}} \mathrm{d}t\langle \frac{1}{N}\sum_{i=1}^{N}\mathbf{v}_i(t)\cdot\mathbf{v}_i(0)\rangle \tag{3.37}$$

and for binary hard sphere mixture is

$$D_b = \frac{1}{3}\int_0^{t_{max}} \mathrm{d}t\langle \frac{1}{N_b}\sum_{i=1}^{N_b}\mathbf{v}_i(t)\cdot\mathbf{v}_i(0)\rangle \tag{3.38}$$

$$D_s = \frac{1}{3}\int_0^{t_{max}} \mathrm{d}t\langle \frac{1}{N_s}\sum_{i=1}^{N_s}\mathbf{v}_i(t)\cdot\mathbf{v}_i(0)\rangle \tag{3.39}$$

where N is the number of particles, b and s denote big and small spheres respectively, and the brackets $\langle\dots\rangle$ mean an average over different configurations used for values of $\mathbf{v}_i(0)$. t_{max} is chosen differently for each ϕ to be a time that is sufficiently long to ensure the convergence of the results.

By splitting the integration interval $[0, t_{max}]$ into n subintervals, n being an even number, each interval with size $\Delta t = \dfrac{t_{max}}{n}$, the integration in above equations can be calculated by Simpson's rule.

$$\int_0^{t_{max}} f(x)\mathrm{d}x \approx \frac{\Delta t}{3}\big[f(x_0) + 2\sum_{j=1}^{\frac{n}{2}-1} f(x_{2j}) + 4\sum_{j=1}^{\frac{n}{2}} f(x_{2j-1}) + f(x_n)\big] \tag{3.40}$$

$$x_0 = 0, \quad x_n = t_{max}, \quad x_j = j\Delta t \quad \text{for } j = 0, 1, \cdots, n \tag{3.41}$$

3.2.3.1 Collision dynamics of hard spheres

The molecular dynamics of hard sphere systems is based on collision dynamics [47]. Due to the singularity of the hard sphere potential, the exchange of momentum and energy among different particles only happen when they collide. Denote the current configuration of the system at time t as $\mathbf{R}(t) = (\mathbf{r}_1, \cdots, \mathbf{r}_N)$, where $\mathbf{r}_j$ $(j = 1, \cdots, N)$ is a 3 dimensional vector denoting the position of particle j. The velocity of sphere j is $\mathbf{v}_j$ $(j = 1, \cdots, N)$. For each two particles i and j (not overlapped at time t), we can calculate the time difference from now to the moment when they are about to collide, denoted as collision time t_{ij}.

Define

$$\mathbf{r}_{ij} = \mathbf{r}_j - \mathbf{r}_i, \quad \mathbf{v}_{ij} = \mathbf{v}_j - \mathbf{v}_i, \tag{3.42}$$

When sphere i and sphere j are about to collide, they are in contact with each other and the following equation is satisfied

$$|\mathbf{r}_{ij}(t + t_{ij})| = |\mathbf{r}_{ij} + \mathbf{v}_{ij}t_{ij}| = \frac{1}{2}(\sigma_i + \sigma_j) \tag{3.43}$$

Define $b_{ij} = \mathbf{r}_{ij} \cdot \mathbf{v}_{ij}$, $\sigma_{ij} = \frac{1}{2}(\sigma_i + \sigma_j)$, Equation 3.43 becomes

$$v_{ij}^2 t_{ij}^2 + 2b_{ij}t_{ij} + r_{ij}^2 - \sigma_{ij}^2 = 0 \tag{3.44}$$

Equation 3.44 is a quadratic equation in t_{ij}. By solving the quadratic equation, the collision time t_{ij} can be obtained.

If $b_{ij} > 0$, particle i and particle j are going away from each other. No collision happens between them.

If $b_{ij} < 0$ and $b_{ij}^2 - v_{ij}^2(r_{ij}^2 - \sigma_{ij}^2) < 0$, Equation 3.44 has complex roots. It means no collision occurs between particle i and j.

If $b_{ij} < 0$ and $b_{ij}^2 - v_{ij}^2(r_{ij}^2 - \sigma_{ij}^2) > 0$, Equation 3.44 has two positive roots. The smaller one is the collision time

$$t_{ij} = \frac{-b_{ij} - (b_{ij}^2 - v_{ij}^2(r_{ij}^2 - \sigma_{ij}^2))^{1/2}}{v_{ij}^2} \tag{3.45}$$

By iterating through all pairs of particles of the system, we know the collision time between any two particle t_{ij} $(i = 1, \cdots, N, j = i + 1, \cdots, N)$. Note $t_{ij} = t_{ji}$.

The earliest collision of the whole system from now is by the colliding pair that has the smallest value of t_{ij}. Denote the earliest colliding pair as particle m and particle n.

$$(m, n) = \arg\min_{i,j} t_{ij}, (i = 1, \cdots, N, j = i + 1, \cdots, N) \tag{3.46}$$

All particles are moved forward by time t_{mn}.

$$\mathbf{r}_j(t + t_{mn}) = \mathbf{r}_j(t) + t_{mn}\mathbf{v}_j, (j = 1, \cdots, N) \tag{3.47}$$

After this move, particle m and n are in contact and are about to collide. The total energy and momentum are both conserved during the elastic collision. Denote the change of velocity of particle m and n as $\delta\mathbf{v}_m$ and $\delta\mathbf{v}_n$ respectively. Because of the conversation of total linear momentum and kinetic energy, and each particle having the same mass, we have

$$\mathbf{v}_m(\text{after}) = \mathbf{v}_m(\text{before}) + \delta\mathbf{v}_m \tag{3.48}$$

$$\mathbf{v}_n(\text{after}) = \mathbf{v}_n(\text{before}) + \delta\mathbf{v}_n \tag{3.49}$$

$$b_{mn} = \mathbf{r}_{mn}(t + t_{mn}) \cdot \mathbf{v}_{mn}(t + t_{mn}) \tag{3.50}$$

$$\delta\mathbf{v}_m = -(b_{mn}/\sigma_{mn}^2)\mathbf{r}_{mn} \tag{3.51}$$

$$\delta \mathbf{v}_n = -\delta \mathbf{v}_m \tag{3.52}$$

Note b_{mn} is reevaluated in Equation 3.50 at the moment of collision $(t + t_{mn})$.

After the collision, the system has an updated configuration and velocity. New colliding pair is calculated from above procedure and the system is propagated forward accordingly.

3.2.3.2 Procedures and Parameters

The calculation is performed in reduced units. Reduced time is $t^* = t(\frac{k_B T}{m\sigma^2})^{\frac{1}{2}}$ and the reduced diffusion coefficient D^* is

$$D^* = \frac{D}{(\frac{k_B T}{m\sigma^2})^{\frac{1}{2}}\sigma^2} \tag{3.53}$$

1. Mono-disperse hard sphere system

   The system is first set up as a face centered crystal. The initial velocities is set by random numbers taken from Maxwell-Boltzman distribution, adjusted to remove the net momentum of the system and rescaled by $\sum_{i=1}^{N} \frac{1}{2} m \mathbf{v}_i^2 = \frac{3}{2} N k_B T$, where in calculation $m = 1.0$, $k_B T = 1.0$. The system is equilibrated with 10^7 MD steps based on collision dynamics [47]. Each trajectory records a configuration every time interval Δt, and records in total 10^5 configurations. The time interval Δt between two consecutively recorded configurations are chosen differently for different ϕ to ensure convergence of results. Choose initial configuration for velocity correlation as every 10 recorded configurations. So each trajectories offers 10^4 configurations as the starting configuration of velocity correlation.

   We propagate 10^5 MD steps between two consecutive trajectories to avoid correlations among trajectories. The reduced diffusion coefficient D^* at each packing fraction ϕ is averaged over 5 such trajectories.

The parameters of t_{max}, Δt and n for mono-disperse hard sphere system are given in Table 3.1.

ϕ	Δt	n	t_{max}
0.05	0.0010	30000	30
0.10,0.15	0.00050	30000	15
0.20,0.25	0.00020	30000	6
0.30,0.35	0.00010	30000	3
0.40,0.45	0.000050	30000	1.5
0.46-0.48	0.000030	30000	0.9

ϕ : packing fraction
Δt : time between two consecutively sampled configurations
n : number of intervals in Simpson's rule
t_{max} : upper limit of time for calculating velocity correlation

Table 3.1: Parameters in reduced unit for the calculation of diffusion coefficient of mono-disperse hard sphere system.

2. binary hard sphere liquid

For $\phi < 0.50$, the system is first set up as a face centered crystal structure, with big and small spheres occupying different halves. The initial velocities are set by random numbers taken from Maxwell-Boltzman distribution, adjusted to remove the net momentum of the system, then rescaled by $\sum_{i=1}^{N} \frac{1}{2} m \mathbf{v}_i^2 = \frac{3}{2} N k_B T$, where in calculation $m = 1.0$, $k_B T = 1.0$. Then the system is equilibrated with 10^7 MD steps based on collision dynamics [47] before collecting data. Each trajectory records a configuration every time interval Δt and records in total $1.5 * 10^5$ configurations. Δt is chosen differently for different ϕ to ensure the convergence of results. The velocity correlation is calculated with initial configuration every 10 recorded configurations. So each trajectory offers $1.5 * 10^4$ configurations as the starting configuration of velocity correlation. We propagate $2 * 10^5$ MD steps between two consecutive trajectories to avoid correlations among different trajectories. The reduced diffusion coefficient D^* is averaged

over 10 such trajectories.

For $\phi \geq 0.50$, the system is first set up as a face centered crystal structure of packing fraction $\phi_{in} = 0.50$, with big and small spheres occupying different halves. This is because an fcc structure of higher packing fraction with this arrangement of big and small spheres would have overlapping particles. The system is then compressed to the desired packing fraction ϕ by mechanical contraction method [53]. The procedure is as follows. For one compression, the simulation box is compressed from its current volume V_0 to a volume $V = 0.9990V_0$. Then we rescale the position of every sphere to put every sphere back into the simulation box. In the case of overlapped spheres after rescaling the positions, the overlapped pairs of spheres are pulled away along the line of the centers of the two spheres from each other to just avoid overlapping. Then we propagate the system with 2000 Monte Carlo steps [54]. One Monte Carlo step here means giving each of the N spheres in the system one trial move $\delta\mathbf{r}$ sequentially. $\delta\mathbf{r} = (\delta x, \delta y, \delta z)$, $-0.10\sigma \leq \delta x \leq 0.10\sigma, -0.10\sigma \leq \delta y \leq 0.10\sigma, -0.10\sigma \leq \delta z \leq 0.10\sigma$. A trial move is accepted if it does not cause any overlaps and is rejected otherwise. After this, compress the system again. The process is repeated until the desired density ϕ is reached. Usually this generates a configuration of which the density is slightly bigger than the desired one. In this case, the simulation box is enlarged to make the density be exactly the desired value. No rescaling of positions of spheres is needed after enlargement because every sphere is still in the simulation box.

After mechanical contraction, the system is of a configuration of desired packing fraction. Then we set the initial velocities of particles in the system by random numbers from Maxwell-Boltzman distribution. The velocities are shifted to remove the net momentum of the system, then rescaled by $\sum_{i=1}^{N} \frac{1}{2} m \mathbf{v}_i^2 = \frac{3}{2} N k_B T$, where in calculation $m = 1.0$, $k_B T = 1.0$. The system is then equilibrated with 10^7 MD steps based on collision dynamics [47] before collecting data. Each tra-

jectory records a configuration every time interval Δt and records in total $2*10^5$ configurations. Δt is chosen differently for different ϕ to ensure the convergence of the results. The velocity correlation is calculated with initial configuration every 100 recorded configurations. So each trajectories offers $2 * 10^3$ configurations as the starting configuration of velocity correlation. We propagate $2 * 10^5$ MD steps between two consecutive trajectories. The reduced diffusion coefficient D^* is averaged over 10 such trajectories.

The parameters of t_{max}, Δt and n for binary hard sphere liquid are given in Table 3.2.

ϕ	Δt	n	t_{max}
0.05	0.00060	40000	24
0.10,0.15	0.00040	40000	16
0.20,0.25	0.00020	40000	8
0.30,0.35	0.00015	40000	6
0.40,0.45	0.000010	40000	4
0.50-0.58	0.000002	100000	2

ϕ : packing fraction
Δt : time between two consecutively sampled configurations
n : number of intervals in Simpson's rule
t_{max} : upper limit of time for calculating velocity correlation

Table 3.2: Parameters used in reduced unit for calculation of diffusion coefficient of binary hard sphere system.

Chapter 4

Results

This chapter presents results of the geodesic theory for hard sphere systems. It shows geodesic theory predicts how dynamics slows down for hard sphere systems, as well as some other features of dynamics. Through these results, along with comparison with a soft particle liquid, geodesic theory proves that what is essential in the change of dynamics in liquids is that available global paths are getting longer. Tests of parameters and results of molecular dynamics calculation of diffusion coefficient are given at the end of the chapter.

4.1 Convergence of Geodesic Path Length

4.1.1 Convergence with ΔR

Recall that the geodesic theory predicts diffusion coefficient by

$$D = \lim_{\Delta R \to \infty} D_0 \overline{(\Delta R/g)^2} \tag{4.1}$$

$$D \propto \overline{(\Delta R/g)^2} \tag{4.2}$$

The above equations work in the limit of $\Delta R \to \infty$. Therefore, we first need to ensure the geodesic path is converged with respect to ΔR before generating further

results and analysis.

What we need to do is to find a ΔR that is large enough so that the value of $(\Delta R/g)^2$ reaches its limit value. Fig. 4.1 and Fig. 4.2 show the convergence of $(\Delta R/g)^2$ with respect to ΔR for mono disperse and binary hard sphere system respectively.

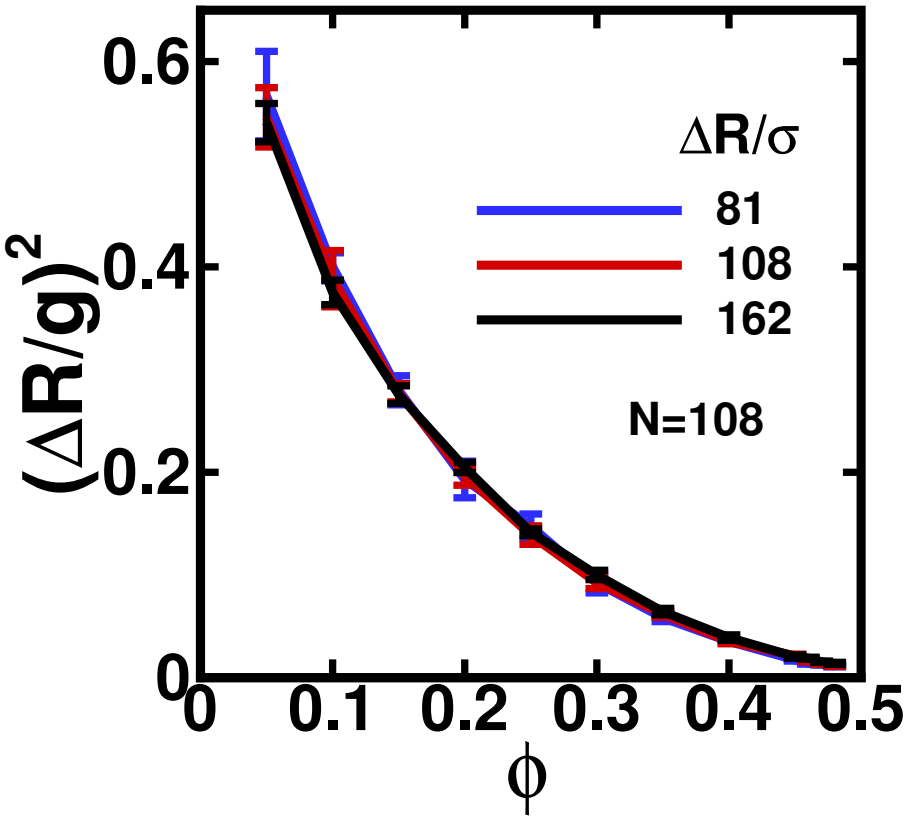

Figure 4.1: Convergence of $(\frac{\Delta R}{g})^2$ with respect to ΔR for the mono disperse hard sphere system. The packing fraction ϕ goes from 0.05 to 0.48. The mono disperse system studied here is of size $N = 108$. The results are averaged over 5 unoptimized paths. The figure shows that $(\frac{\Delta R}{g})^2$ is well converged with ΔR. $\Delta R = 108\sigma$ is large enough to have converged results for $N = 108$ for the mono disperse hard sphere system.

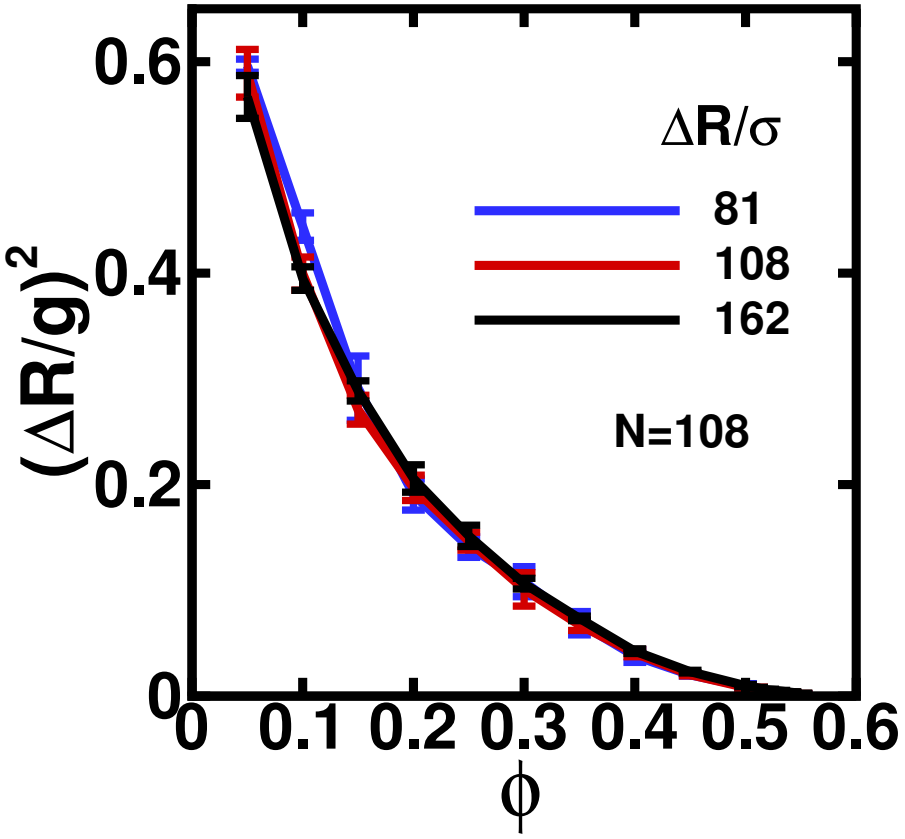

Figure 4.2: Convergence of $(\frac{\Delta R}{g})^2$ with respect to ΔR for the binary hard sphere system. The packing fraction ϕ goes from 0.05 to 0.55. The binary system studied here is of size $N = 108$. The results are averaged over 5 unoptimized paths. The figure shows that $(\frac{\Delta R}{g})^2$ is well converged with ΔR. $\Delta R = 108\sigma$ is large enough to have converged results for $N = 108$ for the binary hard sphere system.

4.1.2 Convergence with N

We also check the finite size effect of the results. A converged value of $(\Delta R/g)^2$ means it should not change with system size N. Because $\Delta R = \sqrt{\sum_{j=1}^{N}(\mathbf{r}_j^f - \mathbf{r}_j^i)^2} \propto \sqrt{N}$, if we fix per-particle displacement across different system sizes, ΔR can be chosen accordingly. Since we know $\Delta R = 108\sigma$ is large enough to have converged results for $N = 108$ for both systems from Fig. 4.1 and Fig. 4.2, ΔR is chosen so that $\Delta R/\sqrt{N} = 10\sigma$. Fig. 4.3 and Fig. 4.4 show the convergence of $(\Delta R/g)^2$ with respect to N for both systems.

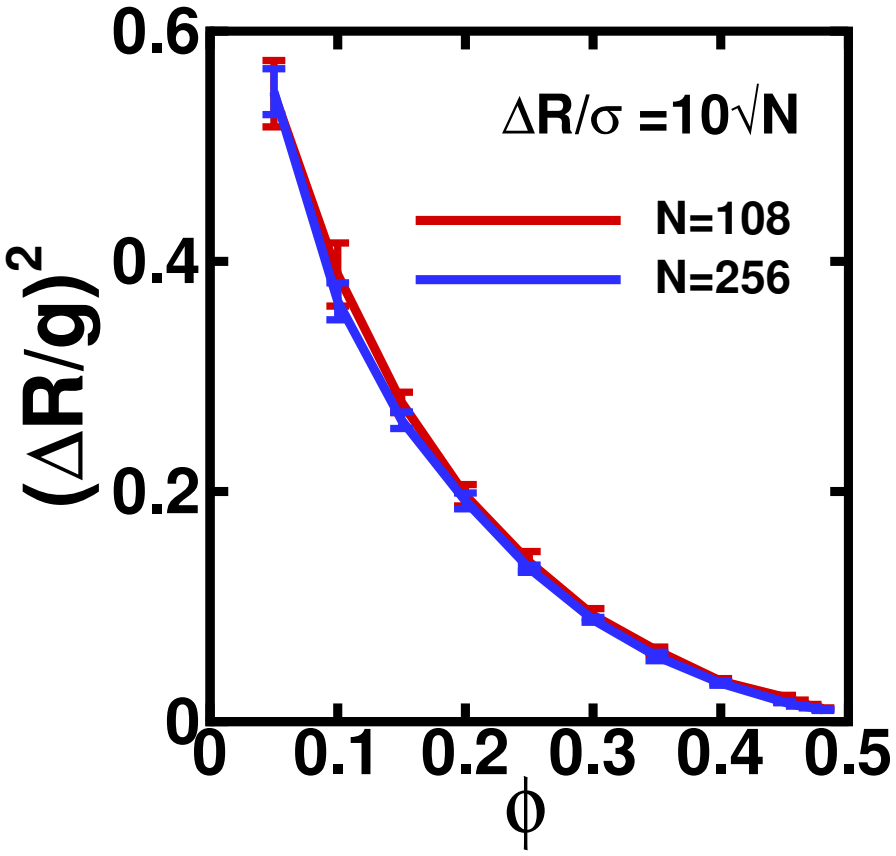

Figure 4.3: Convergence of $(\frac{\Delta R}{g})^2$ with respect to N for the mono disperse hard sphere system. The results are averaged over 5 unoptimized paths. The figure shows that there is no finite size effect in the results.

Fig. 4.1, Fig. 4.2, Fig. 4.3 and Fig. 4.4 serve as a check of the validity of the geodesic paths. For a giving packing fraction ϕ, the converged geodesic path length scales with ΔR, and the ratio $(\frac{\Delta R}{g})^2$ does not change with N when keeping the distance travelled per particle fixed. The figures show that the geodesic paths behave as we expect.

What Fig. 4.1, Fig. 4.2, Fig. 4.3 and Fig. 4.4 show more is that, when increasing the density ϕ, the geodesic path lengths g are getting longer with respect to the net distance ΔR travelled by the system, reflected in the decreasing trend of $(\frac{\Delta R}{g})^2$. They show that the available paths in configuration space do get longer with increasing density.

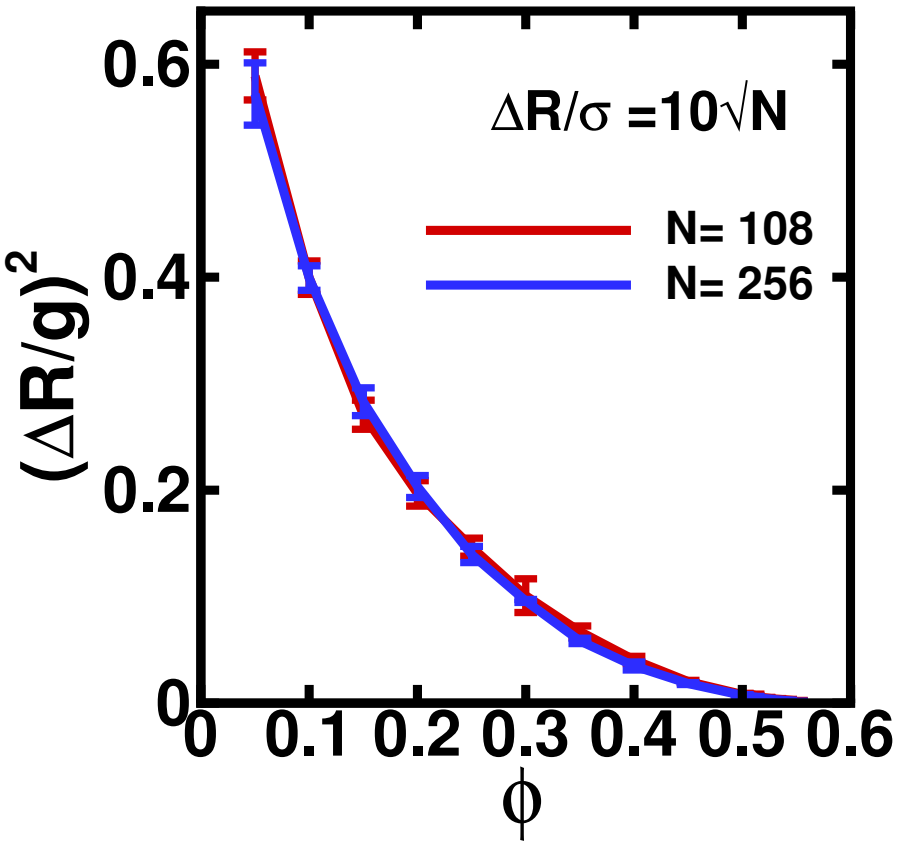

Figure 4.4: Convergence of $(\frac{\Delta R}{g})^2$ with respect to N for the binary hard sphere system. The results are averaged over 5 unoptimized paths. The figure shows that there is no finite size effect in the results.

4.2 Optimization

The paths are shorter after optimization, as shown in Fig. 4.5 and Fig. 4.6. For both systems, the path lengths are shorter on the rough order of 10% after optimization.

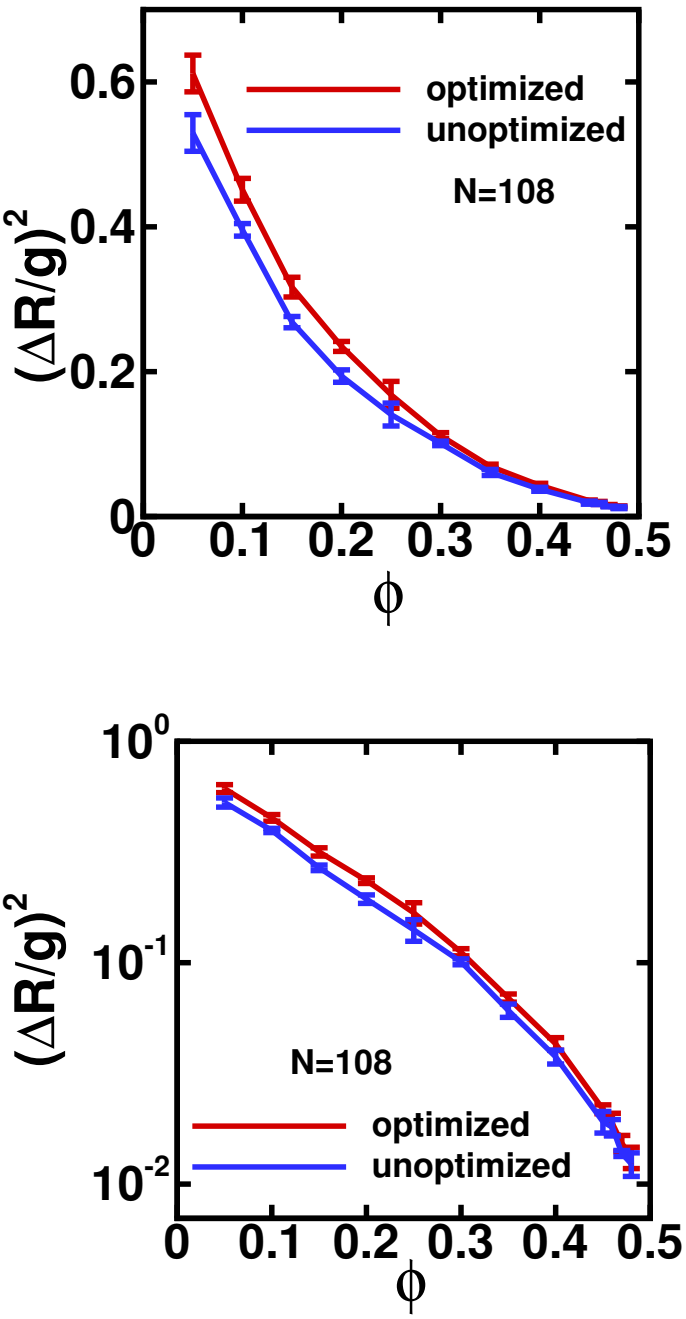

Figure 4.5: Comparison of path lengths of unoptimized paths and optimized paths of the mono disperse hard sphere system. The upper panel is the comparison in linear scale and the lower panel is the same curve on log scale. The results are averaged over 5 paths of $\Delta R = 108\sigma$ and $N = 108$.

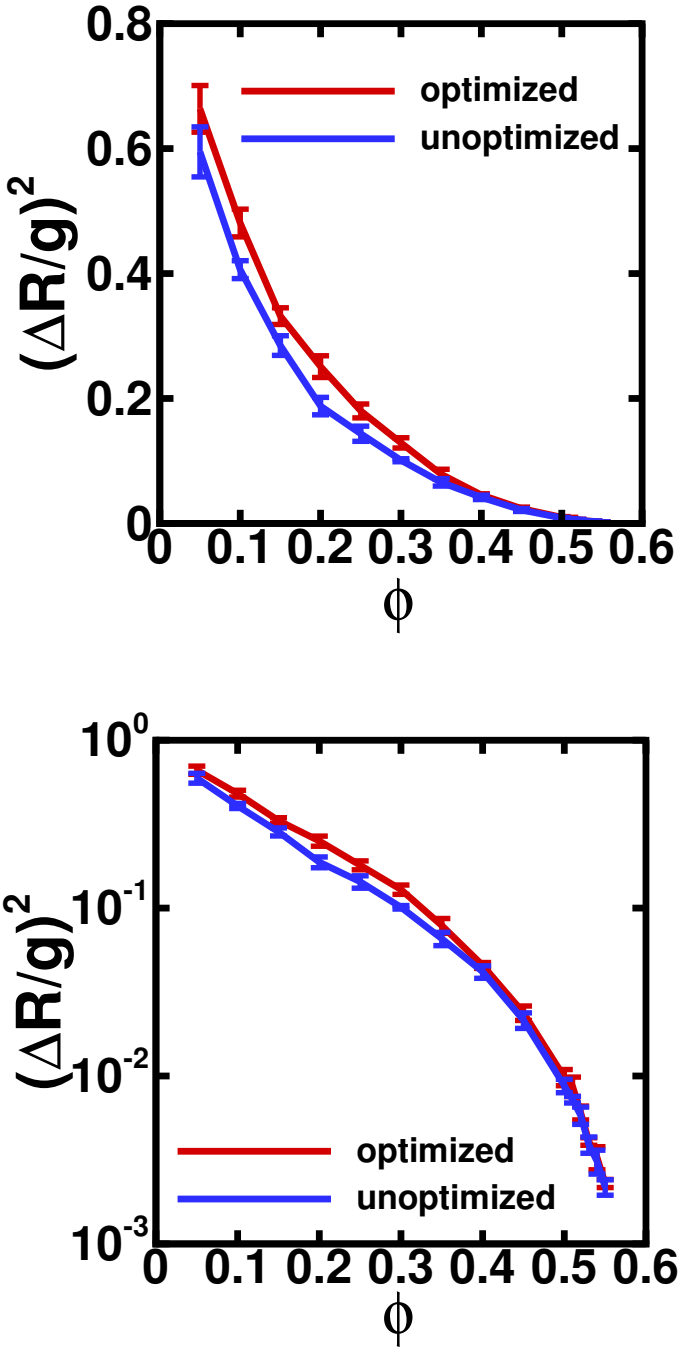

Figure 4.6: Comparison of path lengths of unoptimized paths and optimized paths of the binary hard sphere system. The upper panel is the comparison in linear scale and the lower panel is the same curve on log scale. The results are averaged over 5 paths of $\Delta R = 108\sigma$ and $N = 108$.

4.3 Dynamics Slowing down

How well do the geodesic paths predict dynamics for liquids? We utilize Equation 4.2 to predict diffusion coefficient from landscape geodesics. Fig. 4.7 and Fig. 4.8 show that the landscape geodesic theory predicts dynamics slowing down in simple liquid - the mono disperse hard sphere system.

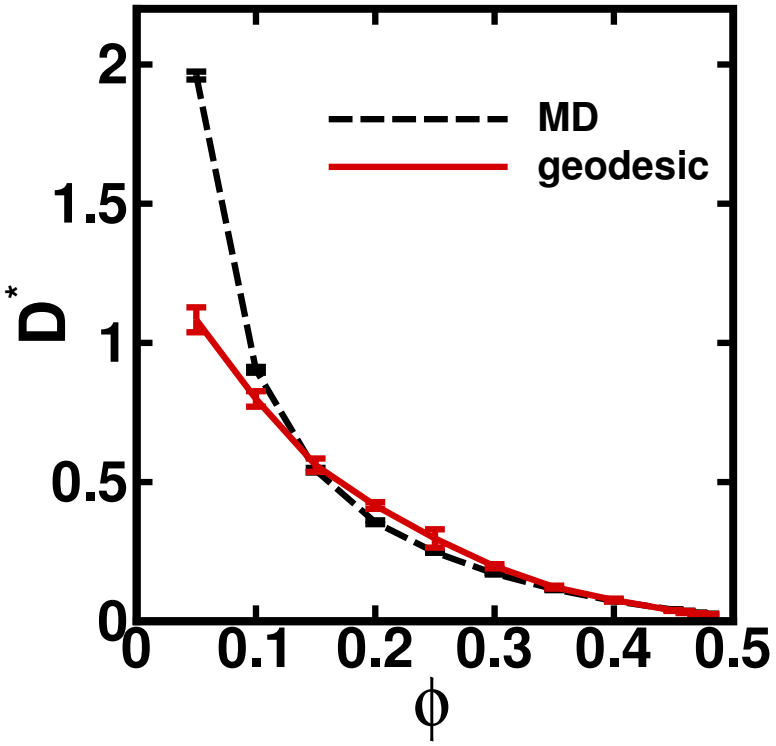

Figure 4.7: The reduced diffusion coefficient D^* as a function of density ϕ for mono disperse hard sphere liquid. The density ϕ goes from 0.05 to 0.48. The dashed black line is precise results from molecular dynamics calculation. The red solid line is the prediction from geodesic theory. According to $D \propto \overline{(\Delta R/g)^2}$, the two curves are collapsed together by multiplying $\overline{(\Delta R/g)^2}$ by an overall constant. The overall constant is chosen to be the average of the value of $D^*/\overline{(\Delta R/g)^2}$ at different ϕ. The geodesic result is averaged over 5 optimized paths of $\Delta R = 108\sigma$ and $N = 108$ for each density. By comparing the results from MD and geodesics, the figure shows that geodesic theory predicts dynamics slowing down accurately.

Not only can geodesic theory predict dynamics slowing down for simple liquids, it is also able to predict dynamics slowing down in glass-forming liquids. Fig. 4.9 and Fig 4.10 show that the landscape geodesic theory captures the slowing down of

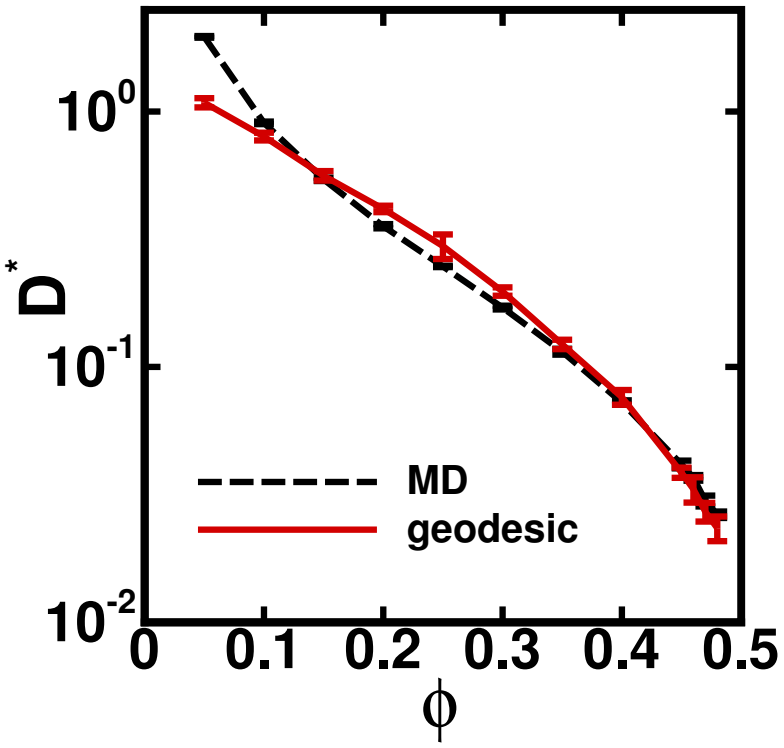

Figure 4.8: Log scale of Fig 4.7. With increasing density ϕ towards the freezing point, the reduced diffusion coefficient D^* drops by two orders of magnitude. Geodesic theory captures the change in dynamics over multiple orders of magnitude.

dynamics for the glass-forming binary hard sphere liquid.

Through Fig. 4.7, Fig. 4.8, Fig. 4.9 and Fig. 4.10, this section shows that geodesic theory is able to predict dynamics with pure landscape information only, without any reliance on dynamical details. The global features of the potential energy landscape are sufficient to predict dynamical trends. The rate of growth of the geodesic path lengths quantitively captures the rate of dynamics slowing down.

Moreover, geodesics being able to predict dynamics is what we expect if they are the inherent dynamics of a system. This is the first test to prove that the geodesics represent the inherent dynamics of a system.

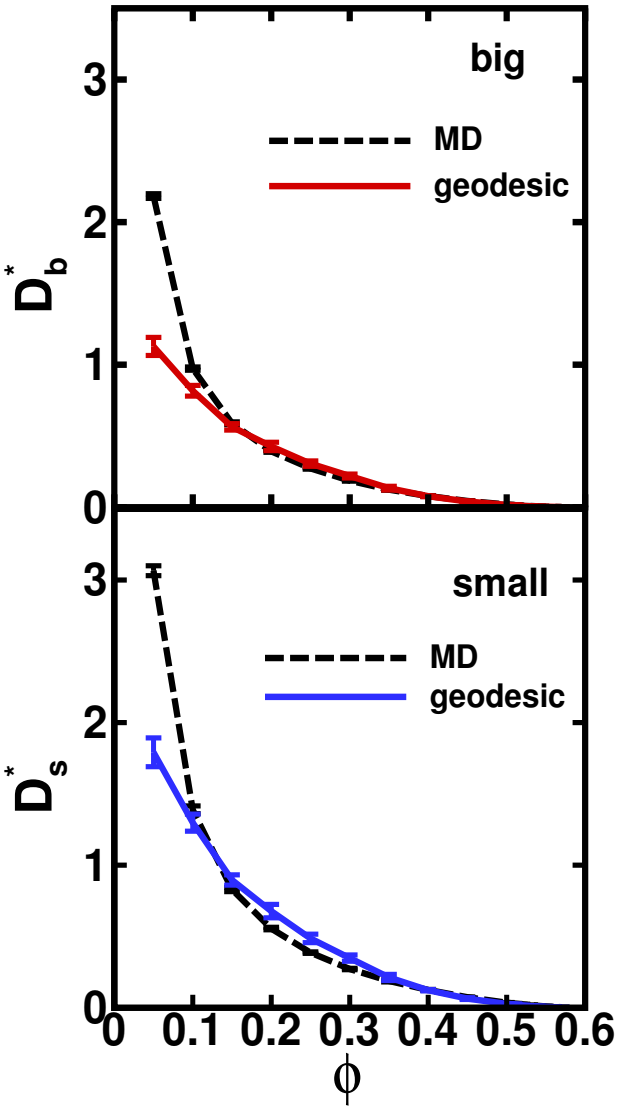

Figure 4.9: The reduced self diffusion coefficient D^* as a function of density ϕ for each component of the binary hard sphere liquid, the upper panel for big spheres(D_b^*) and the lower panel for small spheres(D_s^*). In both panels, the dashed lines are precise results from molecular dynamics calculation(MD), and the solid lines are the prediction from geodesic theory(geodesic). The density ϕ goes from 0.05 to 0.57. The geodesic result uses the overall path length of the whole system, and is averaged over 5 paths of $\Delta R = 108\sigma$ and $N = 108$ using optimized paths for density up to 0.55 and unoptimized paths for $\phi = 0.56, 0.57$. The curves in each panel are collapsed together by multiplying $\overline{(\Delta R/g)^2}$ by an overall constant, which is chosen to be the average of the value of $D_b^*/\overline{(\Delta R/g)^2}$ and $D_s^*/\overline{(\Delta R/g)^2}$ at different ϕ respectively. By comparing the results from MD and geodesics, the figure shows that geodesic theory predicts dynamics slowing down accurately.

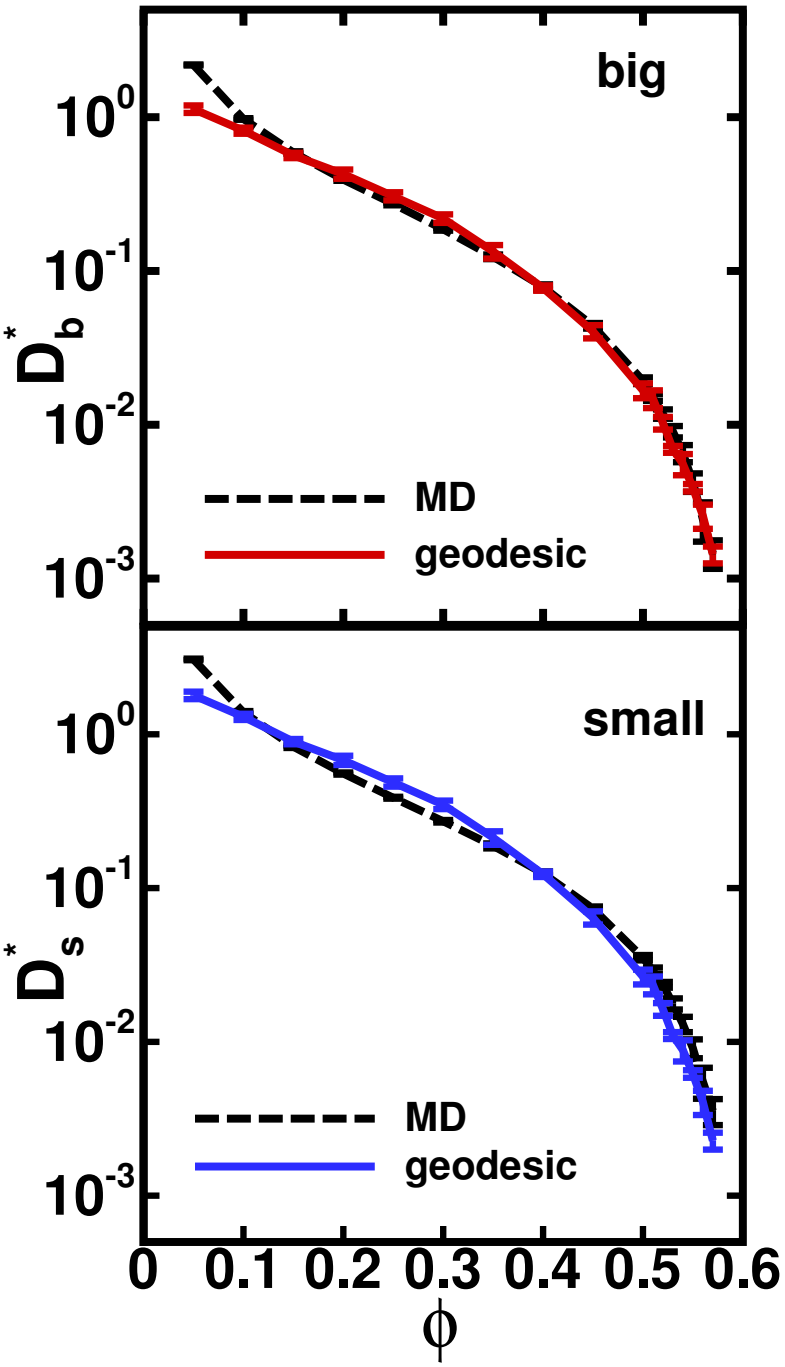

Figure 4.10: Log scale of Fig 4.9. With increasing density ϕ towards the mode coupling transition, the reduced diffusion coefficient D^* drops by four orders of magnitudes. Geodesic theory captures the change in dynamics across multiple orders of magnitude.

4.4 Dynamic Heterogeneity

What other dynamical information is embedded in the geodesics? In this section, by studying further the glass-forming binary hard sphere system, we show that geodesic paths also contain information about dynamic heterogeneity.

For a Gaussian diffusion, the single particle displacement $\delta r_j(t)$ obeys a Gaussian distribution, and the logarithm of single particle displacement

$$\log_{10}(\delta r_j(t)) = \log_{10} |\mathbf{r}_j(t) - \mathbf{r}_j(0)| \tag{4.3}$$

has a probability distribution $P(\log_{10}(\delta r), t)$ that is independent of time [55]. In [24], it is shown that the distribution $P(\log_{10}(\delta r), t)$ of the same binary hard sphere system broadens with increasing density ϕ, and gains bimodality when ϕ reaches 0.58. The increasing width of the distribution is a sign of developing non-Fickian motion [24], and the bimodality at high ϕ shows there are groups of spheres with distinct dynamics in the system [24].

Geodesics should contain information about dynamic heterogeneity if it reveals inherent dynamics. Since the small particle and big particle are already two different groups in the system, we only look at one species here to exclude the possibility of "fake" dynamic heterogeneity from mixed species. Because at high density small spheres have a higher mobility than big spheres, the trend should be more obvious in small spheres, so we study the dynamic heterogeneity in small spheres.

Dynamic heterogeneity should appear in geodesics if different particles contribute differently to the geodesics. One measure is the geodesic distance g_j traveled by each particle scaled by the net end-to-end displacement ΔR_j it has made. In analogy to Equation 4.3, the logarithm of the quantity is

$$\log_{10}(\delta_{js}) = \log_{10}(\frac{g_{js}}{\Delta R_{js}}) \tag{4.4}$$

where the subscript s means small spheres, and the subscript j labels each of them, $j = 1, \cdots, N_s$.

The probability density distribution $P(\log_{10}(\delta_{js}))$ has width Δ

$$\Delta = \left\langle (\log_{10}(\delta_{js}) - \langle \log_{10}(\delta_{js}) \rangle)^2 \right\rangle^{\frac{1}{2}} \tag{4.5}$$

where $\langle \cdots \rangle$ denote ensemble average.

The width Δ of the distribution should increase with density ϕ if dynamic heterogeneity is contained in geodesics. To calculate the distribution and the width, we use 50 unoptimized paths of $\Delta R_s = 90\sigma$ and $N = 108$. R_s is the net distance travelled by small spheres,

$$\Delta R_s = \sqrt{\sum_{j=1}^{N_s} (\mathbf{r}_{js}^f - \mathbf{r}_{js}^i)^2} \tag{4.6}$$

$\Delta R_s = 90\sigma$ corresponds to a value of ΔR of the whole system slightly bigger than 108σ, so we expect the results to be converged. The distribution is done by histogram [56] with bin width 0.05.

The result is shown in Fig. 4.11. It demonstrates that geodesics reveal the growth of dynamic heterogeneity with increasing density.

Unoptimized paths are used because of the limitation of computational time. Comparison of the distributions from optimized paths and unoptimized paths shows no discernible difference, as shown in Fig. 4.12.

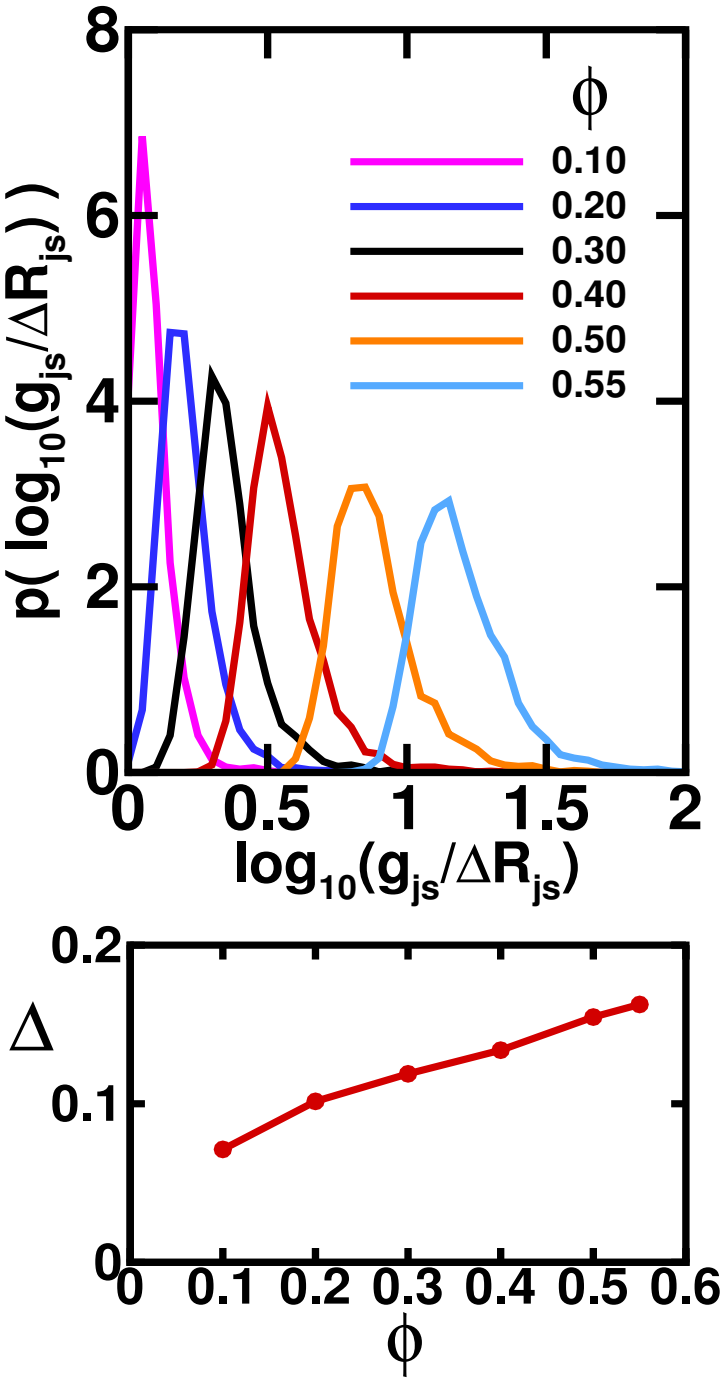

Figure 4.11: Growth of dynamic heterogeneity revealed by geodesics. The upper panel shows the distributions of $\log_{10}(\frac{g_{js}}{\Delta R_{js}})$ for different densities $\phi = 0.10, 0.20, 0.30, 0.40, 0.50, 0.55$, with ϕ increasing from left to right. The lower panel shows that the width Δ of the distributions increases with ϕ. The result is averaged over 50 unoptimized paths of $\Delta R_s = 90\sigma$ and $N = 108$.

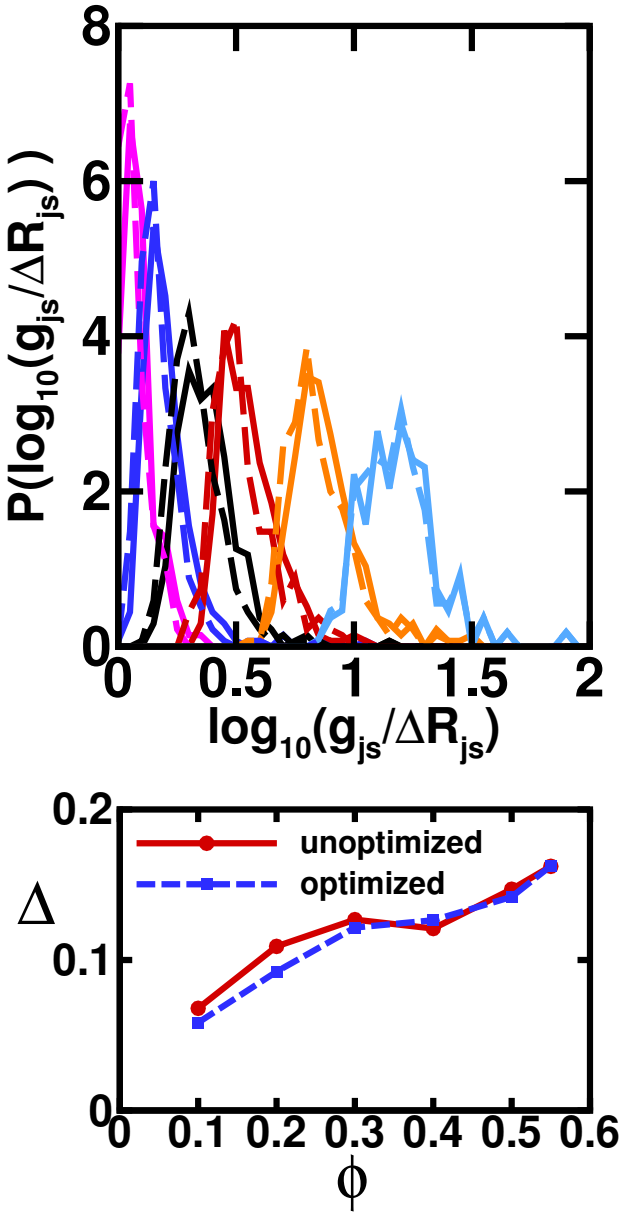

Figure 4.12: Comparison of $P(\log_{10}(\frac{g_{js}}{\Delta R_{js}})$ and the distribution width Δ from optimized paths and unoptimized paths. In both panels the solid lines represent results from unoptimized paths and the dashed lines are for optimized results. In the upper panel the density ϕ for each curve is $0.10, 0.20, 0.30, 0.40, 0.50, 0.55$ respectively, with ϕ increasing from left to right, the same as in Fig. 4.11. Both unoptimized and optimized results are averaged over 5 paths of $\Delta R_s = 90\sigma$ and $N = 108$. The distribution of $\log_{10}(\frac{g_{js}}{\Delta R_{js}})$ shifts towards left slightly after optimization, as the optimized paths are shorter. But the change of the width Δ is within fluctuations.

4.5 Participation Ratio

The participation ratio is studied to learn about the average number of particles contributing to the geodesics [39].

Generally, for a motion of a system from configuration $\mathbf{R}(t) = (\mathbf{r}_1(t), \cdots, \mathbf{r}_j(t), \cdots, \mathbf{r}_N(t))$ to configuration $\mathbf{R}(t+\delta t) = (\mathbf{r}_1(t+\delta t), \cdots, \mathbf{r}_j(t+\delta t), \cdots, \mathbf{r}_N(t+\delta t))$ in a very small time interval δt, the participation number n is

$$n(t) = 1/\sum_{j=1}^{N} |\mathbf{c}_j(t)|^4 \tag{4.7}$$

$$\delta\hat{\mathbf{R}}(t) = \frac{\mathbf{R}(t+\delta t) - \mathbf{R}(t)}{|\mathbf{R}(t+\delta t) - \mathbf{R}(t)|} = \sum_{j\mu} c_{ju}(t)|j\mu\rangle = \sum_{j=1}^{N} \mathbf{c}_j(t)|j\rangle \tag{4.8}$$

$$\mathbf{c}_j^2(t) = \dot{\mathbf{r}}_j^2(t)/\sum_{i=1}^{N} \dot{\mathbf{r}}_j^2(t) \tag{4.9}$$

$$\dot{\mathbf{r}}_j(t) = \frac{\mathbf{r}_j(t+\delta t) - \mathbf{r}_j(t)}{\delta t} \tag{4.10}$$

$$\sum_{j=1}^{N} |\mathbf{c}_j(t)|^2 = 1 \tag{4.11}$$

where j labels the particles and $\mu = x, y, z$ labels the Cartesian coordinates.

The participation ratio $\frac{n}{N}$, N being the system size, is usually used to measure the degree of localizations of motions [57] in a system. In an extreme case where there are m particles in a system contributing equally to a motion and the other $N-m$ particles not contributing at all , we would have $n = m$.

$$\mathbf{c}_j^2 = \begin{cases} \frac{1}{m} & \text{if } j \text{ is one of the } m \text{ particles} \\ 0, & \text{if } j \text{ is one of the } N-m \text{ particles} \end{cases} \tag{4.12}$$

$$n = 1/\sum_{j=1}^{N} |\mathbf{c}_j(t)|^4 = m \tag{4.13}$$

Thus this participation ratio measures the effective number of particles moving in any one step along the path.

The participation number n of a geodesic is the participation number per step averaged over the entire path.

$$n = \langle n(\tau) \rangle = \int_0^1 \mathrm{d}\tau n(\tau) \tag{4.14}$$

where τ is the progress along the path.

In implementation, the participation number of a path is calculated as follows. Denote the total path length as g, the total number of steps along the path as P, the length of each step t as $s(t)$, t being the index of steps along the paths, $t = 0, 1, \cdots, P$, $\mathbf{R}(0) = \mathbf{R}_i$, $\mathbf{R}(P+1) = \mathbf{R}_f$.

$$g = \sum_{t=0}^{P} s(t) \tag{4.15}$$

$$s(t) = |\mathbf{R}(t+1) - \mathbf{R}(t)| \tag{4.16}$$

The participation number n of the whole path is

$$n = \frac{\sum_{t=0}^{P}(s(t) \cdot n(t))}{g} \tag{4.17}$$

The participation number $n(t)$ of step t in implementation is

$$n(t) = 1/\sum_{j=1}^{N} |\mathbf{c}_j(t)|^4 \tag{4.18}$$

$$\delta\hat{\mathbf{R}}(t) = \frac{\mathbf{R}(t+1) - \mathbf{R}(t)}{|\mathbf{R}(t+1) - \mathbf{R}(t)|} = \sum_{j\mu} c_{ju}(t)|j\mu\rangle = \sum_{j=1}^{N} \mathbf{c}_j(t)|j\rangle \tag{4.19}$$

$$\mathbf{c}_j^2(t) = \dot{\mathbf{r}}_j^2(t) / \sum_{i=1}^{N} \dot{\mathbf{r}}_j^2(t) \tag{4.20}$$

$$\dot{\mathbf{r}}_j(t) = \mathbf{r}_j(t+1) - \mathbf{r}_j(t) \tag{4.21}$$

Fig. 4.13 shows that the participation number n scales linearly with N, meaning the motion along the geodesics is macroscopic.

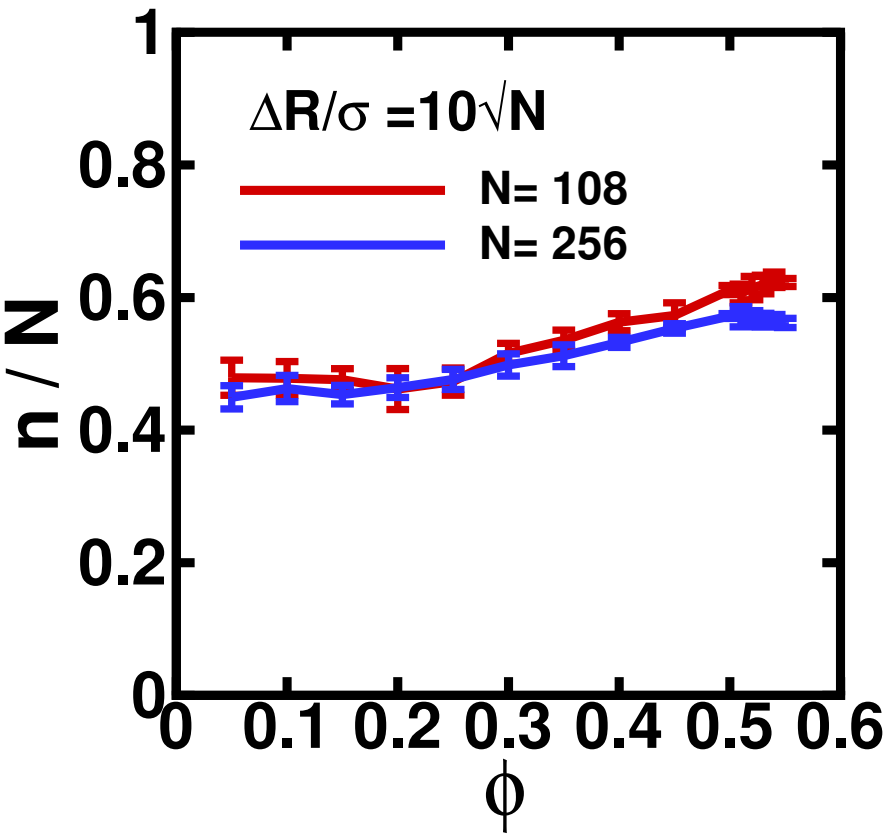

Figure 4.13: Participation ratio n/N as a function of density ϕ for different system sizes $N = 108$ and $N = 256$. The results are averaged over 5 unoptimized paths. The figure shows that the participation ratio does not depend on N. The motion is therefore macroscopic along geodesics.

The unoptimized paths are used in Fig. 4.13 for computational convenience. Participation number does not vary much after optimization, as shown in Fig. 4.14.

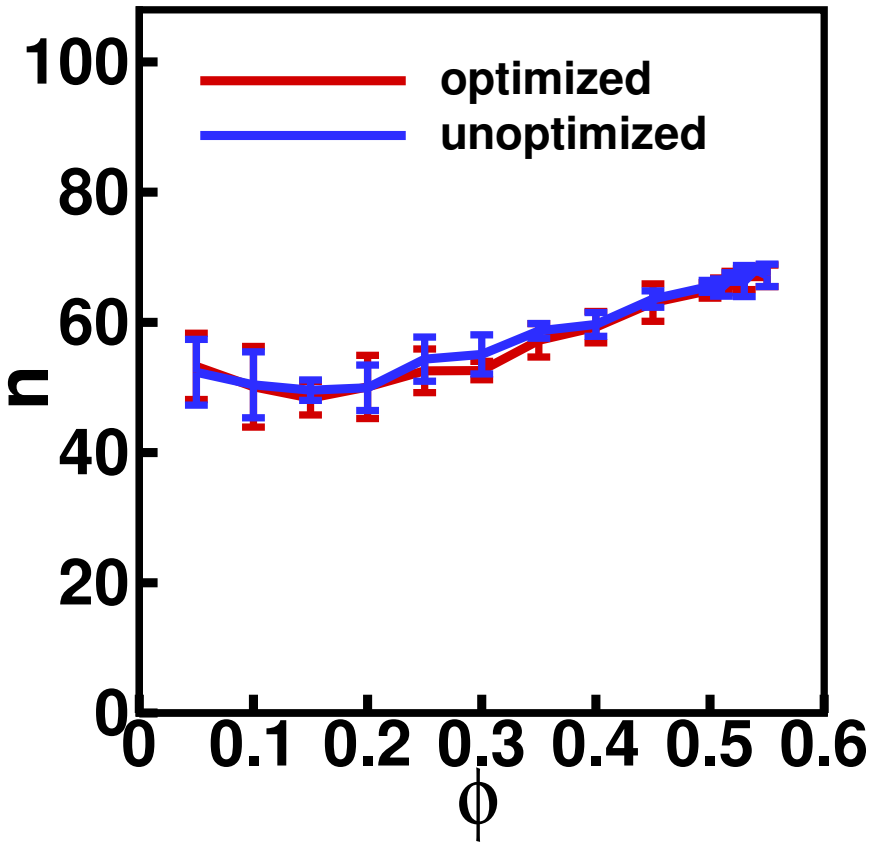

Figure 4.14: Participation number n as a function of density ϕ before and after optimization. The results are averaged over 5 paths of $N = 108$ and $\Delta R = 108\sigma$. The figure shows that the participation number does not vary much after optimization.

By comparing the participation ratio of the binary hard sphere liquid and soft particle Kob-Andersen liquid, we show that the motion for both systems is macroscopic, as shown in Fig. 4.15. In both systems, a significant fraction of the system moves, even in the most efficient pathways.

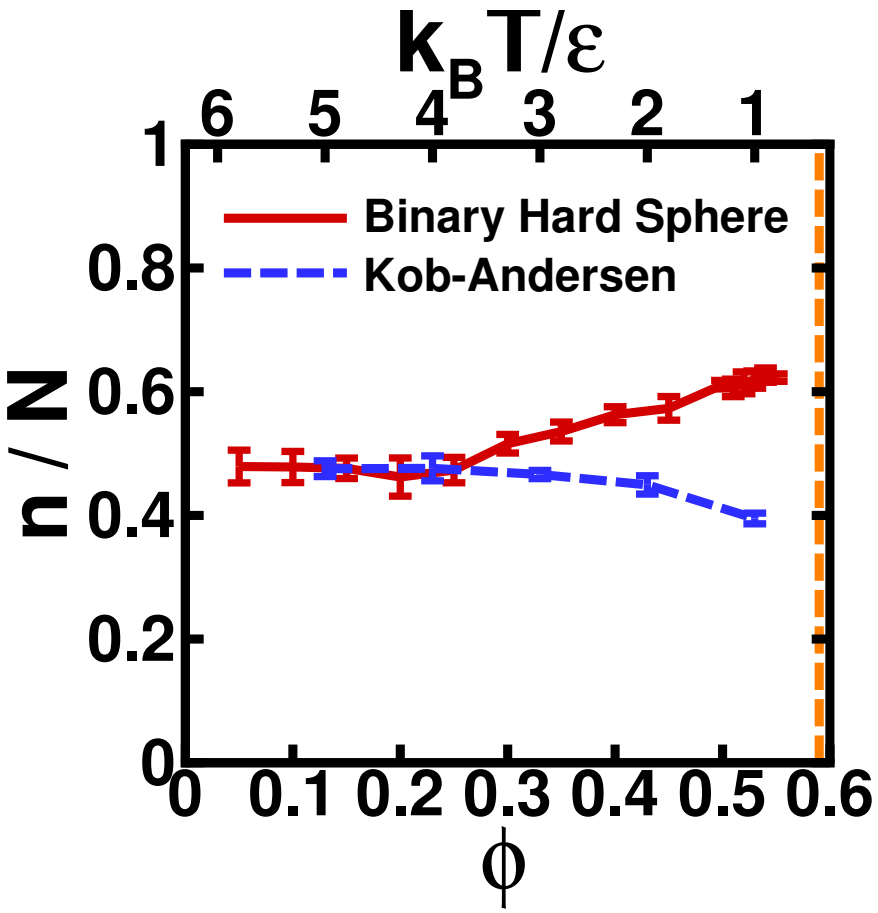

Figure 4.15: Participation ratios n/N of the binary hard sphere liquid and Kob-Andersen liquid, as a function of ϕ and k_BT/ϵ_{AA} respectively. The vertical dashed line is the mode coupling transition for both systems. The results for both systems are averaged over 5 optimized paths of $\Delta R = 108\sigma$ and $N = 108$. The motion along geodesics for the two systems are both macroscopic.

4.6 Non-Gaussian Parameter

In Fig. 4.15, it is shown that the motion along the geodesics is macroscopic for both hard and soft particle systems. However, there is a slightly different trend of the participation ratio when the system approaches the mode coupling transition. Is this difference related to the nature of the geodesics or the potential energy landscape? This section studies the participation ratio of each step $n(t)$ to take a more detailed look at the geodesic paths.

Recall the non-Gaussian parameter α_2 is

$$\alpha_2(t) = \frac{3}{5}\frac{\langle \delta r_j^4(t) \rangle}{\langle \delta r_j^2(t) \rangle^2} - 1 \tag{4.22}$$

where $\delta r(t) = |\mathbf{r}_j(t) - \mathbf{r}_j(0)|$ is the displacement of particle j during time t.

Besides the fact that α_2 measures how non-Gaussian the distribution of single particle displacements is, α_2 is also related to the participation ratio $\frac{n}{N}$.

$$\mathbf{c}_j^2(t) = \dot{\mathbf{r}}_j^2(t) / \sum_{i=1}^{N} \dot{\mathbf{r}}_j^2(t) \tag{4.23}$$

$$n(t) = \frac{1}{\sum_{j=1}^{N} |\mathbf{c}_j(t)|^4} = N \frac{\left(\frac{1}{N}\sum_{j=1}^{N} |\delta \mathbf{r}_j(t)|^2\right)^2}{\frac{1}{N}\sum_{j=1}^{N} |\delta \mathbf{r}_j(t)|^4} = N \frac{\langle |\delta \mathbf{r}(t)|^2 \rangle^2}{\langle |\delta \mathbf{r}(t)|^4 \rangle} \tag{4.24}$$

$$\frac{n}{N} = \frac{3}{5}\,\frac{1}{1+\alpha_2(t)} \tag{4.25}$$

Equation 4.25 shows that the participation ratio and α_2 carry the same information. Also, Equation 4.25 shows that a perfect Gaussian diffusion with $\alpha_2 = 0$ has participation ratio $\frac{n}{N} \approx 0.6$. Geodesics of normal liquid at equilibrium do have this value [39]. Besides, a motion with few-particle contributions has large positive value of α_2, while a motion involving more than Gaussian numbers of particles has small negative values of α_2 ($-0.4 \leq \alpha_2 < 0$).

By looking at the participation ratio and α_2 along the path, we can investigate how Gaussian the motion of each step is. Fig. 4.16 shows the probability distribution of the participation ratio n/N and non-Gaussian parameter α_2 of each step.

Fig. 4.16 shows that there are few-particle moves along geodesics in hard sphere system. Due to the singularity of the potential energy, the potential energy violation of overlapped particles can be solved locally without disturbing other particles. Those few particle motions are labeled as $n = 2, 3, 4$ in the lower panel of Fig. 4.16. The

weight of this few-particle motion decreases as density increases but is present at all densities.

The locality of interaction among hard spheres also leads to a kind of motion involving a large portion of particles of the system with increasing density, because each local overlapping has to be solved entirely since the rearrangement of other particles will not lower the potential energy. As with increasing density the surrounding particles of overlapped particles have to rearrange in coordination to make enough free space to solve the overlapping. On the contrary, soft particle system can easily "spread the pain" of potential energy violation. As shown in Fig. 4.17, the detailed motion for Kob-Andersen liquid is different from the hard sphere liquid. There are no obvious few-particle motion and there are no obvious very non-Gaussian steps. The difference in potential energy landscape leads to this difference.

Unoptimized paths are used for both systems for computational convenience. The distribution does not vary much after optimization, as shown in Fig. 4.18 and Fig. 4.19.

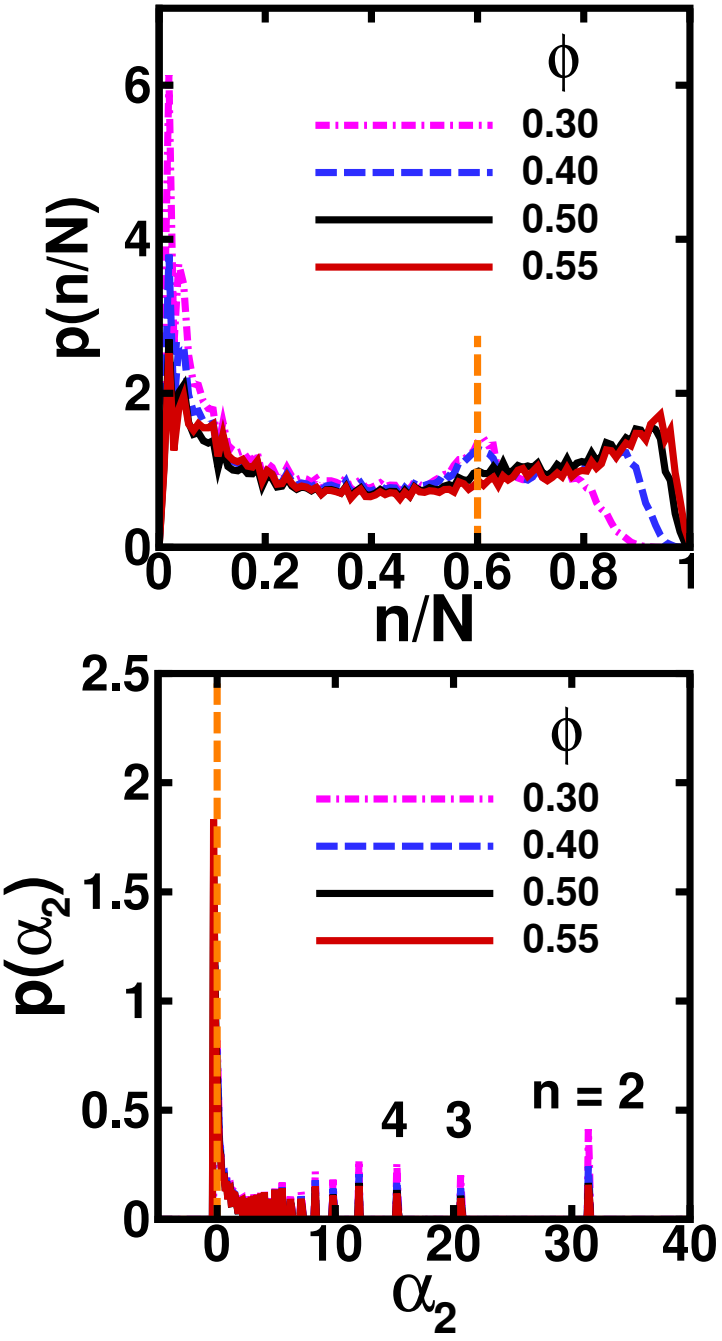

Figure 4.16: Probability distributions of participation ratio n/N (upper panel) and non-Gaussian parameter α_2 (lower panel) of individual steps along the geodesics of the binary hard sphere system at different densities. The vertical dashed line marks the location of perfect Gaussian behavior in both panels. The discrete peaks at large α_2 indicate few-particle moves of $n = 2, 3, 4...$ (Equation 4.25 implies $n = 2, 3, 4, \cdots$ correspond to $\alpha_2 = 31.4, 20.6, 15.2, \cdots$ respectively). The results are averaged over 20 unoptimized paths of $\Delta R = 108\sigma$ and $N = 108$.

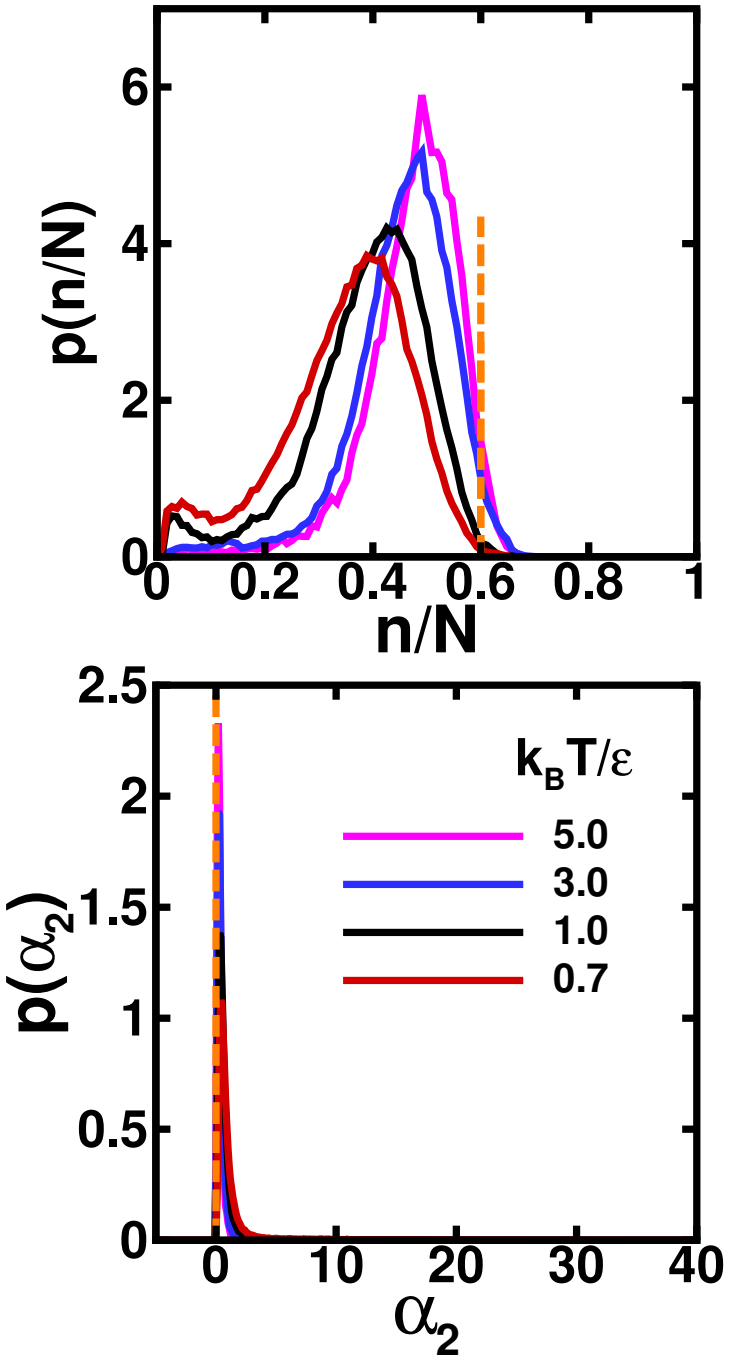

Figure 4.17: Probability distributions of participation ratio n/N (upper panel) and non-Gaussian parameter α_2 (lower panel) of individual steps along the geodesics of the Kob-Andersen system at different temperatures. The vertical dashed line marks the location of perfect Gaussian behavior in both panels. The results are averaged over 20 unoptimized paths of $\Delta R = 108\sigma$ and $N = 108$.

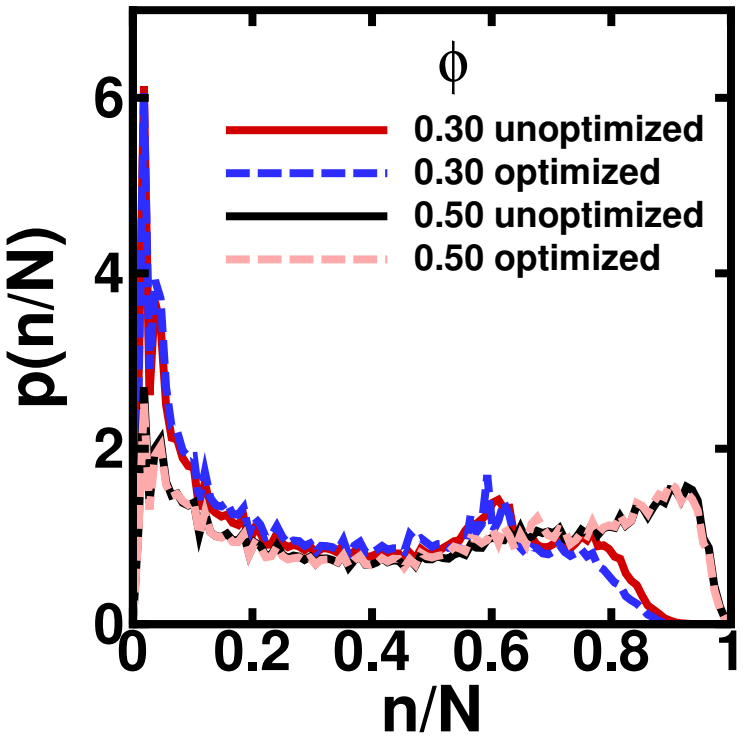

Figure 4.18: Comparison of the probability distributions of single step participation ratio of unoptimized and optimized paths for binary hard sphere system. The optimized results are averaged over 5 optimized paths of $\Delta R = 108\sigma$ and $N = 108$. The unoptimized results are averaged over 20 unoptimized paths of $\Delta R = 108\sigma$ and $N = 108$. The figure shows the distribution does not vary much after optimization.

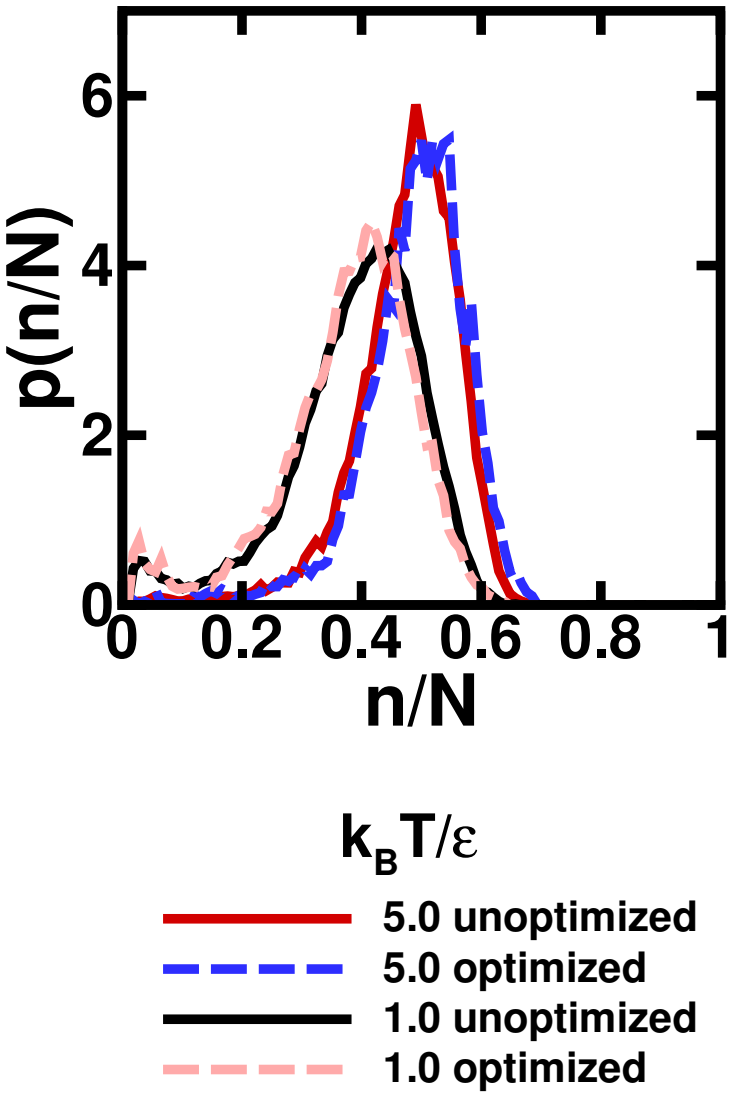

Figure 4.19: Comparison of the probability distributions of single step participation ratio of unoptimized and optimized paths for Kob-Andersen system. The optimized results are averaged over 5 optimized paths of $\Delta R = 108\sigma$ and $N = 108$. The unoptimized results are averaged over 20 unoptimized paths of $\Delta R = 108\sigma$ and $N = 108$. The figure shows the distribution does not vary much after optimization.

4.7 Data Fitting

This section discusses how the data from our calculation for the binary hard sphere system fit into different formulas used to describe glassy behaviors. The data used are the geodesic results of $(\Delta R/g)^2$ and MD results of D_b^* of the binary hard sphere system for density ϕ from 0.53 to 0.57. Although the density range of our data is not close enough to the mode coupling transition, we nevertheless take a look at how the data fits. The three fittings listed below are in analogy with [24], where Szamel et al. fit their data of the same binary hard sphere system at higher densities. For each fitting, we use the same transition density as in [24] to avoid overfitting. Szamel et al. found that their data of relaxation time and length scale is in remarkable agreement with Berthier and Witten's fitting, and VTF fitting of relaxation time is the best over the largest range of densities. We find our data fit mode coupling theory the best from the following figures and goodness of fit.

4.7.1 Mode Coupling Theory

In [24], Szamel et al. fit their data of diffusion coefficient of the same binary hard sphere system for $0.55 \leq \phi \leq 0.58$ with $\phi_c = 0.59$, according to mode coupling theory [24].

$$D^{-1} \propto a(\phi_c - \phi)^{-\gamma}, \quad \phi_c = 0.590 \tag{4.26}$$

where D is the diffusion coefficient of the whole system, calculated from mean square displacement from their Monte Carlo calculation. They found $\gamma = 1.94$.

Here we fit the value of $(\Delta R/g)^2$ by mode coupling theory, as shown in Fig. 4.20.

$$(\Delta R/g)^2 \propto a(\phi_c - \phi)^{\gamma}, \quad \phi_c = 0.590 \tag{4.27}$$

For the fit we find $\gamma = 1.450$.

We also fit the data of D_b^* from molecular dynamic calculation, as shown in

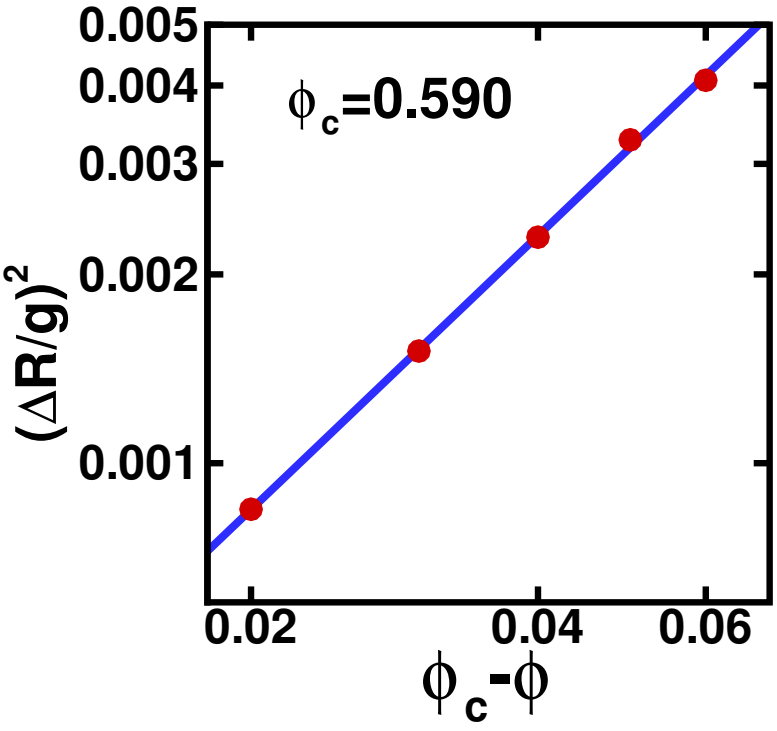

POWER FIT DATA:
Goodness of Fit:
$R^2 = 0.999301$
$R^2 = 0.998602(residual degrees of freedom adjusted)$
$Y = e^(A * log(X) + B)$
A = 1.4503929735522176 3475E+00
B = -1.4040442607470744 4627E+00

Figure 4.20: Mode coupling fitting of $(\frac{\Delta R}{g})^2$ as a function of $\phi_c - \phi$. The red dots are the data points of $(\frac{R}{g})^2$ from 5 paths of $\Delta R = 108\sigma$ and $N = 108$, using optimized paths for $\phi = 0.53, 0.54, 0.55$ and unoptimized paths for $\phi = 0.56, 0.57$. The blue curve is the mode coupling fit. The bottom box is the parameters of the fit.

Fig. 4.21.

$$D_b^* \propto a(\phi_c - \phi)^\gamma, \quad \phi_c = 0.590 \tag{4.28}$$

We find $\gamma = 1.688$ for this fit.

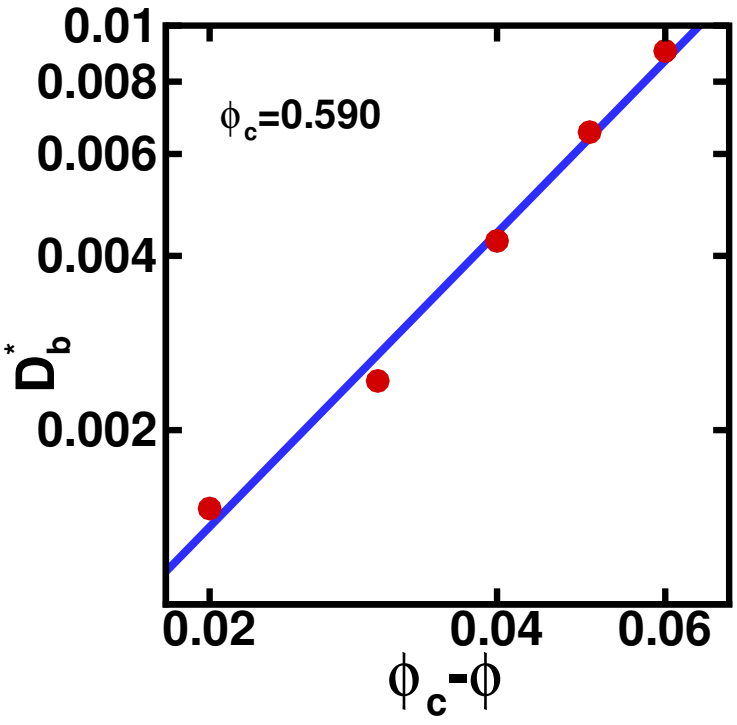

POWER FIT DATA:
Goodness of Fit:
$R^2 = 0.991879$
$R^2 = 0.983757(residualdegreesoffreedomadjusted)$
$Y = e^(A * log(X) + B)$
A = 1.6884476646064519034 2E+00
B = 5.3181513857083473340 0E-03

Figure 4.21: Mode coupling fitting of reduced diffusion coefficient D_b^* as a function of $\phi_c - \phi$. The red dots are the data points of D^* from molecular dynamics calculation. The blue curve is the mode coupling fit. The bottom box is the parameters of the fit.

4.7.2 Vogel-Fucher-Tamman Formula

In [24], Szamel et al. fit their data of relaxation time τ_α for $0.55 \leq \phi \leq 0.5905$ with $\phi_0 = 0.6122$, according to Vogel-Fucher-Tamman formula [24].

$$\ln(\tau_\alpha) \propto A(\phi_0 - \phi)^{-1}, \quad \phi_0 = 0.6122 \tag{4.29}$$

They found $A = 0.222$.

We fit the value of $(\Delta R/g)^2$ by the same formula, as shown in Fig. 4.22.

$$\ln((\Delta R/g)^{-2}) \propto A(\phi_0 - \phi)^{-1}, \quad \phi_0 = 0.6122 \tag{4.30}$$

We find $A = 0.1375$ for this fit.

We also fit the data of D_b^* from molecular dynamic calculation, as shown in Fig. 4.23.

$$\ln(D_b^*) \propto A(\phi_0 - \phi)^{-1}, \quad \phi_0 = 0.6122 \tag{4.31}$$

We find $A = 0.1596$.

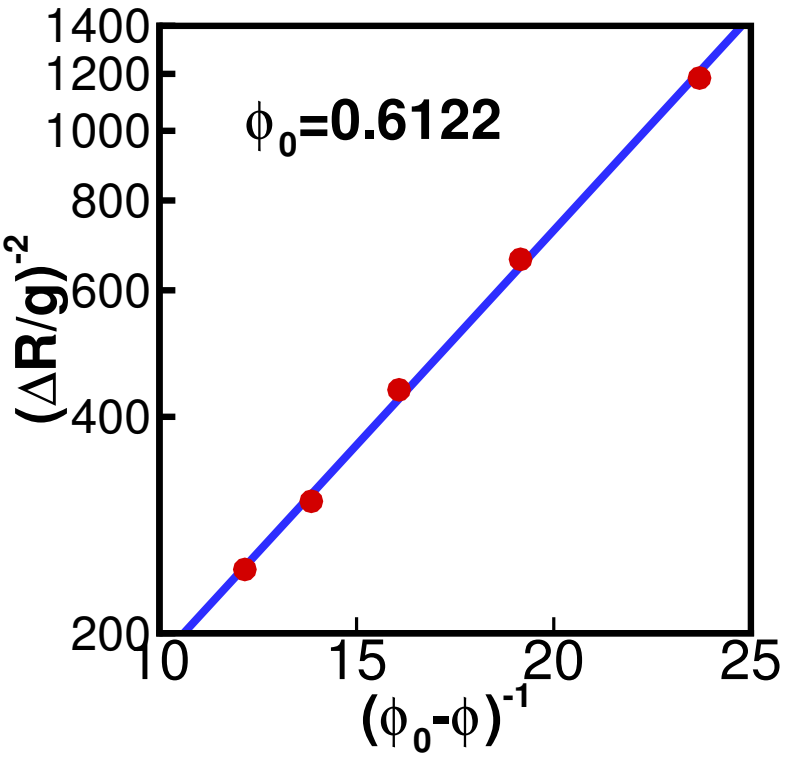

EXPONENTIAL FIT DATA:
Goodness of Fit:
$R^2 = 0.998632$
$R^2 = 0.997265(residual degrees of freedom adjusted)$
$Y = e^(A * X + B)$
A = 1.3752849258544888 5999E-01
B = 3.8383295601606555 1808E+00

Figure 4.22: $(\frac{\Delta R}{g})^2$ as a function of $\phi_0 - \phi$. The red dots are the data points of $(\frac{R}{g})^2$ from 5 paths of $\Delta R = 108\sigma$ and $N = 108$, using optimized paths for $\phi = 0.53, 0.54, 0.55$ and unoptimized paths for $\phi = 0.56, 0.57$. The blue curve is the Vogel-Fucher-Tamman fit. The bottom box is the parameters of the fit.

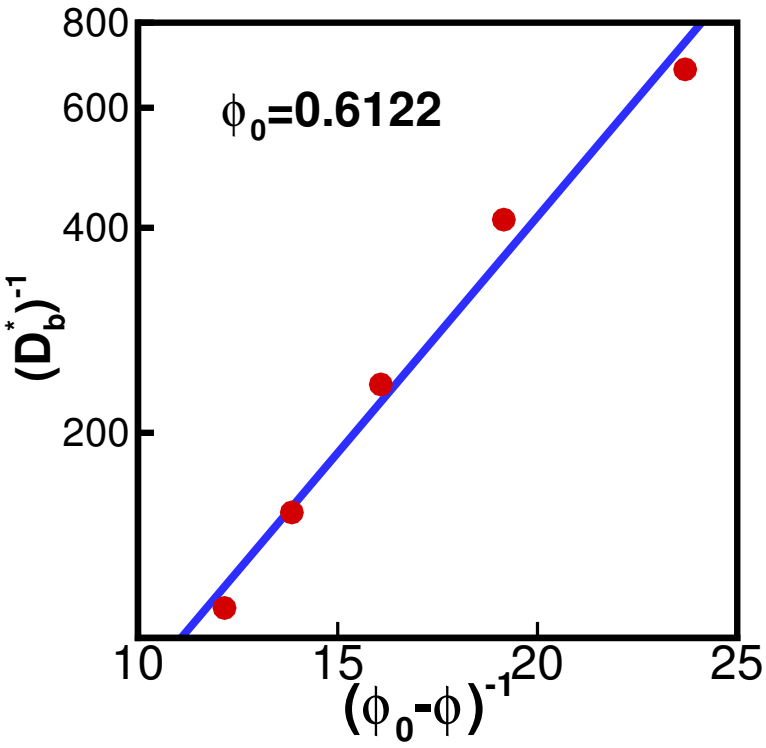

EXPONENTIAL FIT DATA:
Goodness of Fit:
$R^2 = 0.986225$
$R^2 = 0.972451(residualdegreesoffreedomadjusted)$
$Y = e^(A * X + B)$
A = 1.5964295433277478 3532E-01
B = 2.8362946327908744 5926E+00

Figure 4.23: Reduced diffusion coefficient D_b^* as a function of $\phi_0 - \phi$. The red dots are the data points of D^* from molecular dynamics calculation. The blue curve is the Vogel-Fucher-Tamman fit. The bottom box is the parameters of the fit.

4.7.3 Berthier and Witten Formula

In [24], Szamel et al. fit their data of relaxation time $\tau_\alpha$for $0.55 \leq \phi \leq 0.5905$ with $\phi_0 = 0.635$ according to Berthier and Witten formula [24].

$$\ln(\tau_\alpha) \propto A(\phi_0 - \phi)^{-2}, \quad \phi_0 = 0.635 \tag{4.32}$$

They found $A = 0.017$.

We fit the value of $(\Delta R/g)^2$ by the same formula, as shown in Fig. 4.24.

$$\ln((\Delta R/g)^{-2}) \propto A(\phi_0 - \phi)^{-2}, \quad \phi_0 = 0.635 \tag{4.33}$$

We find $A = 0.01083$ for this fit.

We also fit the data of D_b^* from molecular dynamic calculation, as shown in Fig. 4.25.

$$\ln(D_b^*) \propto A(\phi_0 - \phi)^{-2}, \quad \phi_0 = 0.635 \tag{4.34}$$

We find $A = 0.01256$ for this fit.

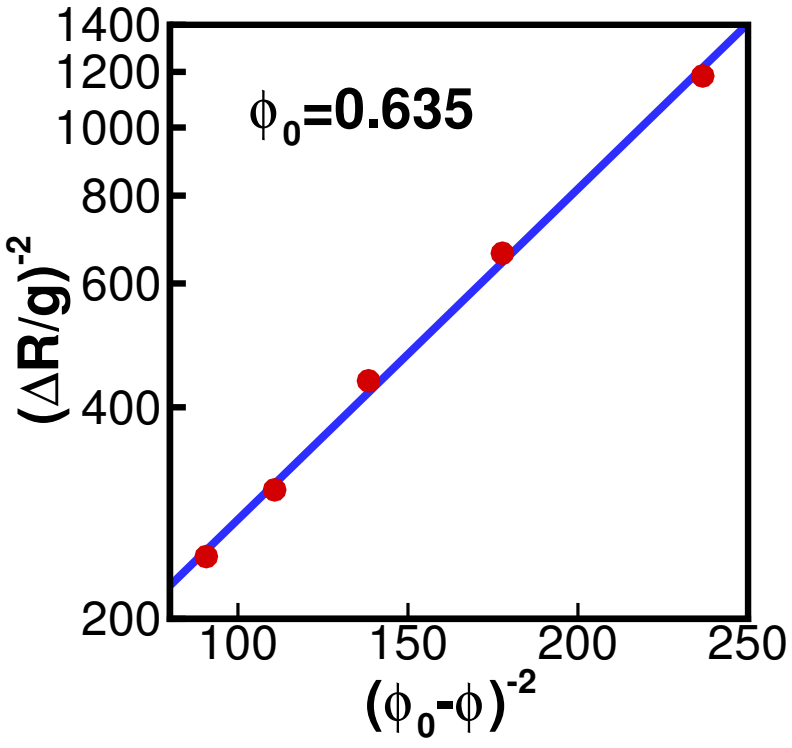

EXPONENTIAL FIT DATA:
Goodness of Fit:
$R^2 = 0.997713$
$R^2 = 0.995426(residual degrees of freedom adjusted)$
$Y = e^(A * X + B)$
A = 1.0832232463664492883OE-02
B = 4.5405296227144003040 6E+00

Figure 4.24: $(\frac{\Delta R}{g})^2$ as a function of $\phi_0 - \phi$. The red dots are the data points of $(\frac{R}{g})^2$ from 5 paths of $\Delta R = 108\sigma$ and $N = 108$, using optimized paths for $\phi = 0.53, 0.54, 0.55$ and unoptimized paths for $\phi = 0.56, 0.57$. The blue curve is the Berthier and Witten fit. The bottom box is the parameters of the fit.

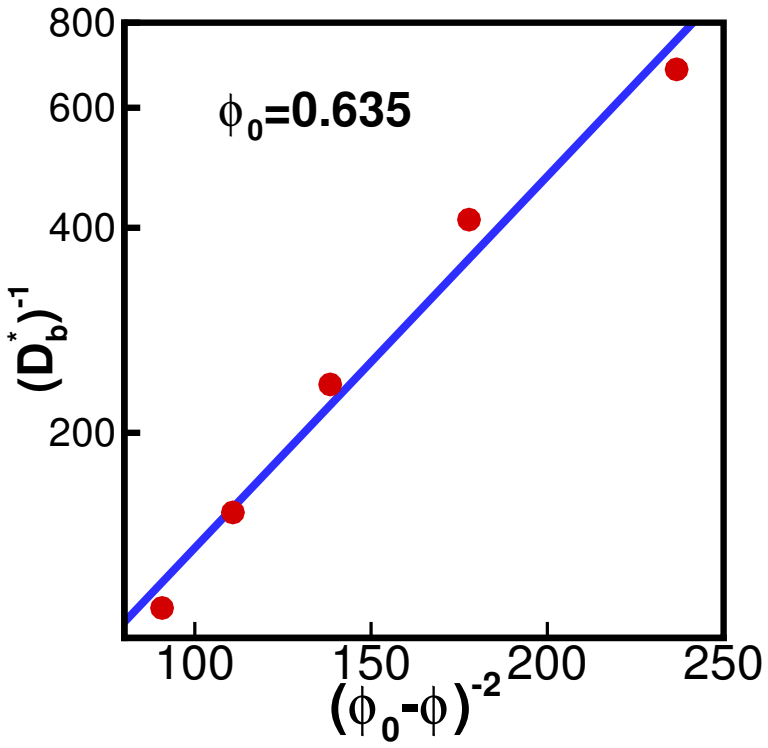

EXPONENTIAL FIT DATA:
Goodness of Fit:
$R^2 = 0.983282$
$R^2 = 0.966565(residualdegreesoffreedomadjusted)$
$Y = e^(A * X + B)$
A = 1.25595041101043327497E-02
B = 3.6536018724057557349 7E+00

Figure 4.25: Reduced diffusion coefficient D_b^* as a function of $\phi_0 - \phi$. The red dots are the data points of D^* from molecular dynamics calculation. The blue curve is the Berthier and Witten fit. The bottom box is the parameters of the fit.

4.8 Limitations of Generating Geodesics at High Density

The results of binary hard sphere system goes to density $\phi = 0.57$. At high density close to the mode coupling transition, finding pairs of end points that are far away enough from each other is the major hindrance of getting geodesic results.

The trend is that when ϕ is high, the computational time needed to get end points by regular MD grows rapidly. Table 4.1 shows the time needed for regular molecular dynamics to find one pair of end points distanced by $\Delta R = 108\sigma$ for the binary hard sphere system of $N = 108$. The result is recorded in the rough order of thousands. Within the given computational time, the regular molecular dynamics has not been able to find a pair of such end points for density $\phi = 0.598$ and higher.

The difficulty of finding end points that are enough far away does not exist only in glass-forming hard sphere systems. In [32] and [33], Wang et al. found similar behavior of the glass-forming Kob-Andersen liquid, that beyond a certain critical temperature (the empirical mode-coupling temperature), they have not found a pair of end points that are far away by a required distance.

A possible explanation is that the configuration space is divided up to different separate regions beyond a certain critical value of ϕ (or beyond a critical temperature in the case of soft particle liquid), similar to the "ocean -lake" analogy in [32]. Upon increasing ϕ (or decreasing temperature in the case of soft particle liquid), the available paths between two well separated configurations becomes more convoluted.

ϕ	time (seconds)
0.50	700
0.58	80,000
0.59	520,000
0.597	3,500,000

Table 4.1: Time needed to generate one pair of end points of $\Delta R = 108\sigma$ by regular MD, for the binary hard sphere system of $N = 108$.

The regular molecular dynamics method has more difficulty propagating the system to a distant configuration. At certain critical point, there may be a sharp transition that the configuration space changes to a disconnected state. The system is confined in one of the disconnected regions and is non-ergodic [32]. This percolation transition of the potential energy landscape causes the regular molecular dynamics to fail to propagate the system to a configuration far away.

4.9 Statistics along the Path

To take a more detailed look at the paths, this section shows some statistics of the steps along the paths of the binary hard sphere system.

4.9.1 Fractions of Direct Steps and Collision Avoidance Steps

To see the fractions of different kinds of steps along the paths, we compare the number of direct steps and the number of collision avoidance steps along the paths, shown in Table 4.2. The results are averaged over 5 unoptimized paths of $N = 108$ and $\Delta R = 108\sigma$ and are recorded in the rough order of thousands of steps.

Table 4.2 shows that the major portion of the path is the collision avoidance step, which is the segments of paths that are going around the boundaries. This is the same as soft particle liquid, in which case the major portion of a path is from escape steps that are going around boundaries too. It is consistent with the fact that in the high dimensional configuration space, most configurations lie close to the boundaries

ϕ	number of direct steps	number of collision avoidance steps	fraction of collision avoidance steps
0.30	18,000	300,000	94%
0.50	43,000	1,000,000	96%
0.58	150,000	6,000,000	98%

Table 4.2: Number of different steps along a path, for the binary hard sphere system of $N = 108$ and $\Delta R = 108\sigma$.

in the potential energy landscape ensemble.

Besides, Table 4.2 also shows that the fraction of collision avoidance step increases upon increasing ϕ. With increasing density, the forbidden regions occupy bigger fraction of the configuration space. There is less chance of successful direct steps due to the decrease of free space. The increasing fraction of collision avoidance steps means that the portion of the segments of geodesics that are going around the obstacles increases.

4.9.2 Overlaps in Failed Direct Steps

In a failed direct step, a particle with overlaps can have from 1 to $N-1$ overlapping partners. Denote the number of the overlapping partners that one overlapped particle has as v ($v = 1, 2, \cdots, N-1$). Figure 4.26 shows the distribution of v. v is clearly a local property that is independent of N, which is sensible because of the locality of hard sphere potential. Also, when packing fraction ϕ gets higher, an overlapped particle has a higher probability of having more overlapping partners. It is reflected in the distribution of v that v has a higher weight at relatively large values when ϕ is higher.

To show that v is independent of N, we compare the distributions of v of $N = 108$ and $N = 256$ in the same graph, shown in Fig. 4.27.

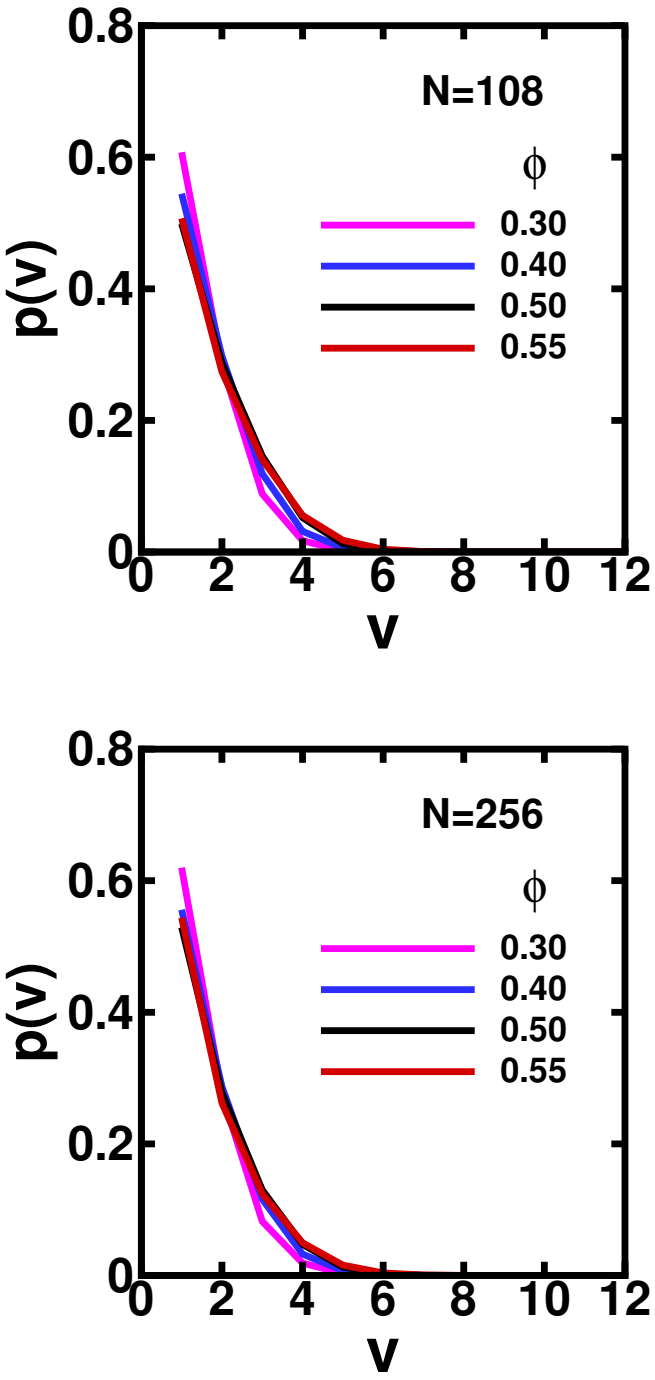

Figure 4.26: Probability distributions of the number of overlapping partners one overlapped particle has. The upper panel is the result of the binary hard sphere system of size $N = 108$ and lower panel is of $N = 256$. Each distribution is from all failed direct steps of 1 unoptimized path of $\Delta R/\sigma = 10\sqrt{N}$. Particles that do not have overlap in a failed direct step are not taken into account in the distribution.

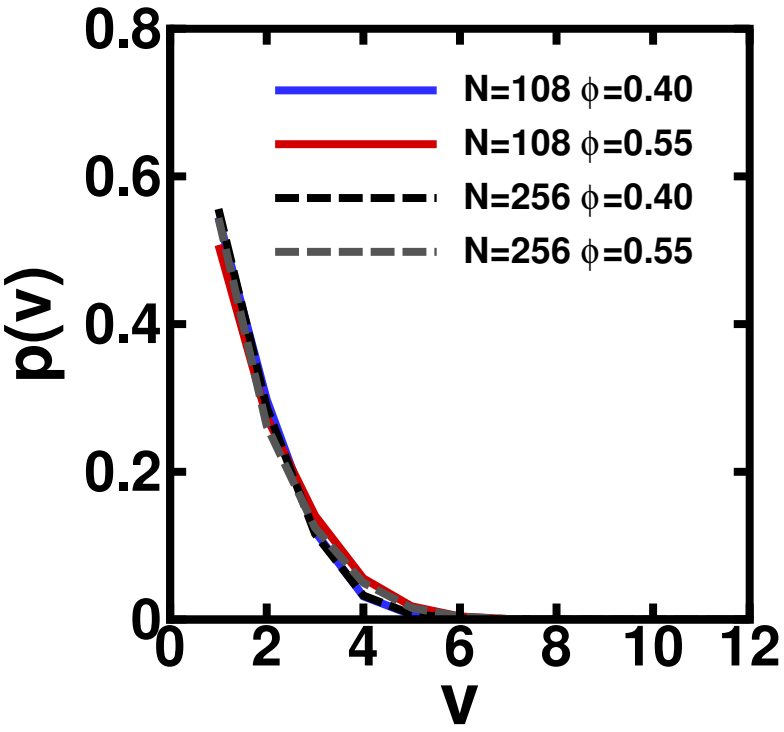

Figure 4.27: Comparison of probability distributions of the number of overlapping partners one overlapped particle has. The data is the same as in Fig. 4.26. This figure shows that v is independent of N.

4.9.3 Number of Particles in a Collision Avoidance Step

In a collision avoidance step, particles that are spatially close to overlapped particles have to rearrange in coordination to solve the overlap and reposition the system in configuration space, especially when density is high. Denote the number of particles that actually moved in a collision avoidance step as c ($c = 2, 3, \cdots, N$). $\frac{c}{N}$ is the fraction of particles involved in a collision avoidance step in the system. Fig. 4.28 shows the distribution of $\frac{c}{N}$. Similar to the participation ratio, the distribution of $\frac{c}{N}$ demonstrates that the collision avoidance step can have few particle moves as well as large proportion of particle moves. The weight of large proportion of particle moves increases with increasing density, which is due to the locality of hard sphere potential as discussed in Section 4.5.

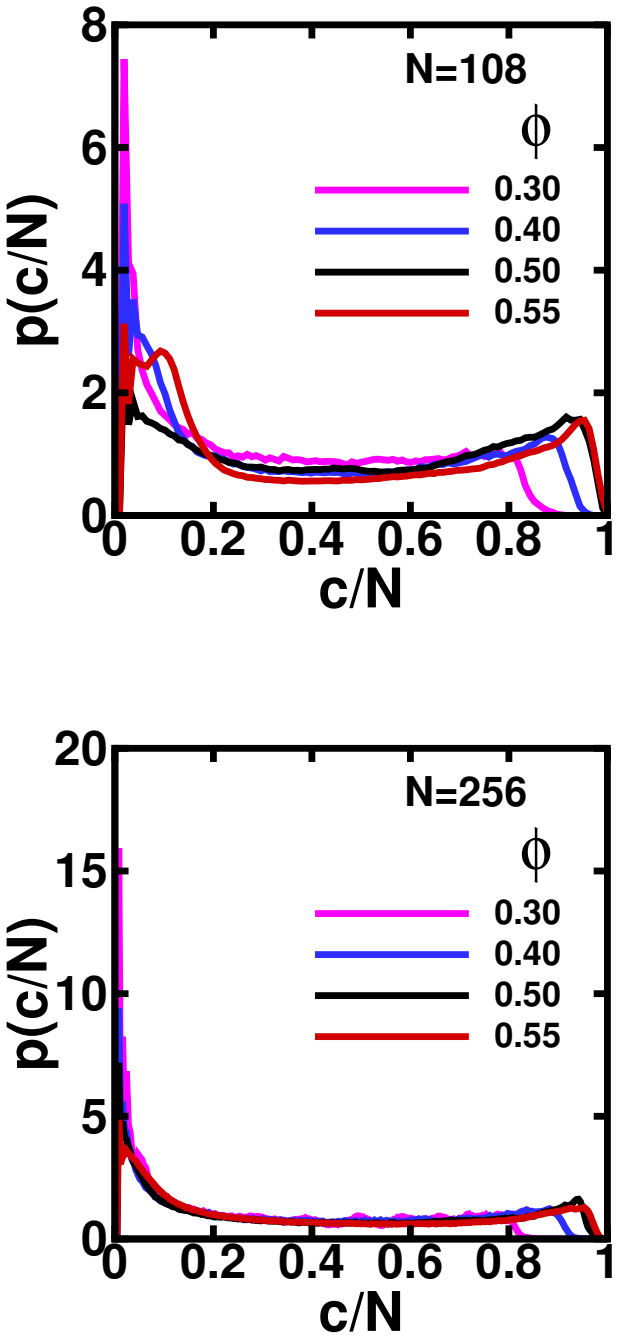

Figure 4.28: Probability distributions of the fraction of particles moved in a collision avoidance step. The upper panel is the result of the binary hard sphere system of size $N = 108$ and lower panel is of $N = 256$. Each distribution is from all collision avoidance steps of 1 unoptimized path of $\Delta R/\sigma = 10\sqrt{N}$.

To compare $\frac{c}{N}$ for different N, we compare the distribution of v for $N = 108$ and $N = 256$ in the same graph, shown in Fig. 4.29. It shows $\frac{c}{N}$ is independent of N, same as the participation ratio.

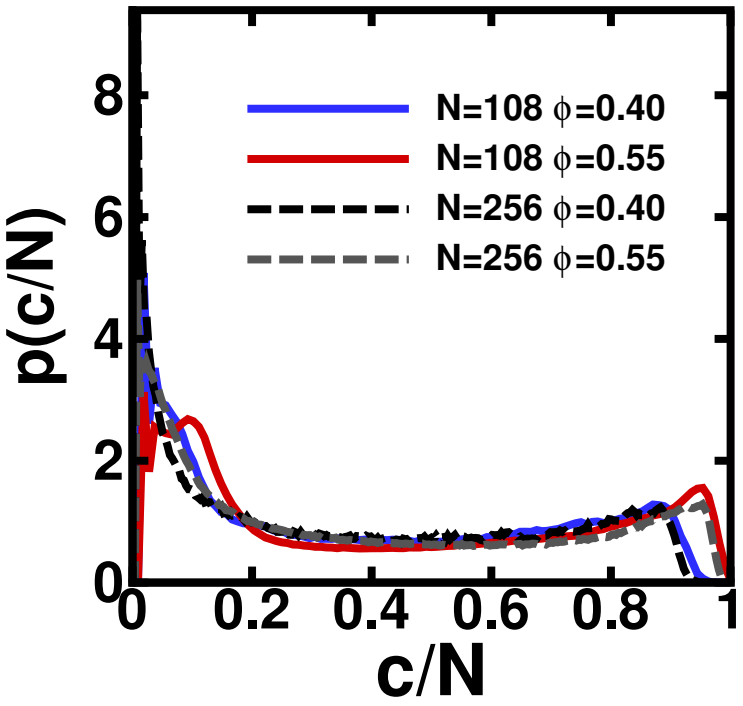

Figure 4.29: Comparison of probability distributions of the fraction of particles moved in a collision avoidance step for $N = 108$ and $N = 256$. The data is the same as in Fig. 4.28. This figure shows that $\frac{c}{N}$ is independent of N.

4.9.4 Groups of Particles in a Collision Avoidance Step

The particles that actually moved in a collision avoidance step can be divided into different groups according to the cause of the move, traced back to the initial overlapped particles after the failed direct step.

For example, if after one failed direct step, particle 1 and 2 overlap after the failed move, moving them apart involving moving particle 3. And particle 101, 102, 103 overlap after the failed move, moving them apart involving moving particle 104. Then

particle 1, 2, 3 are in one group, particle 101, 102, 103, 104 are in another group.

If the collision avoidance move invoked by two different groups involves the same particle, then the two groups joins to be one big group. In the above example, if moving apart particle 1 and 2 causes moving particle 3 and 50, and moving apart particle 101, 102, 103 causes moving particle 104 and 50, then particle 1, 2, 3, 50, 101, 102, 103, 104 are counted as one group.

4.9.4.1 Number of Particles in a Group in a Collision Avoidance Step

Denote the number of particles in one group in a collision avoidance step as s. According to the above definition, a group has at least 2 particles in it. Fig. 4.30 shows the distribution of s. The motion of each group is localized and the number of particles in a group is independent of N because of the locality of the hard sphere potential. s also has a very weak ϕ dependence.

To show that s is independent of N, we compare the distribution of s for $N = 108$ and $N = 256$ in the same graph, shown in Fig. 4.31.

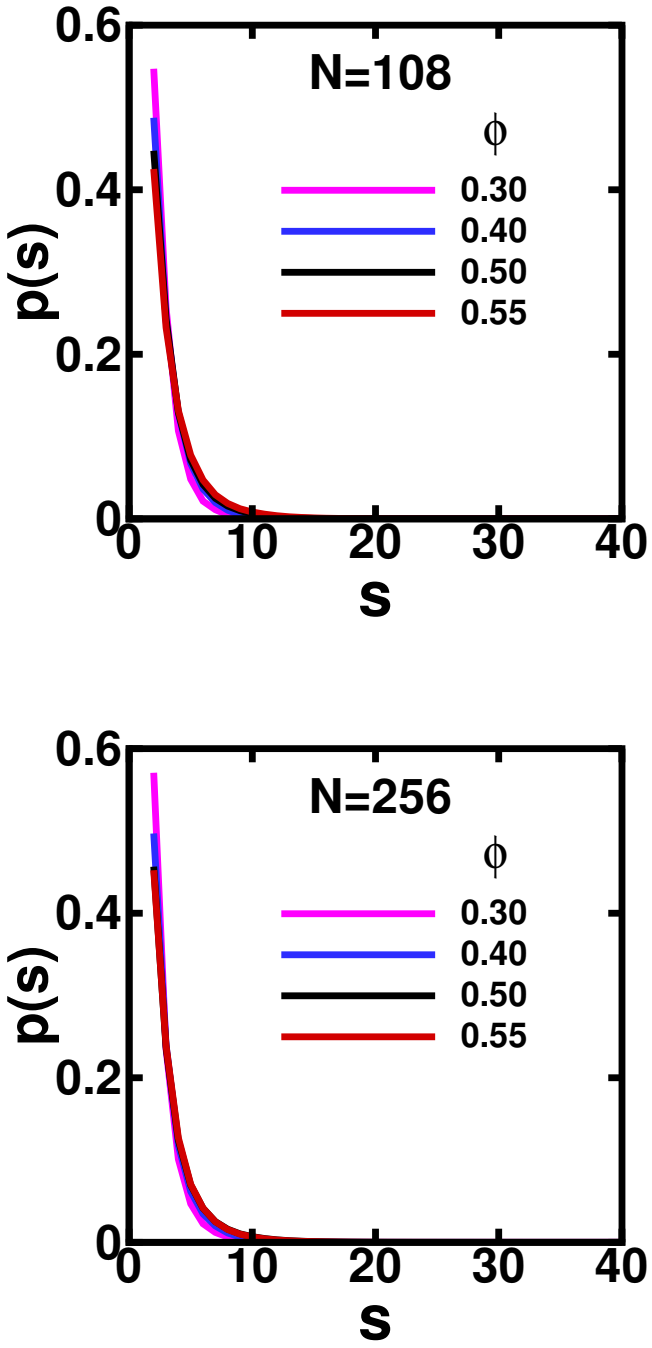

Figure 4.30: Probability distributions of the number of particles per group in a collision avoidance step. The upper panel is the result of the binary hard sphere system of size $N = 108$ and lower panel is of $N = 256$. Each distribution is from all collision avoidance steps of 1 unoptimized path of $\Delta R/\sigma = 10\sqrt{N}$.

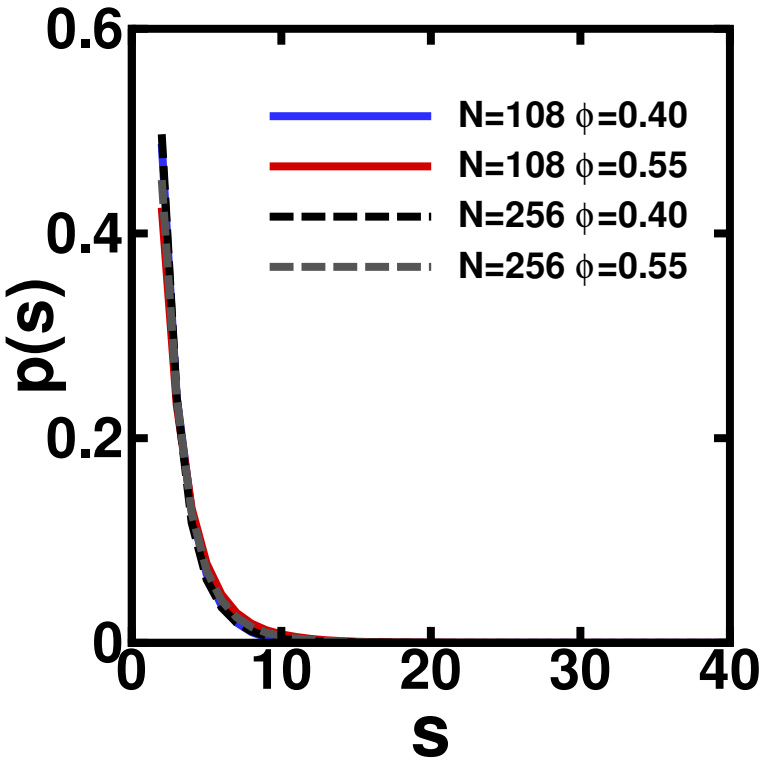

Figure 4.31: Comparison of probability distributions of the number of particles per group for $N = 108$ and $N = 256$. The data is the same as in Fig. 4.30. This figure shows that s is independent of N.

4.9.4.2 Number of Groups in a Collision Avoidance Step

Denote the number of groups in a collision avoidance step as m. Fig. 4.32 shows the distribution of $\frac{m}{N}$.

m should behave macroscopically because of the singularity of the hard sphere potential. To show that $m \propto N$, we compare the distributions of $\frac{m}{N}$ for $N = 108$ and $N = 256$ in the same graph, shown in Fig. 4.33.

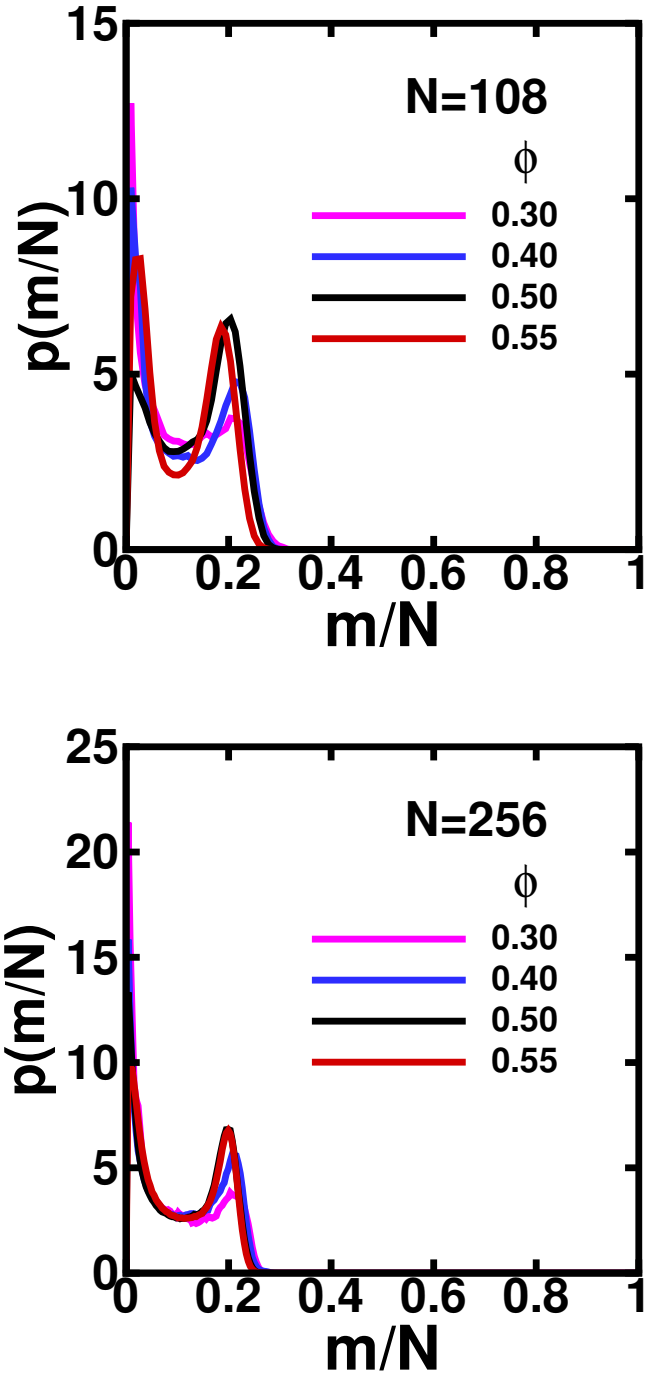

Figure 4.32: Probability distributions of the number of groups per collision avoidance step. The upper panel is the result of the binary hard sphere system of size $N = 108$ and lower panel is of $N = 256$. Each distribution is from all collision avoidance steps of 1 unoptimized path of $\Delta R/\sigma = 10\sqrt{N}$.

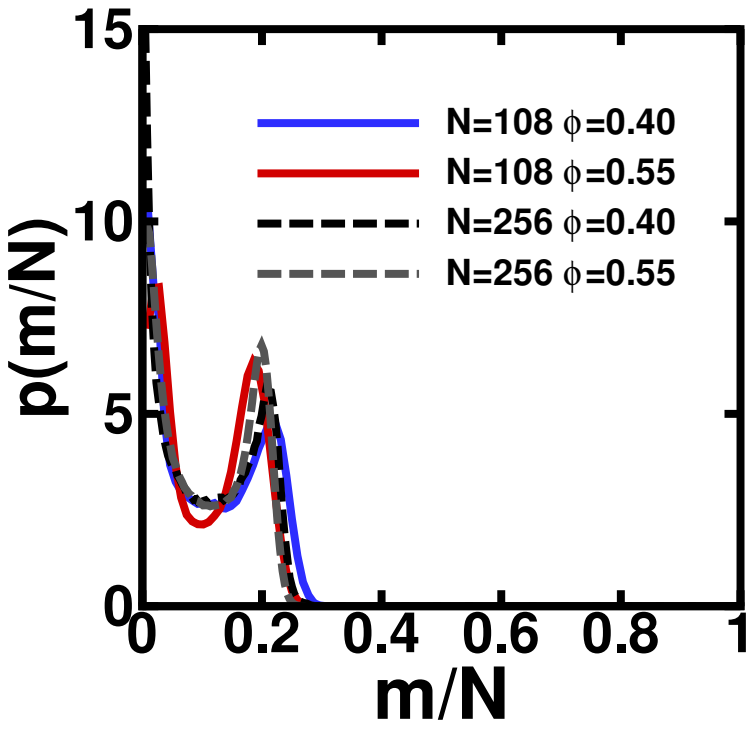

Figure 4.33: Comparison of probability distributions of the number of groups per collision avoidance step for $N = 108$ and $N = 256$. The data is the same as in Fig. 4.32. This figure shows that $\frac{m}{N}$ is independent of N, that $m \propto N$.

4.9.4.3 Conditional Distribution of Number of Particles per Group

To further see whether there exists a correlation between the number of particles per group and the number of groups per step, another distribution of particles per group is calculated, based on the number of groups in the collision avoidance step.

Three distributions are calculated from the data of collision avoidance steps.

- Distribution of number of particles per group when the number of group is less than a lower bound. This part is considered as intensive. The probability density function is denoted as $p(s_l)$.

- Distribution of number of particles per group when the number of group is bigger than an upper bound. This part is considered as extensive. The probability density function is denoted as $p(s_r)$.

- Distribution of number of particles per group when the number of group is between the lower bound and the upper bound. This part is a mix of intensive and extensive group motion. The probability density function is denoted as $p(s_m)$.

For $N = 108$, the lower bound is chosen to be 4 and the upper bound is 18. For $N = 256$, the lower bound is chosen to be 10 and the upper bound is 45.

Fig. 4.34 shows these three distributions of the binary hard sphere system at density $\phi = 0.50$. The distributions of the system at other densities is similar. There is no distinct differences in these distributions. It means there are not distinctive kinds of motions in collision avoidance steps.

We also compare the two graphs in Fig. 4.34, shown in Fig. 4.35.

Through this section, we show that the collision avoidance step takes up the major fraction of a path, especially when density is high. Also, due to the singularity of the hard sphere potential, both the number of overlapping partners that an overlapped particle has and the number of particles that are involved in a collision avoidance step are independent of N, and the collision avoidance step has both few particle moves and large proportion of particle moves. The hard sphere potential affects the detailed properties of the paths.

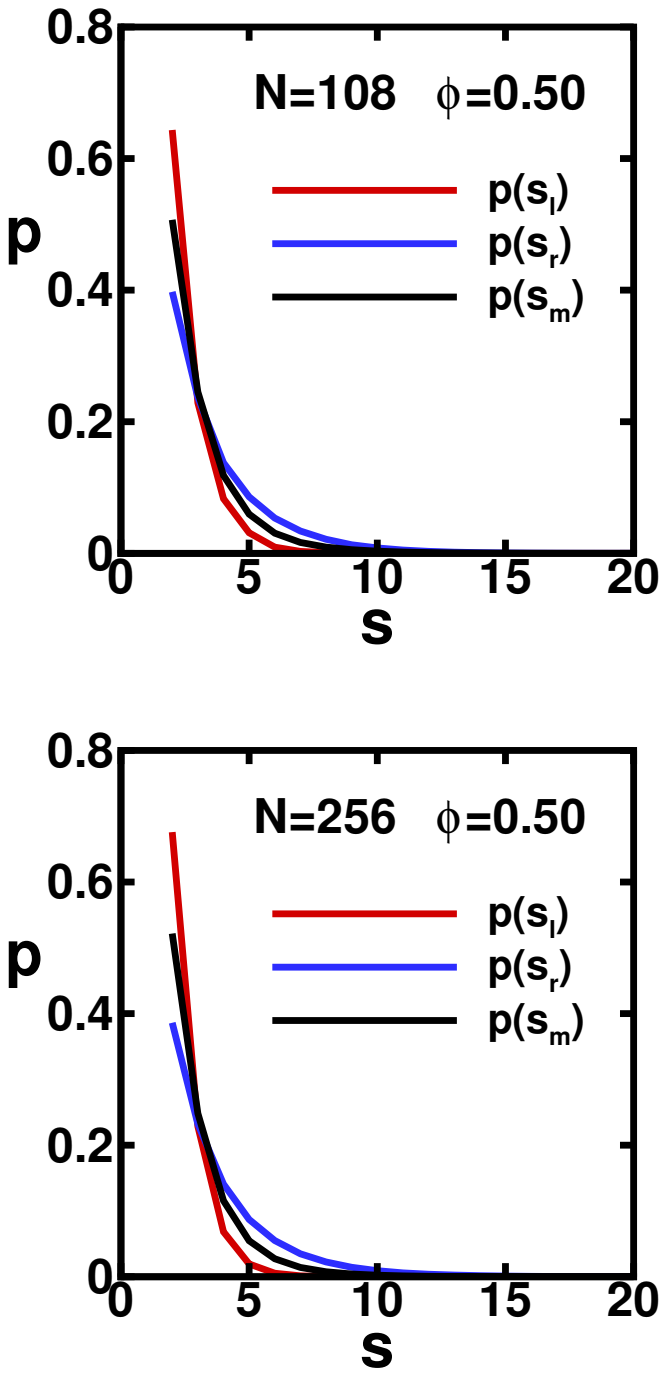

Figure 4.34: Conditional distributions of the number of particles per group in a collision avoidance step. The upper panel is the result of the binary hard sphere system of size $N = 108$ and lower panel is of $N = 256$. Each distribution is from all collision avoidance steps of 1 unoptimized path of $\Delta R/\sigma = 10\sqrt{N}$.

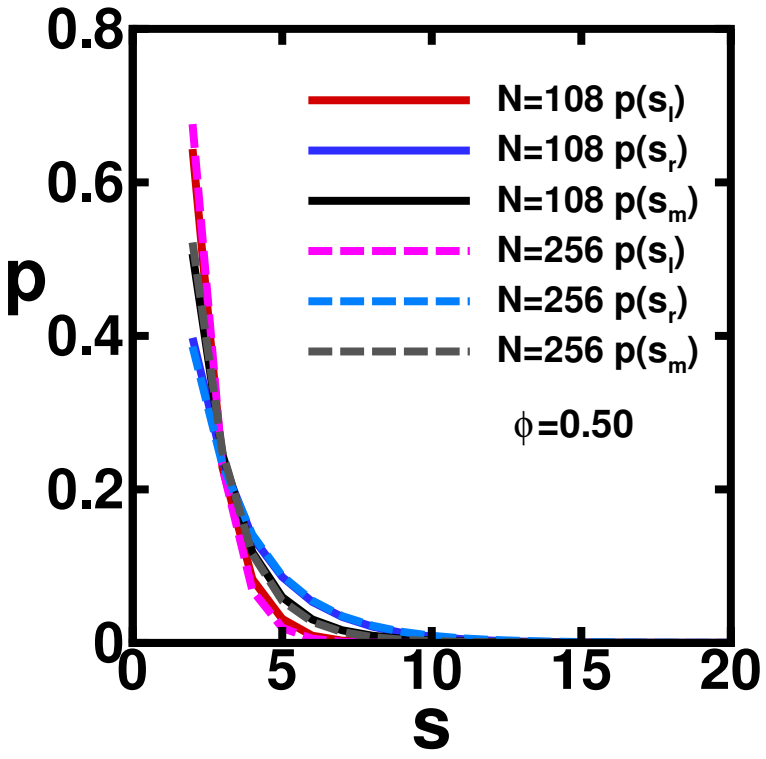

Figure 4.35: Comparison of conditional distributions of the number of particles per group in a collision avoidance step for $N = 108$ and $N = 256$. The data is the same as in Fig. 4.34. This figure shows that the conditional distributions are independent of N .

4.10 Parameter Test

This section shows numerical tests used to pick optimum parameters. The optimum parameters are the ones shown in Chapter 3 and are used for generating main results.

4.10.1 Direct Step Length δ_{di}

$\delta_{di} = 0.01\sigma$ is used as the length of the direct step of the whole system. Fig. 4.36 shows the test result of different values of δ_{di}, while fixing the values of all other parameters as shown in Chapter 3.

Fig. 4.36 shows that $\delta_{di} = 0.01\sigma$ and $\delta_{di} = 0.1\sigma$ are able to generate shorter paths than $\delta_{di} = 0.001\sigma$. $\delta_{di} = 0.01\sigma$ and $\delta_{di} = 0.1\sigma$ also take similar amount of computa-

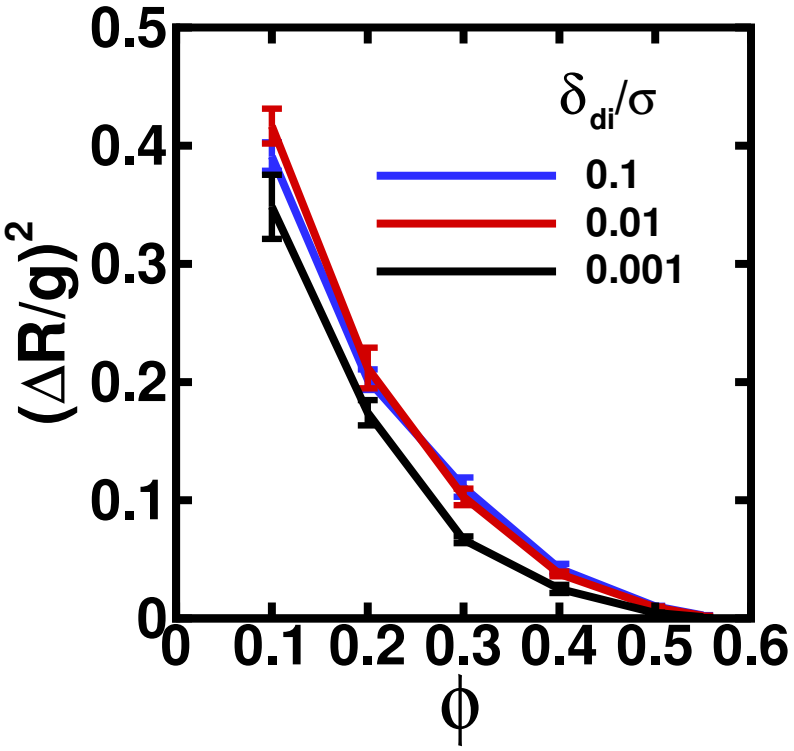

Figure 4.36: Test of different values of δ_{di} for the binary hard sphere system. The density ϕ goes from 0.05 to 0.55. The results are averaged over 5 unoptimized paths of $\Delta R = 108\sigma$ and $N = 108$.

tional time to find a path. To avoid that too big a step may jump over a forbidden region, we choose $\delta_{di} = 0.01\sigma$ to ensure the continuous and smoothness of the path.

4.10.2 Collision Avoidance Step Length δ_{ca}

$\delta_{ca} = 0.0001\sigma$ is used as the length of the collision avoidance step of each particle. Fig. 4.37 shows the test result of different values of δ_{ca}, while fixing the values of all other parameters as shown in Chapter 3.

Fig. 4.37 shows that $\delta_{ca} = 10^{-4}\sigma$ and $\delta_{ca} = 10^{-5}\sigma$ are able to generate shorter paths than $\delta_{ca} = 10^{-3}\sigma$. But $\delta_{ca} = 10^{-5}\sigma$ takes longer computational time to find a path than $\delta_{ca} = 10^{-4}\sigma$, so we choose $\delta_{ca} = 10^{-4}\sigma$.

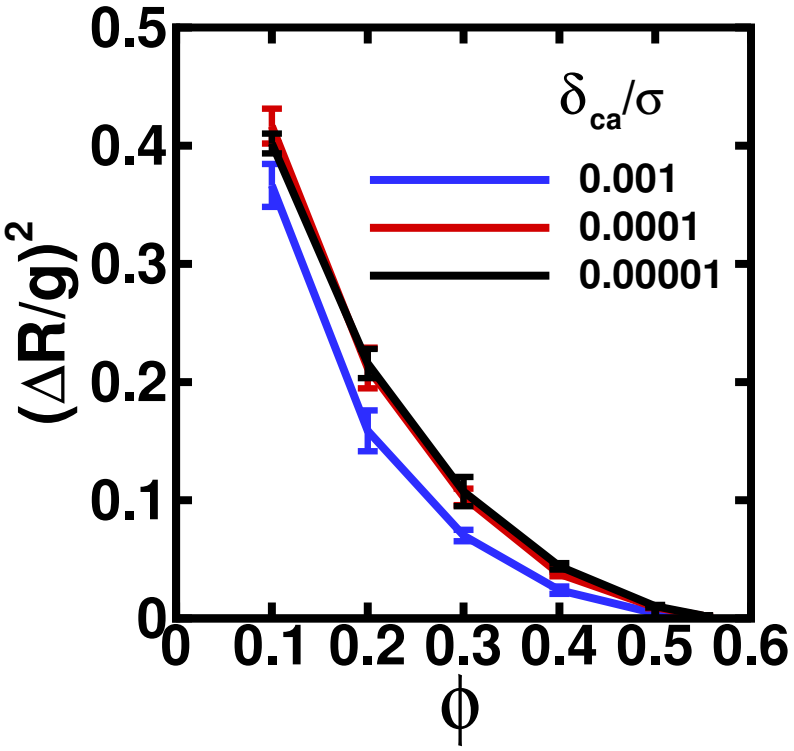

Figure 4.37: Test of different values of δ_{ca} for the binary hard sphere system. The density ϕ goes from 0.05 to 0.55. The results are averaged over 5 unoptimized paths of $\Delta R = 108\sigma$ and $N = 108$.

4.10.3 Fictitious Potential

Recall the fictitious potential used for generating geodesics for hard sphere systems is

$$\mu_{ij} = \begin{cases} 0 & : r_{ij} \geq \sigma_{ij} \\ \nu(r_{ij}/\sigma_{ij}) & : r_{ij} < \sigma_{ij} \end{cases} \tag{4.35}$$

$$\nu(x) > 0 \quad if\ 0 < x < 1 \tag{4.36}$$

$$\nu_{ij}(x) = \sigma_{ij}^2(1-x) \tag{4.37}$$

Trials with an alternate potential

$$\nu_{ij}^{a}(x) = \sigma_{ij}^{3}(\frac{1}{3}x^3 - \frac{1}{2}x^2 + \frac{1}{6}) \tag{4.38}$$

show no discernible numerical differences, as shown in Fig. 4.38.

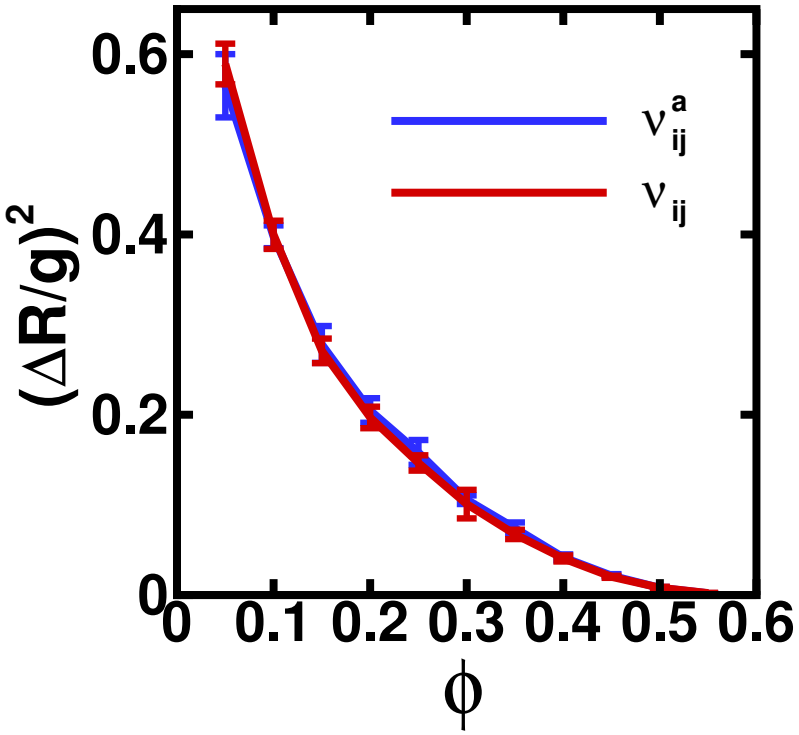

Figure 4.38: Test of different fictitious potentials for the binary hard sphere system. The density ϕ goes from 0.05 to 0.55. The results are averaged over 5 unoptimized paths of $\Delta R = 108\sigma$ and $N = 108$. The figure shows that there is no distinct numerical differences.

The fictitious potential and the resulting fictitious force is just a tool to let the system "detect" the forbidden regions around it in configuration space, thus the detailed form of the potential energy function should not matter for finding geodesics.

4.11 MD Calculation of Diffusion Coefficients of Hard Sphere Liquids

This section gives numerical tests to pick optimum parameters used in molecular dynamics calculation of diffusion coefficients of the hard sphere liquids, as well as the comparison of the calculation results with published data.

4.11.1 Mono-disperse Hard Sphere Liquid

The parameters used for calculating the diffusion coefficient of the mono disperse hard sphere system is Table 4.3. The result is shown in Fig. 4.39.

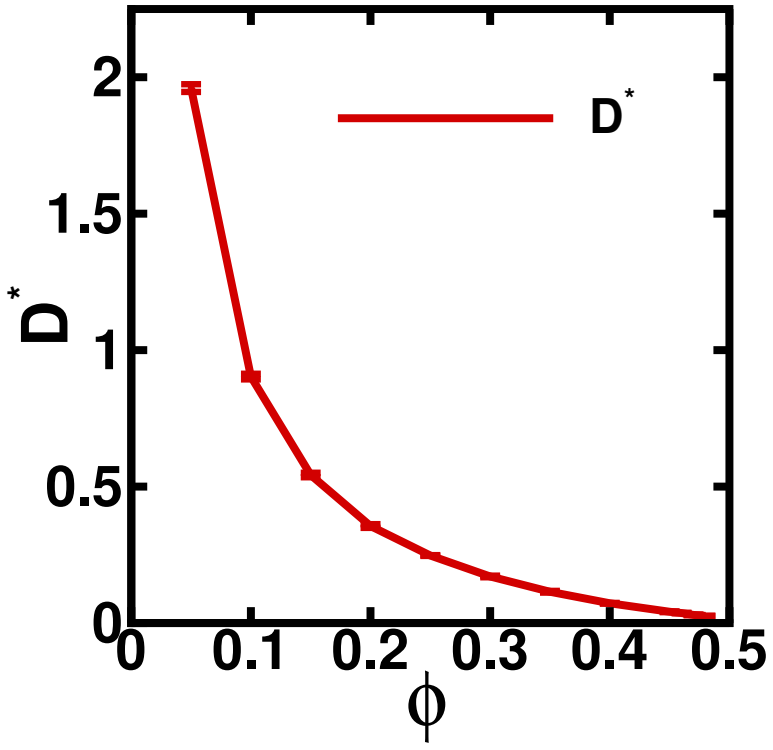

Figure 4.39: Reduced diffusion coefficient D^* as a function of ϕ for the mono disperse hard sphere system.

To test whether the value of t_{max} is large enough to get converged result, we run the same MD calculation with two different sets of parameters as shown in Table 4.4.

ϕ	Δt	n	t_{max}
0.05	0.0010	30000	30
0.10,0.15	0.00050	30000	15
0.20,0.25	0.00020	30000	6
0.30,0.35	0.00010	30000	3
0.40,0.45	0.000050	30000	1.5
0.46-0.48	0.00030	30000	0.9

ϕ : packing fraction
Δt : time between two consecutively sampled configurations
n : number of intervals in Simpson's rule
t_{max} : upper limit of time for calculating velocity correlation

Table 4.3: Parameters for calculation of the diffusion coefficient of the mono disperse hard sphere system

The upper panel in Table 4.4 has a shorter t_{max} than the lower panel for each density while fixing Δt the same. By comparing the results with the two different sets of parameters, we show that the value of t_{max} is large enough to generate converged result, as shown in Fig. 4.40.

The final results of diffusion coefficients is calculated with an even larger t_{max} and smaller Δt, as shown in Table 4.3. A comparison of the final results with the testing results show that the value of Δt is small enough to have converged results, as shown in Fig. 4.41.

ϕ	Δt	n	t_{max}
0.05	0.00150	10000	15
0.10,0.15	0.00080	10000	8
0.20,0.25	0.00050	10000	5
0.30,0.35	0.00020	10000	2
0.40,0.45	0.00010	10000	1
0.46-0.48	0.00060	10000	0.6
ϕ	Δt	n	t_{max}
0.05	0.00150	12000	18
0.10,0.15	0.00080	12000	9.6
0.20,0.25	0.00050	12000	6
0.30,0.35	0.00020	12000	2.4
0.40,0.45	0.00010	12000	1.2
0.46-0.48	0.00060	12000	0.72

ϕ : packing fraction
Δt : time between two consecutively sampled configurations
n : number of intervals in Simpson's rule
t_{max} : upper limit of time for calculating velocity correlation

Table 4.4: Parameters for testing t_{max} for the mono disperse hard sphere system

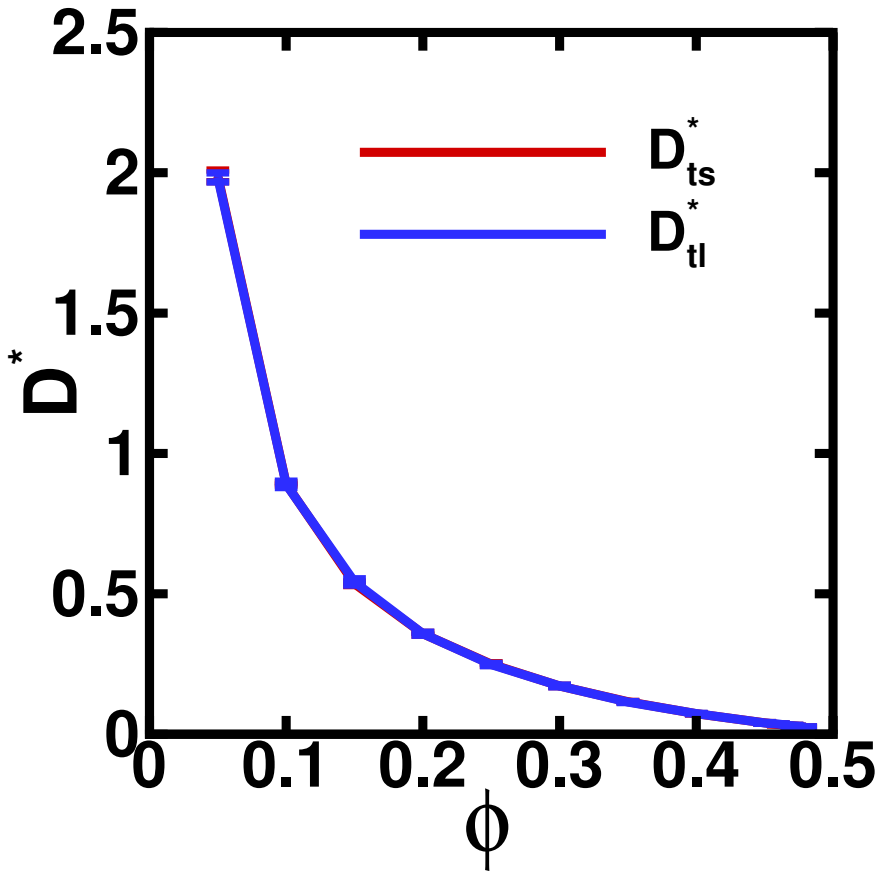

Figure 4.40: Convergence of the results of D^* with different t_{max}. The red curve is the diffusion constants D^*_{ts} calculated with a smaller value of t_{max} as shown in the upper panel of Table 4.4. The blue curve is the diffusion constants D^*_{tl} calculated with a larger value of t_{max} as shown in the lower panel of Table 4.4. This figure shows that the value of D^* is converged with respect to the chosen t_{max}.

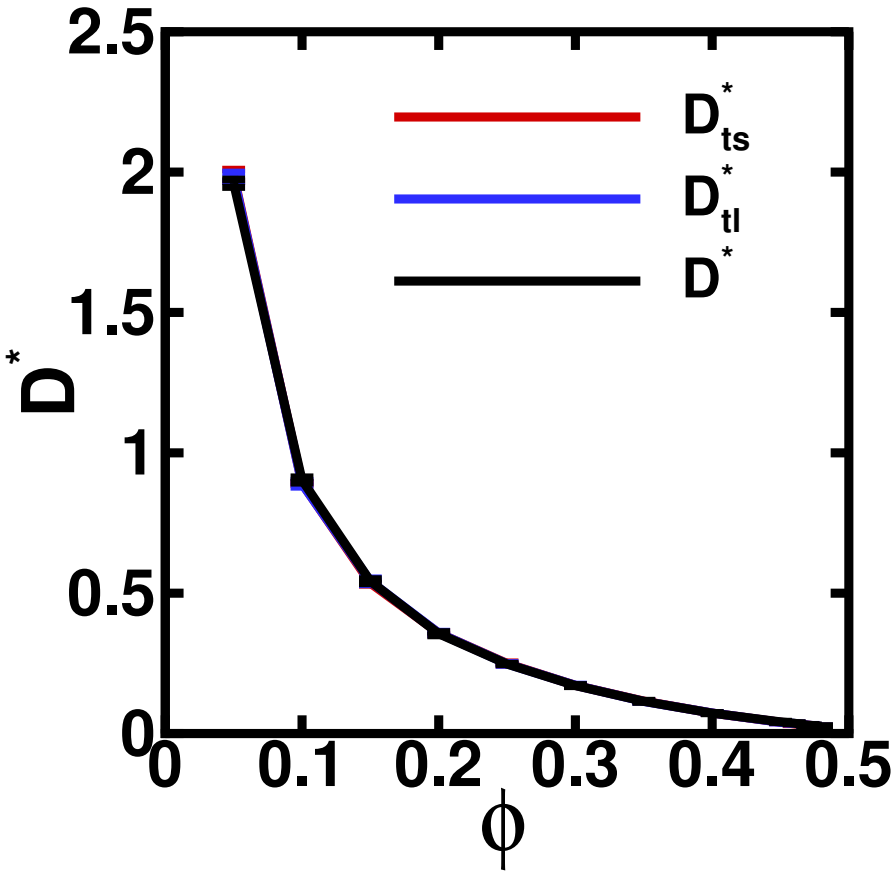

Figure 4.41: Convergence of the results of D^* with different Δt. The red curve and the blue curve is the same as in Fig. 4.40. The black curve is the diffusion coefficient calculated with parameters in Table 4.3 and is the data used for final results. This figure shows that the value of D^* is well converged with the chosen Δt and t_{max}.

4.11.1.1 Comparison with Literature

We compare our results of diffusion coefficient of the mono-disperse hard sphere system with published MD results in literature. [58] lists the diffusion coefficients for the mono disperse hard sphere system of size $N = 512$ at density $\phi = 0.10, 0.20, 0.30, 0.40, 0.494$. We compare our results with [58] at density $\phi = 0.10, 0.20, 0.30, 0.40$ in Fig. 4.42.

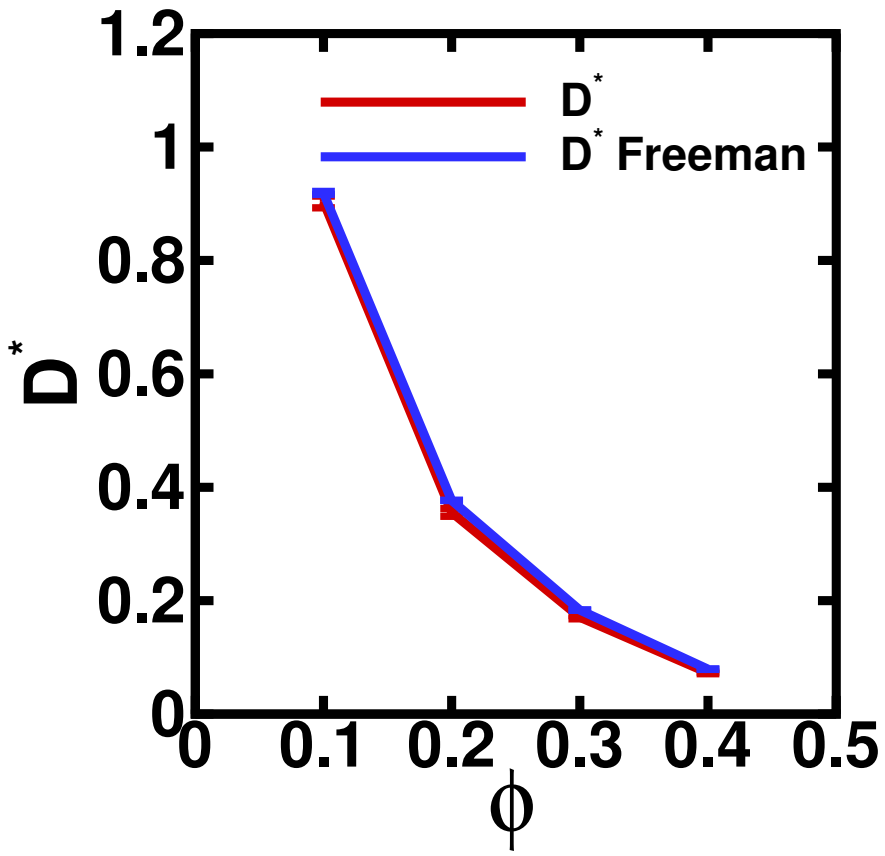

Figure 4.42: Comparison of our results of reduced diffusion coefficient D^* with literature results from [58]. The red curve is D^* from our MD results of $N = 108$. The blue curve D^* Freeman is the MD results from [58] of $N = 512$. The figure shows that our results are converged with the literature results.

[59] studied in detail the diffusion coefficients of the mono-disperse hard sphere liquid of different system sizes N for finite size effect. We compare our results with theirs in Fig. 4.43.

We investigate the finite size effect on the calculation of diffusion coefficients. De-

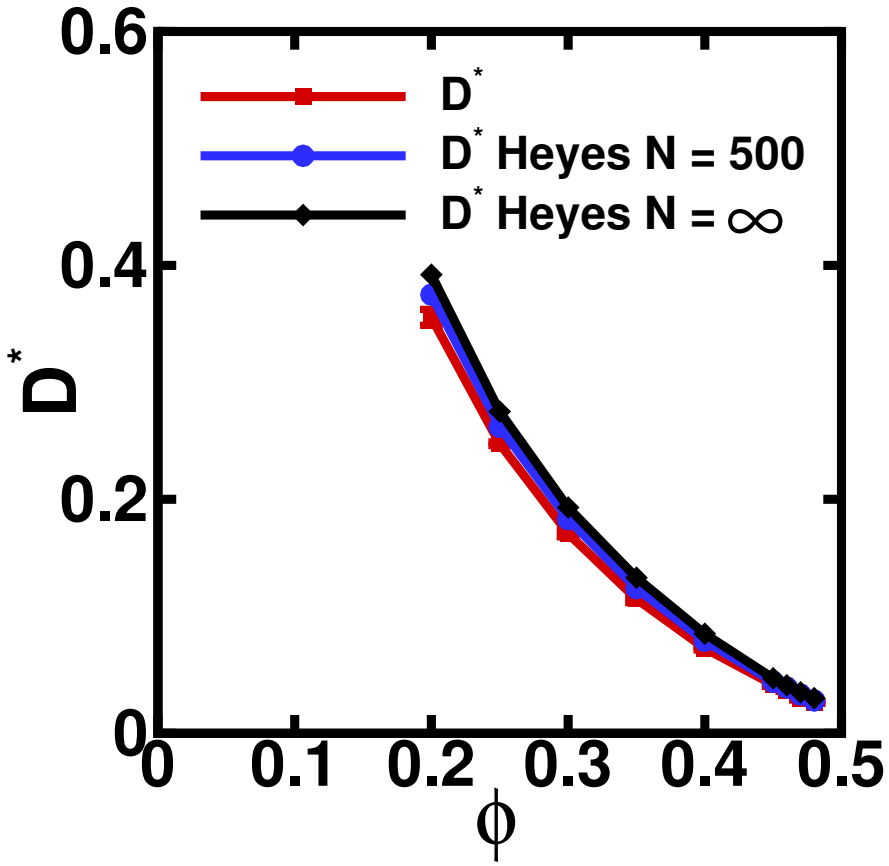

Figure 4.43: Comparison of our results of reduced diffusion coefficient D^* with literature results from [59]. The red curve is D^* from our MD results of $N = 108$. The blue curve D^* *Heyes* $N = 500$ is the MD results from [59] of $N = 500$. The black curve D^* *Heyes* $N = \infty$ is results from [59] where they obtained the data by extrapolation. The figure shows that there is a systematic finite-size effect on the result of D^*.

note the percentage error as $\epsilon = \frac{(D^* - D^*_{HeyesN=\infty})}{D^*_{HeyesN=\infty}}$, where D^* is the results of the reduced diffusion coefficient calculated by MD, and $D^*_{HeyesN=\infty}$ is the numerical results of the reduced diffusion coefficient of of $N = \infty$ from [59] obtained by extrapolation. The data from [58] of $N = 512$ has a percentage error ϵ around -5%. The data from [59] of $N = 500$ has a percentage error ϵ around -6%. The percentage error of our results of $N = 108$ is around -12%. The differences of results from different calculations are from finite size effect and fluctuation.

However, finite size effect acts as an overall constant in the absolute value of diffusion coefficient, so our results based on formula $D \propto \overline{(\Delta R/g)^2}$ are still valid. To

show this, we fit the diffusion coefficients from both the result of $N = 500$ from [59] and our MD result to the diffusion coefficient of $N = 4000$ from [59], by multiplying an overall constant c, which is obtained by matching the data at $\phi = 0.4$ respectively. The results are shown in Fig. 4.44.

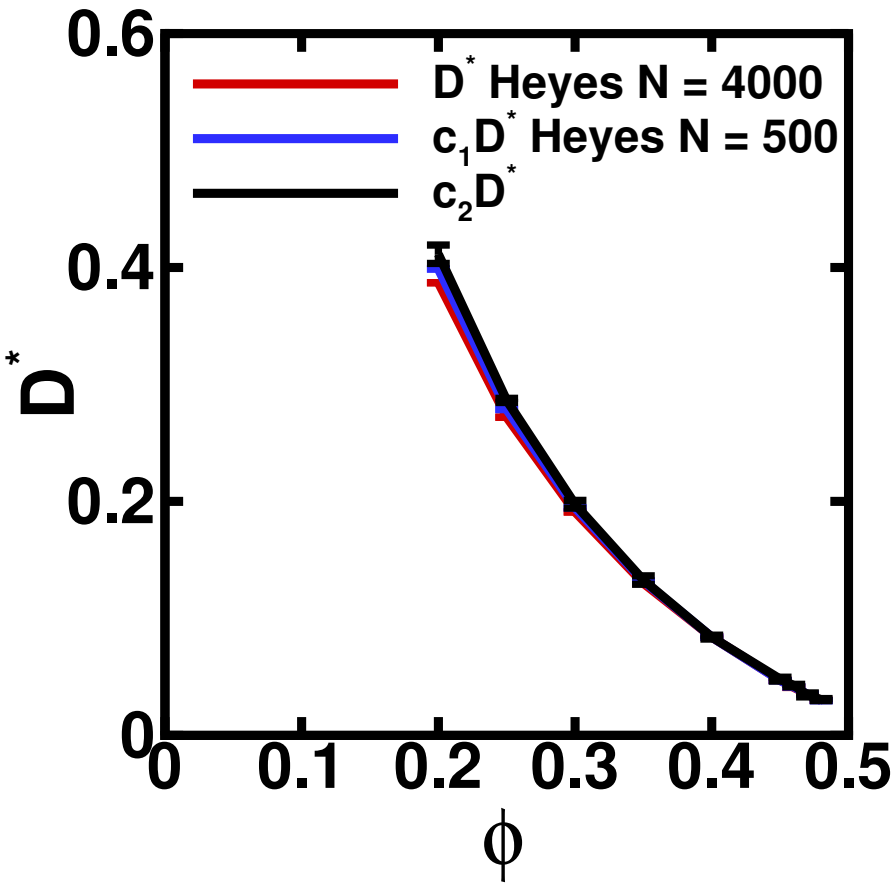

Figure 4.44: Finite size effect on the calculation of diffusion coefficient. The red curve D^* *Heyes* $N = 4000$ is results from [59]. The blue curve $c_1 D^*$ *Heyes* $N = 500$ is the MD results from [59] of $N = 500$ multiplied by constant c_1, $c_1 = \frac{D^*_{HeyesN=4000}}{D^*_{HeyesN=500}}$ at $\phi = 0.40$. The black curve $c_2 D^*$ is our MD results of D^* of $N = 108$ multiplied by constant c_2, $c_2 = \frac{D^*_{HeyesN=4000}}{D^*}$ at $\phi = 0.40$. The figures shows that finite size effect acts as an overall constant in the value of diffusion coefficient.

Fig. 4.45 shows the log scale of Fig. 4.44.

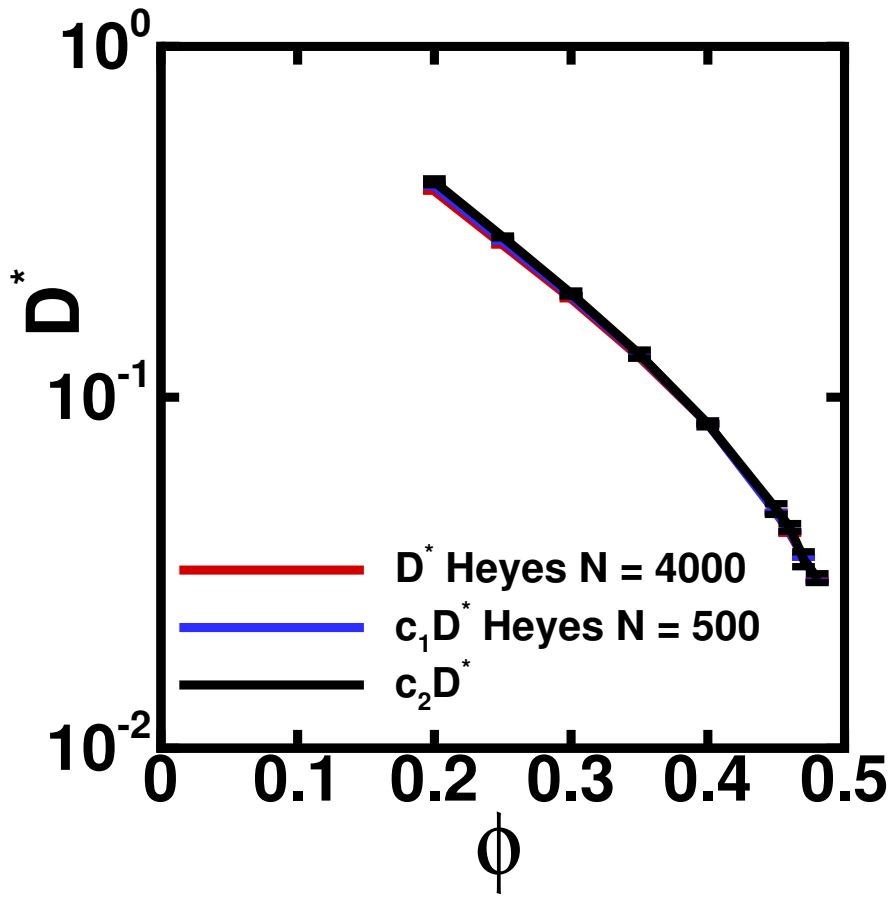

Figure 4.45: Log scale of Figure 4.44.

4.11.2 Binary Hard Sphere Liquid

The parameters used for calculating the diffusion coefficient of the binary hard sphere system is Table 4.5. The result is shown in Fig. 4.46.

We vary the value of Δt while fixing the value of t_{max} to test that Δt is small enough to give converged results. The parameters are in Table 4.6 and the result is shown in Fig. 4.47.

We also test with smaller values of t_{max} while fixing Δt to see that the value of t_{max} is big enough to generate converged results. The parameters are in Table 4.7 and the result is shown in Fig. 4.48.

ϕ	Δt	n	t_{max}
0.05	0.00060	40000	24
0.10,0.15	0.00040	40000	16
0.20,0.25	0.00020	40000	8
0.30,0.35	0.00015	40000	6
0.40,0.45	0.000010	40000	4
0.50-0.58	0.00002	100000	2

ϕ : packing fraction
Δt : time between two consecutively sampled configurations
n : number of intervals in Simpson's rule
t_{max} : upper limit of time for calculating velocity correlation

Table 4.5: Parameters for the calculation of the diffusion coefficient of the binary hard sphere system

ϕ	Δt	n	t_{max}
0.05	0.00120	20000	24
0.10,0.15	0.00080	20000	16
0.20,0.25	0.00040	20000	8
0.30,0.35	0.00030	20000	6
0.40,0.45	0.00020	20000	4
0.46-0.48	0.00005	40000	2

ϕ : packing fraction
Δt : time between two consecutively sampled configurations
n : number of intervals in Simpson's rule
t_{max} : upper limit of time for calculating velocity correlation

Table 4.6: Parameters for testing Δt for the calculation of the diffusion coefficient of the binary hard sphere system

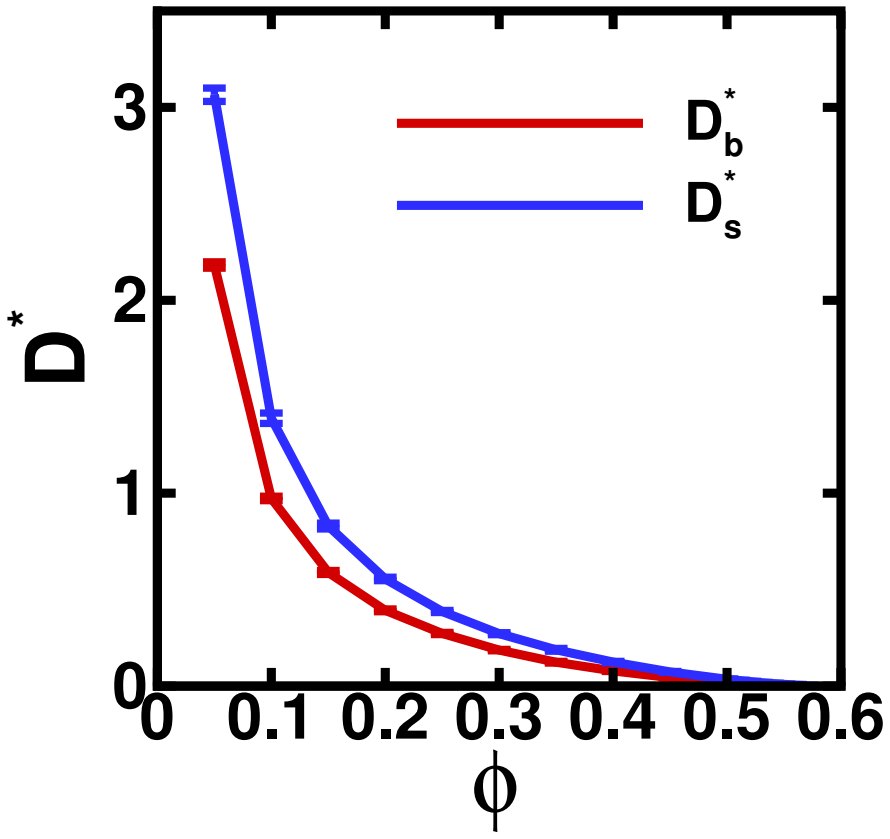

Figure 4.46: Reduced diffusion coefficient D^* as a function of ϕ of the binary hard sphere system. The red curve is the reduced self diffusion coefficient of big spheres D_b^*. The blue curve is the reduced self diffusion coefficient of small spheres D_s^*.

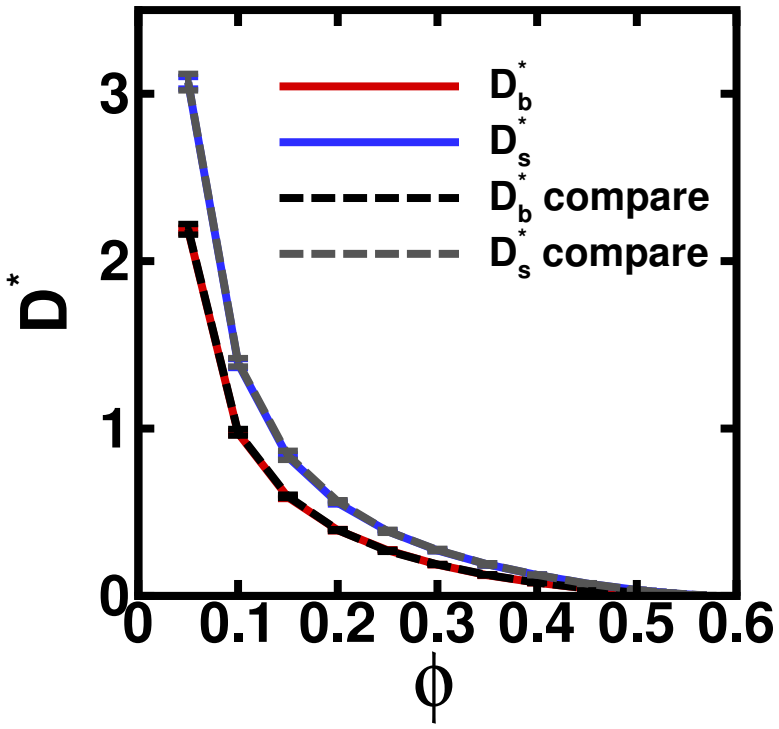

Figure 4.47: Convergence of the results of D^* with different Δt. The solid red curve and the solid blue curve are the reduced self diffusion coefficient for big spheres and small spheres respectively, calculated with parameters in Table 4.5. The dashed black curve and the dashed grey curve are the reduced self diffusion coefficient for big spheres and small spheres respectively, calculated with parameters in Table 4.6 which has a bigger value of Δt than Table 4.5 for each density. This figure shows that the value of D^* is well converged with the chosen Δt.

ϕ	Δt	n	t_{max}
0.05	0.00120	15000	18
0.10,0.15	0.00080	15000	12
0.20,0.25	0.00040	15000	6
0.30,0.35	0.00030	15000	4.5
0.40,0.45	0.00020	15000	3
0.46-0.48	0.00010	15000	1.5

ϕ : packing fraction
Δt : time between two consecutively sampled configurations
n : number of intervals in Simpson's rule
t_{max} : upper limit of time for calculating velocity correlation

Table 4.7: Parameters for testing t_{max} for the calculation of the diffusion coefficient of the binary hard sphere system

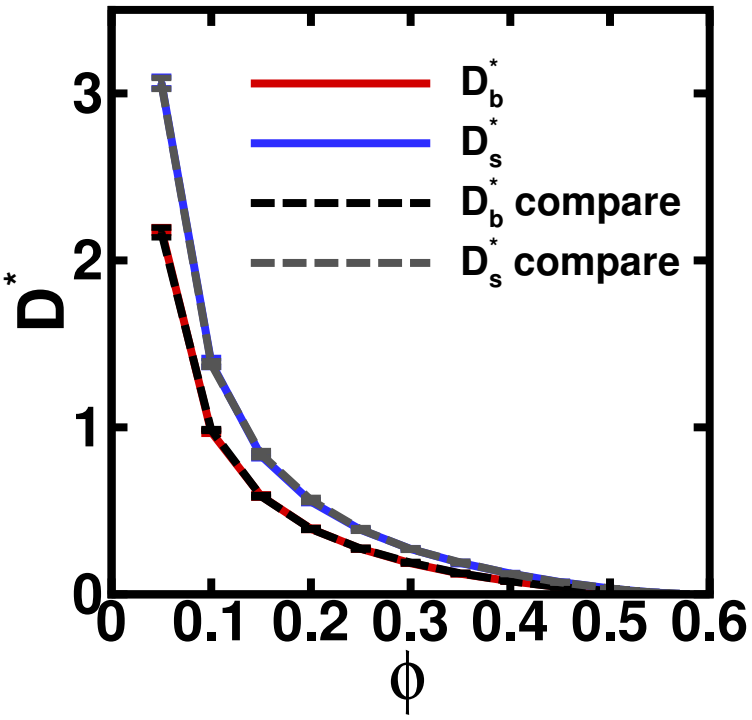

Figure 4.48: Convergence of the results of D^* with different t_{max}. The solid red curve and the solid blue curve are the reduced self diffusion coefficient for big spheres and small spheres respectively, calculated with parameters in Table 4.5. The dashed black curve and the dashed grey curve are the reduced self diffusion coefficient for big spheres and small spheres respectively, calculated with parameters in Table 4.7 which has a smaller value of t_{max} than Table 4.5 for each density. This figure shows that the value of D^* is well converged with the chosen t_{max}.

Chapter 5

Other Path-finding Methods

There are other methods of finding paths, some not necessarily the shortest path. These methods are documented in this chapter as well as some results. This chapter first presents a new method of path-finding for soft particle systems, which generates similar paths to the original method shown in Chapter 3 but with higher computational efficiency. Then this chapter records a method of path-finding for the hard sphere liquids, which generates longer paths than the method used in Chapter 3.

5.1 Soft Particle Liquid

5.1.1 Method

A new method of finding geodesics for soft particle liquids is given in this section. It follows the basic idea of the original method in Chapter3 based on Kuhn-Tucker theorem, that the path consists of segments of unconstrained steps ($V(\mathbf{R}) < E_L$) and segments of steps obeying the equality ($V(\mathbf{R}) = E_L$). Similar to the situation in the original method, the system always heads towards the end point until it hits an obstacle in the configuration space. The difference is how to form steps around the obstacles.

Given a pair of end points $\mathbf{R}_i$ and $\mathbf{R}_f$, the landscape energy E_L is the bigger value

of $V(\mathbf{R}_i)$ and $V(\mathbf{R}_f)$, $E_L = max(V(\mathbf{R}_i), V(\mathbf{R}_f))$. The system has a configuration $\mathbf{R} = (\mathbf{r}_1, \cdots, \mathbf{r}_j, \cdots, \mathbf{r}_N)$ and a potential energy $V = V(\mathbf{R})$.

The path consists of direct steps and contour steps.

1. Direct Step

   In direct step, the system always tries to go directly from its current position $\mathbf{R}(t)$ to the second end point $\mathbf{R}_f$, with a small step size δ_{di}. This part is the same as in the original method in Chapter 3. Direct steps form the segments of free propagation of a path based on Kuhn-Tucker theorem.

$$\mathbf{R}^0(t+1) = \mathbf{R}(t) + \delta_{di} \frac{\mathbf{R}_f - \mathbf{R}(t)}{|\mathbf{R}_f - \mathbf{R}(t)|} \tag{5.1}$$

   In calculation $\delta_{di} = 0.001\sigma$ is used.

   If the trial position $\mathbf{R}^0(t+1)$ is in the allowed region of configuration space($V(\mathbf{R}^0(t+1)) \leq E_L$), this $\mathbf{R}^0(t+1)$ is accepted as the new configuration of the system along the path. The system will proceed from there.

2. Contour Step

   If the trial position is in a forbidden region of configuration space($V(\mathbf{R}^0(t+1)) > E_L$), the system first retreats to its position $\mathbf{R}(t)$ before the failed direct step. The system then takes a contour step. (Similar to the case of hard sphere method in Chapter 3, the hard sphere system first retreats to its last allowed position before the failed direct step, then takes a collision avoidance step.)

   Denote the $3N$ dimensional gradient vector of potential energy function $V(\mathbf{R})$ as $\nabla V(\mathbf{R})$.

   The level set Φ of potential energy function V at an arbitrary configuration $\mathbf{R}(t)$ is

$$\Phi(\mathbf{R}(t)) = \{\mathbf{R} : V(\mathbf{R}) = V(\mathbf{R}(t))\} \tag{5.2}$$

The gradient of V at $\mathbf{R}(t)$ is perpendicular to the level set of V at $\mathbf{R}(t)$.

$$\nabla V(\mathbf{R}(t)) \perp \Phi(\mathbf{R}(t)) \tag{5.3}$$

Denote the unit vector pointing from the current position of the system $\mathbf{R}(t)$ to the second end point $\mathbf{R}_f$ as $\hat{\mathbf{d}}$.

$$\hat{\mathbf{d}} = \frac{\mathbf{R}_f - \mathbf{R}(t)}{|\mathbf{R}_f - \mathbf{R}(t)|} \tag{5.4}$$

$\hat{\mathbf{d}}$ can be decomposed to two perpendicular vectors $\mathbf{f}$ and $\mathbf{g}$, with $\mathbf{f}$ perpendicular to ∇V and $\mathbf{g}$ parallel to ∇V. $\mathbf{g}$ is the projection of $\hat{\mathbf{d}}$ along the direction of ∇V, and $\mathbf{f}$ is $\hat{\mathbf{d}} - \mathbf{g}$.

$$\hat{\mathbf{d}} = \mathbf{f} + \mathbf{g} \tag{5.5}$$

$$\mathbf{g} = \frac{\hat{\mathbf{d}} \cdot \nabla V}{|\nabla V|} \frac{\nabla V}{|\nabla V|} \tag{5.6}$$

$$\mathbf{f} = \hat{\mathbf{d}} - \mathbf{g} \tag{5.7}$$

$$\mathbf{g} \parallel \nabla V, \quad \mathbf{g} \perp \Phi(\mathbf{R}(t)) \tag{5.8}$$

$$\mathbf{f} \perp \nabla V, \quad \mathbf{f} \parallel \Phi(\mathbf{R}(t)) \tag{5.9}$$

$$\mathbf{f} \perp \mathbf{g} \tag{5.10}$$

Since $\mathbf{f} \perp \nabla V$, if the system moves along the direction $\mathbf{f}$, the move does not

increase the potential energy V. We can move the system according to

$$\mathbf{R}^0(t+1) = \mathbf{R}(t) + \delta_{di}\hat{\mathbf{f}} \tag{5.11}$$

$$\hat{\mathbf{f}} = \frac{\mathbf{f}}{|\mathbf{f}|} \tag{5.12}$$

$$\delta_{di} = 0.001\sigma \tag{5.13}$$

Contour steps form the segments of a path that satisfy the constraints as equality based on Kuhn-Tucker theorem.

Equation 5.11 does not increase the potential energy of the system in principle. Due to numerical precision in calculation, in some cases the move may need a small component in the direction of $-\mathbf{g}$ to decrease the potential energy a little bit. An iteration is used to deal with this situation.

$$\mathbf{R}^n(t+1) = \mathbf{R}(t) + \delta_{di}\hat{\mathbf{f}} - \delta_c^n \frac{\nabla V}{|\nabla V|} \tag{5.14}$$

$$\delta_c^n = 10^{-5} n\sigma \tag{5.15}$$

where $n = 0, 1, 2, \cdots, n_{max}$ is the index of iteration. The iteration stops when $V(\mathbf{R}^n(t+1)) \leq E_L$. In most cases, no iteration is needed and $n_{max} = 0$. In some cases two or three iterations are needed. (In the original method in Chapter 3 a tolerance δV is used to deal with numerical error, which serves the same purpose.) The configuration $\mathbf{R}^{n_{max}}(t+1)$ is accepted as the new configuration of the system along the path. The system proceeds from there.

3. A path is found when the distance between the current configuration of the system $\mathbf{R}(t)$ and the second end point $\mathbf{R}_f$ is smaller than δ_{di}.

$$|\mathbf{R}_f - \mathbf{R}(t)| < \delta_{di} \tag{5.16}$$

The path length l is the sum of the lengths of every successful step (steps connecting two consecutive allowed configurations) along the path.

$$l = \sum_{t=0}^{t=P} |\mathbf{R}(t+1) - \mathbf{R}(t)| \tag{5.17}$$

where P is the total number of steps along the path, $\mathbf{R}(0) = \mathbf{R}_i$, $\mathbf{R}(P+1) = \mathbf{R}_f$.

This method is shown in Algorithm 4.

Algorithm 4 New method of path finding for soft particle systems

$E_L \leftarrow MAX(V(\mathbf{R}_i), V(\mathbf{R}_f))$
$l \leftarrow 0$ ▷ path length
$\mathbf{R}_t$ ▷ current configuration of the system
$\mathbf{R}_o$ ▷ previous allowed configuration of the system
$\mathbf{R}_t \leftarrow \mathbf{R}_i$, $\mathbf{R}_o \leftarrow \mathbf{R}_i$
while $|\mathbf{R}_f - \mathbf{R}_t| > \delta_{di}$ **do** ▷ $\delta_{di} = 0.001\sigma$
$\mathbf{R}_o \leftarrow \mathbf{R}_t$
$\mathbf{R}_t \leftarrow \mathbf{R}_t + \delta_{di}\dfrac{\mathbf{R}_f - \mathbf{R}_t}{|\mathbf{R}_f - \mathbf{R}_t|}$ ▷ direct step
  if $V(\mathbf{R}_t) > E_L$ **then**
    $\mathbf{R}_t \leftarrow$ ContourStep($\mathbf{R}_o$) ▷ contour step
  end if
$l \leftarrow l + |\mathbf{R}_t - \mathbf{R}_o|$
end while
return l

procedure ContourStep($\mathbf{R}_o$)
  $\mathbf{R}$
  $\delta_c \leftarrow 0$
  $\hat{\mathbf{d}} \leftarrow \frac{\mathbf{R}_f - \mathbf{R}_o}{|\mathbf{R}_f - \mathbf{R}_o|}$
  $\hat{\nabla V} \leftarrow \frac{\nabla V}{|\nabla V|}$
  repeat
    $\mathbf{R} \leftarrow \mathbf{R}_o + \delta_{di}\dfrac{\hat{\mathbf{d}} - (\hat{\mathbf{d}} \cdot \hat{\nabla V})\hat{\nabla V}}{|\hat{\mathbf{d}} - (\hat{\mathbf{d}} \cdot \hat{\nabla V})\hat{\nabla V}|} - \delta_c \hat{\nabla V}$ ▷ $\delta_{di} = 0.001\sigma$
    $\delta_c \leftarrow \delta_c + 10^{-5}\sigma$
  until $V(\mathbf{R}) \leq E_L$
return R
end procedure

5.1.2 Results

The procedure of setting up molecular dynamics and finding pairs of end points is the same as in Chapter 3.

5.1.2.1 Parameter Testing

The step size $\delta_{di} = 0.001\sigma$ is used throughout the calculations with the new method. Fig. 5.1 shows the convergence of $(\frac{\Delta R}{g})^2$ with respect to the parameter δ_{di}.

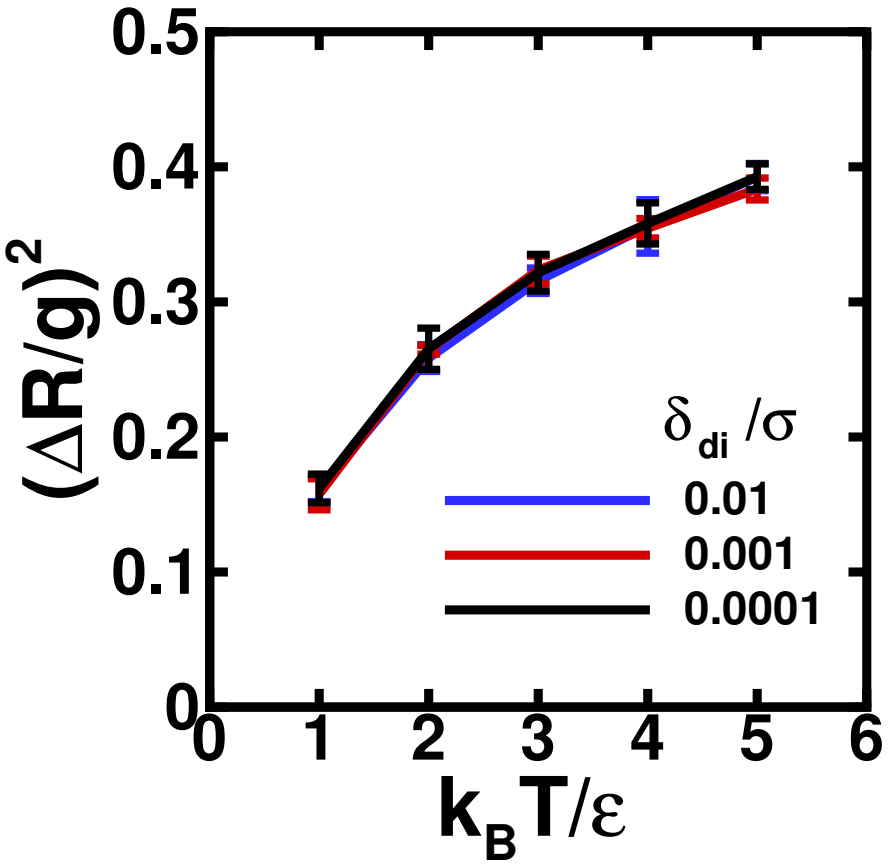

Figure 5.1: Parameter test of δ_{di} of the new path finding method. The system is Kob-Andersen liquid of size $N = 108$. The reduced temperature k_BT/ϵ decreases from 5.0 to 1.0. The results are averaged over 5 unoptimized paths of $\Delta R = 108\sigma$.

Fig. 5.1 shows that the path lengths generated with the three different tested values of the parameter δ_{di} are numerically very close. Computationally the time t

needed to find a path is $t(\delta_{di} = 0.01\sigma) < t(\delta_{di} = 0.001\sigma) < t(\delta_{di} = 0.0001\sigma)$. Because in the original method $\delta_{di} = 0.001\sigma$ is used as the direct step length, here $\delta_{di} = 0.001\sigma$ is chosen.

5.1.2.2 Convergence of the Paths

Fig. 5.2 shows the convergence of $(\frac{\Delta R}{g})^2$ with respect to ΔR with the new path finding method. Fig. 5.3 shows the convergence of $(\frac{\Delta R}{g})^2$ with respect to ΔR with the original path finding method. Comparing the graphs, the new method has similar convergence rates to the original method with respect to ΔR.

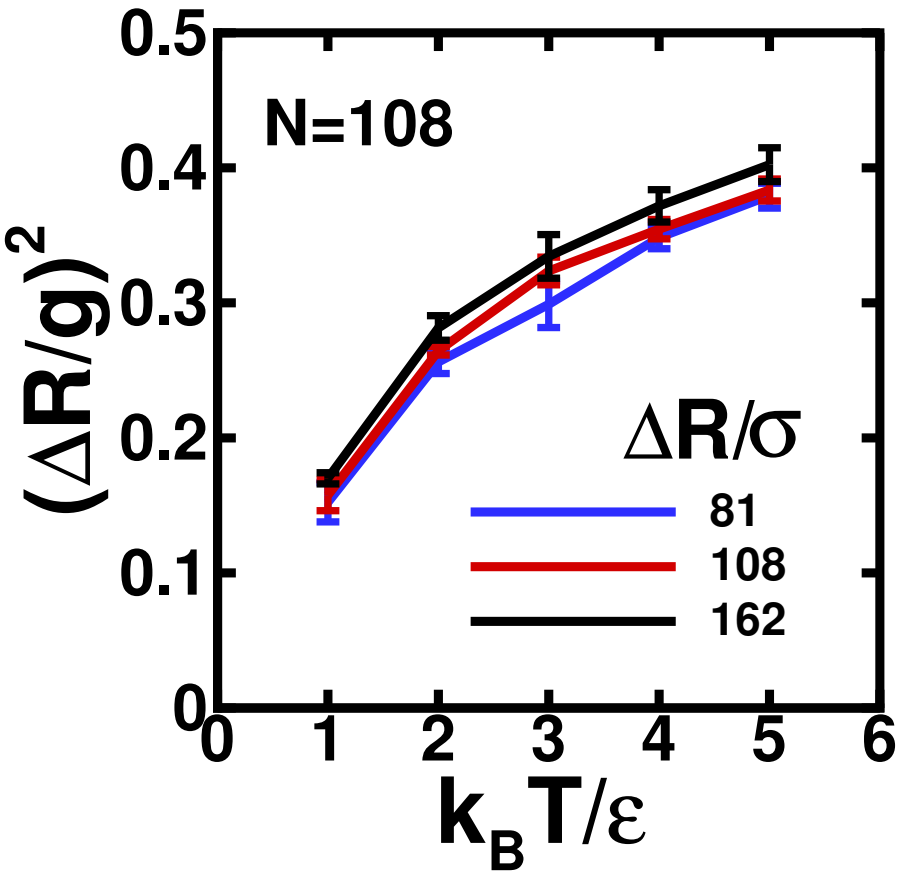

Figure 5.2: Convergence of $(\frac{\Delta R}{g})^2$ with respect to ΔR with the new path finding method. The system is Kob-Andersen liquid of size $N = 108$. The reduced temperature $k_B T/\epsilon$ decreases from 5.0 to 1.0. The results are averaged over 5 unoptimized paths. The figure shows that $(\frac{\Delta R}{g})^2$ is converged with ΔR within fluctuation.

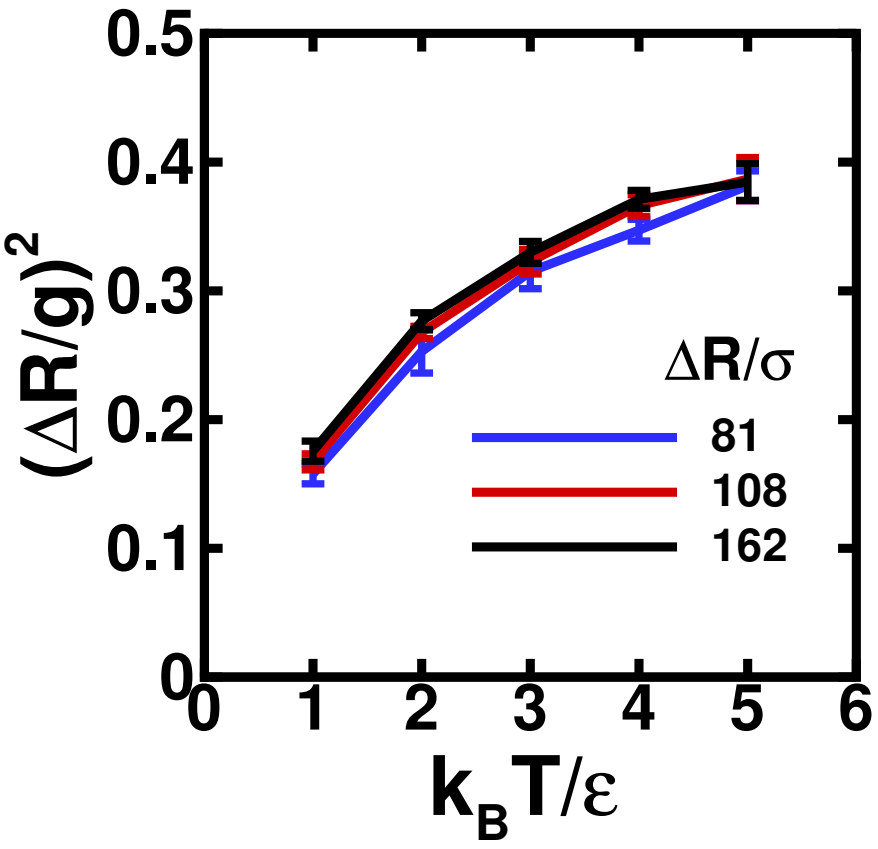

Figure 5.3: Convergence of $(\frac{\Delta R}{g})^2$ with respect to ΔR with the original path finding method. The system is Kob-Andersen liquid of size $N = 108$. The reduced temperature $k_B T/\epsilon$ decreases from 5.0 to 1.0. The results are averaged over 5 unoptimized paths. The figure shows that $(\frac{\Delta R}{g})^2$ is converged with ΔR within fluctuation.

Fig. 5.4 shows the convergence of $(\frac{\Delta R}{g})^2$ with respect to N with the new path finding method. Fig. 5.5 shows the convergence of $(\frac{\Delta R}{g})^2$ with respect to N with the original path finding method. Comparing the graphs, the new method has similar convergence rates to the original method with respect to N.

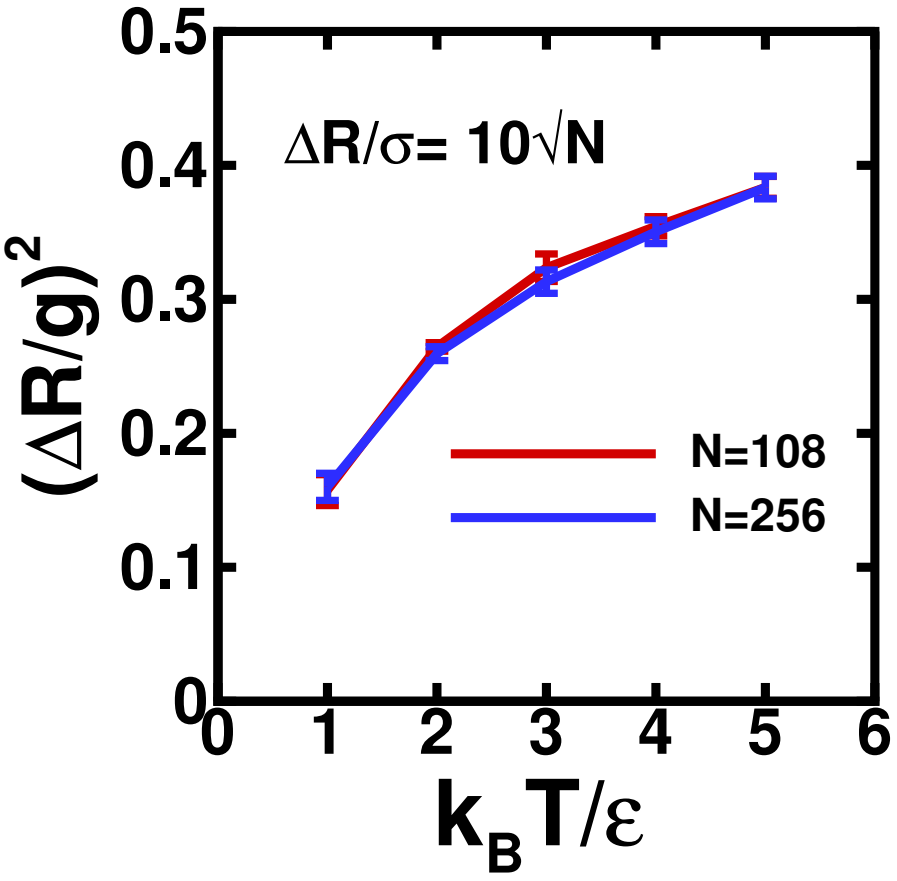

Figure 5.4: Convergence of $(\frac{\Delta R}{g})^2$ with respect to N with the new path finding method. The system is Kob-Andersen liquid of sizes $N = 108$ and $N = 256$. The reduced temperature $k_B T/\epsilon$ decreases from 5.0 to 1.0. The results are averaged over 5 unoptimized paths. The figure shows that $(\frac{\Delta R}{g})^2$ is converged with N within fluctuation.

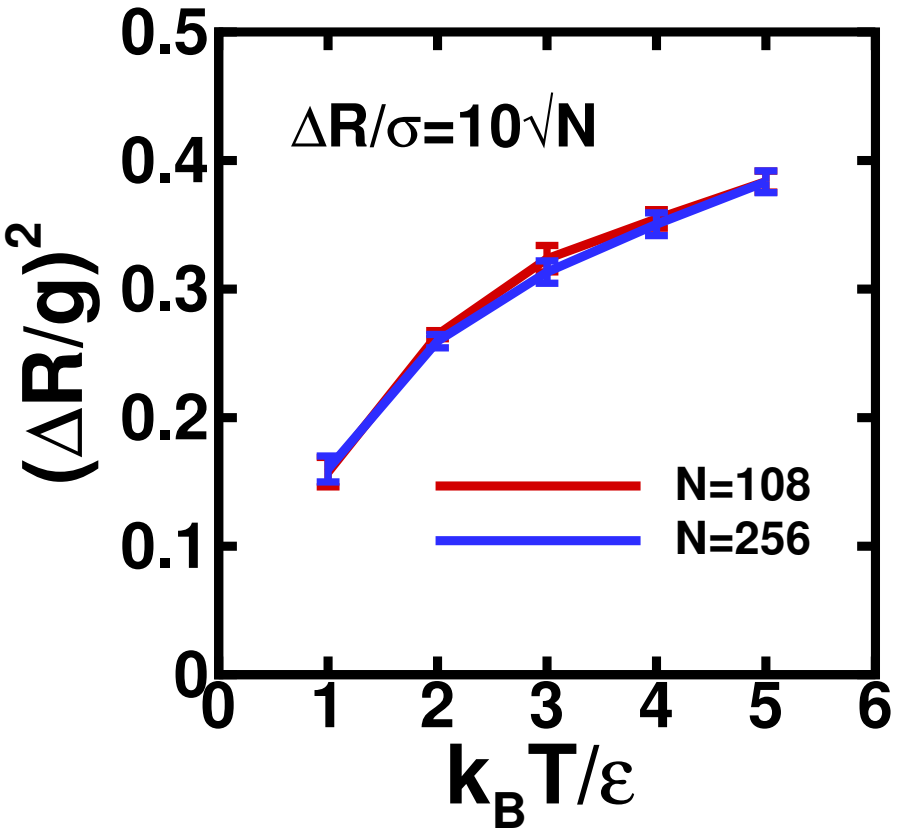

Figure 5.5: Convergence of $(\frac{\Delta R}{g})^2$ with respect to N with the original path finding method. The system is Kob-Andersen liquid of sizes $N = 108$ and $N = 256$. The reduced temperature $k_B T/\epsilon$ decreases from 5.0 to 1.0. The results are averaged over 5 unoptimized paths. The figure shows that $(\frac{\Delta R}{g})^2$ is converged with N within fluctuation.

5.1.2.3 $(\frac{\Delta R}{g})^2$

Fig. 5.6 shows the comparison of $(\frac{\Delta R}{g})^2$ with the new method and with the original method.

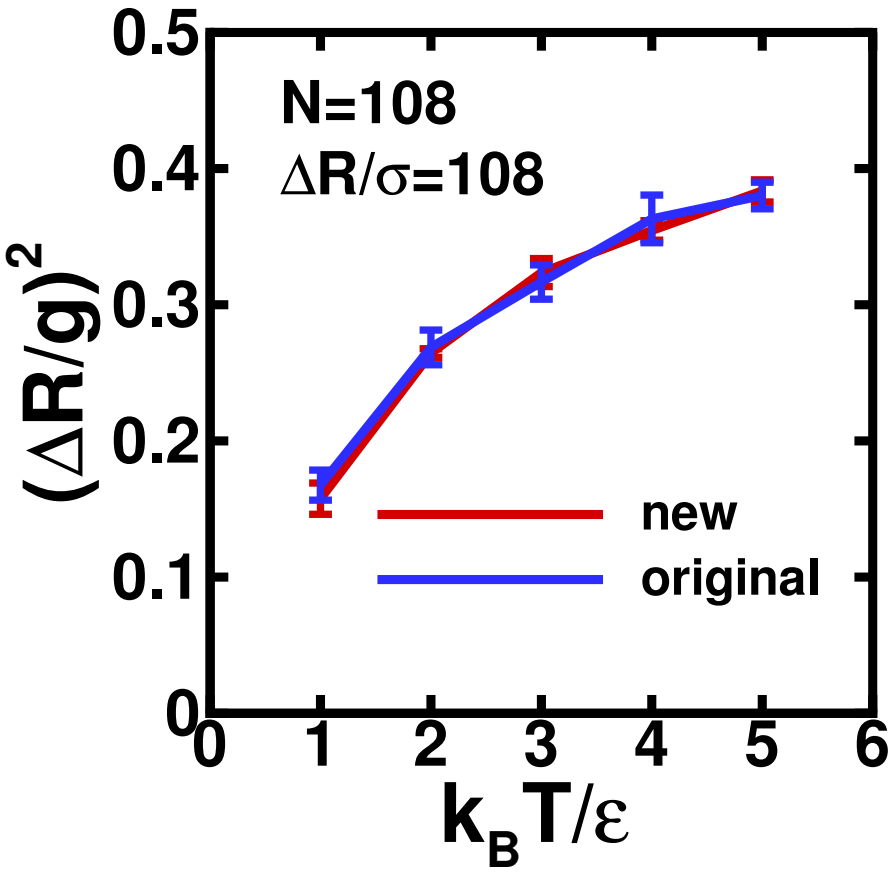

Figure 5.6: Comparison of $(\frac{\Delta R}{g})^2$ with the new method and with the original method. The system is Kob-Andersen liquid of size $N = 108$. The reduced temperature k_BT/ϵ decreases from 5.0 to 1.0. The results of both methods are averaged over 5 unoptimized paths of $\Delta R = 108\sigma$. The figure shows that the two methods give close numerical results for $(\frac{\Delta R}{g})^2$.

5.1.2.4 Participating Ratio

Fig. 5.7 shows the convergence of participation ratio n/N with respect to N with the new path finding method.

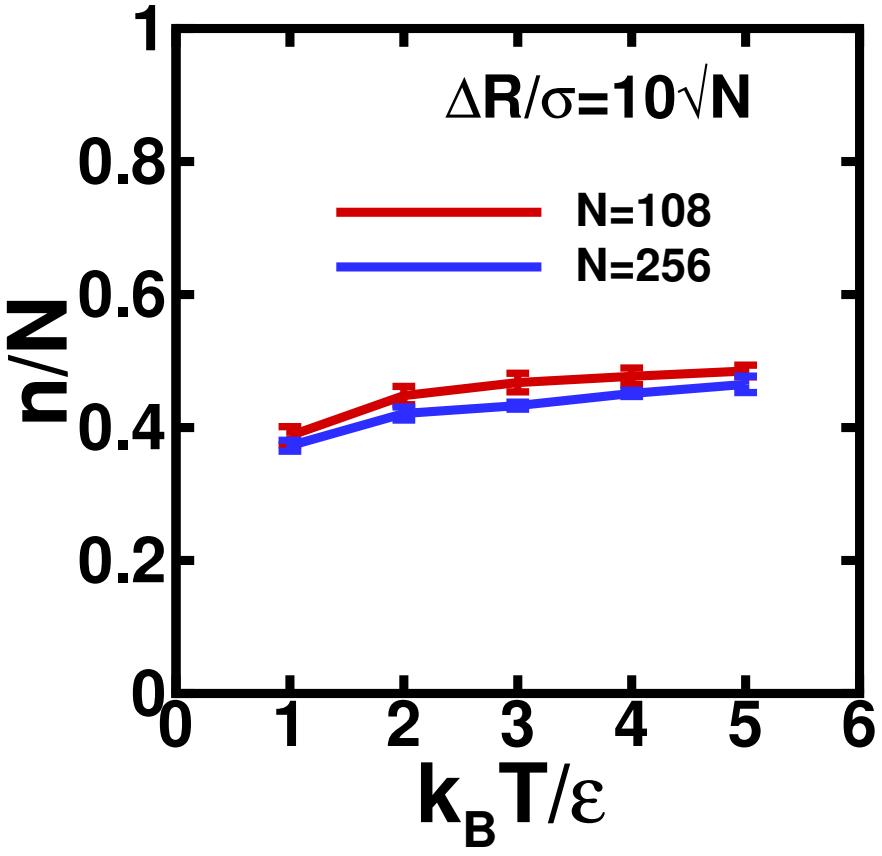

Figure 5.7: Convergence of the participation ratio n/N with respect to N with the new path finding method for the Kob-Andersen liquid. The reduced temperature k_BT/ϵ decreases from 5.0 to 1.0. The results are averaged over 5 unoptimized paths. The figure shows that n/N is converged with N within fluctuation. The motions along the paths are therefore macroscopic.

Fig. 5.8 shows the comparison of participation ratio $\frac{n}{N}$ with the new method and with the original method.

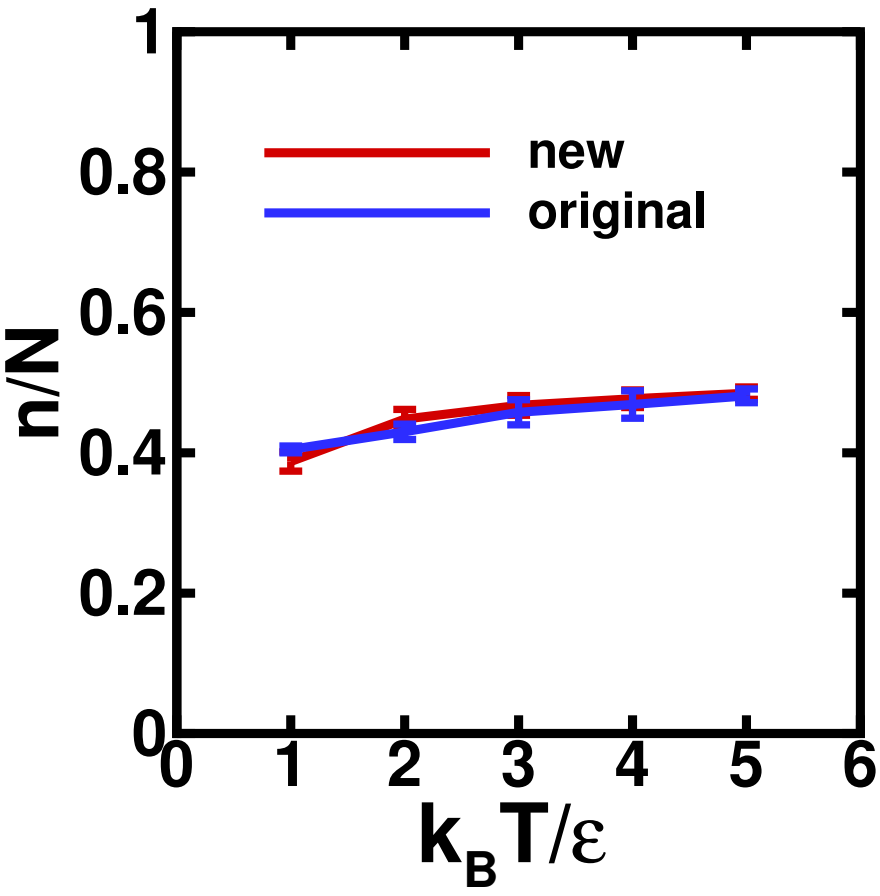

Figure 5.8: Comparison of participation ratio n/N with the new method and with the original method for the Kob-Andersen liquid. The reduced temperature k_BT/ϵ decreases from 5.0 to 1.0. The results of both methods are averaged over 5 unoptimized paths of $N = 108$ and $\Delta R = 108\sigma$. The figure shows that the two methods give close numerical results of $\frac{n}{N}$.

5.1.3 Comparison of Methods

All the above figures show that the new method is able to generate converged paths, and the results are numerically very close to those of the original method. The two methods are both based on Kuhn-Tucker theorem, with the difference in implementing the segments of paths that obey the constraints as equality. The contour step in the new method, as the counterpart of the escape step in the original method, allows the system to move along the boundary too. The system does retreat to the allowed configuration first before the contour step, and that configuration does not usually lie

exactly on the boundary. But as long as the step length is small, the configuration is still very close to the boundary, so is the contour step.

In the escape step in the original method, iteration is needed in the gradient descend method to find the nearest allowed configuration from the disallowed trial location. In the new method, no such iteration is needed. This saves computational time because it does not have to compute the potential energy multiple times for one step. We compare the computational performance of the two methods in Table 5.1. The time listed in the table is the rough average amount of time needed for a method to find a path, given a pair of end points, averaged over 5 unoptimized paths of $N = 108$ and $\Delta R = 108\sigma$ for Kob-Andersen liquid. The table shows that the efficiency of the new method is about 10 times higher than the original method.

k_BT/ϵ	time(seconds) - new method	time(seconds) - original method
5.0	750	12000
4.0	800	12000
3.0	850	12000
2.0	900	13000
1.0	1100	15000

Table 5.1: Comparison of computational performance of the new method and the original method. The table lists the time needed to find a path for both methods. Both results are averaged from 5 unoptimized paths of $N = 108$ and $\Delta R = 108\sigma$ for Kob-Andersen liquid. The new method consumes about one tenth of the time of the original method to find a path.

Another advantage of the new method is that, if the nearest allowed configuration $\mathbf{R}$ where the escape step in the original method takes the system to happens to have the property that $\hat{\mathbf{d}}$ is perpendicular to $\nabla V(\mathbf{R})$, the next direct step would take the system back to the forbidden region, then the following escape step would take the system back to the same nearest allowed point $\mathbf{R}$ again. The program would stay in an infinite loop. The new method, on the other hand, does not have this problem.

5.2 Hard Sphere Liquid

This section records a previous trial method of finding paths for hard sphere liquids. While this method does find paths for hard sphere systems at low densities, the paths it generates have wrong scaling behavior and are longer than the method in Chapter 3.

5.2.1 Method

Given a pair of end points $\mathbf{R}_i$ and $\mathbf{R}_f$, a hard sphere system always have a landscape energy $E_L = 0$. The system has a configuration $\mathbf{R} = (\mathbf{r}_1, \cdots, \mathbf{r}_j, \cdots, \mathbf{r}_N)$. The potential energy V is 0 for every allowed configuration and ∞ for any disallowed configuration. No overlap is allowed in any allowed configuration in the potential energy landscape ensemble.

The path consists of direct steps and away steps.

- Direct Step

  The system always tries to move from its current configuration $\mathbf{R}(t)$ towards the final configuration $\mathbf{R}_f$ directly, until two particles are about to overlap. If we assign each particle a fictitious velocity $\mathbf{v}_j$ $(j = 1, 2, \cdots, N)$,

$$\mathbf{v}_j = \mathbf{r}_{jf} - \mathbf{r}_j(t) \tag{5.18}$$

  where $\mathbf{r}_{jf}$ is the position of particle j in the final configuration $\mathbf{R}_f$, $\mathbf{r}_j(t)$ is the position of particle j in the current configuration $\mathbf{R}(t)$, then using collision dynamics same as in the molecular dynamics [47], we can calculate the time interval Δt the system can travel until the moment when two particles are in contact. We calculate the collision time interval t_{ij} between particle i and j $(i = 1, 2, \cdots, N-1,\ j = i+1, \cdots, N)$. The first pair to collide has the minimum value of t_{ij}, denoted as Δt. Denote the colliding pair as particle p and

particle q. $\Delta t = t_{pq}$.

The system is moved according to

$$\mathbf{r}_j(t+1) = \mathbf{r}_j(t) + \Delta t \cdot \mathbf{v}_j \quad j = 1, \cdots, N \tag{5.19}$$

$$\Delta t = \min\{t_{ij}\}, \quad i = 1, \cdots, N, j = i+1, \cdots, N \tag{5.20}$$

The time t the system needs to move from its current configuration to the final configuration with the assigned velocity is $t = 1.0$. Thus if $\Delta t \geq 1.0$, it means the system can move to the final configuration without any collisions. This happens at the last step of the path where the system is moved to the final configuration directly. Along the path $\Delta t < 1.0$.

This step is similar to the direct step in the soft particle case where

$$\mathbf{R}(t+1) = \mathbf{R}(t) + \delta_{di} \frac{\mathbf{R}_f - \mathbf{R}(t)}{|\mathbf{R}_f - \mathbf{R}(t)|} \tag{5.21}$$

$$\delta_{di} = |\mathbf{v} \cdot \Delta t| \tag{5.22}$$

$$\mathbf{v} = (\mathbf{v}_1, \cdots, \mathbf{v}_j, \cdots, \mathbf{v}_N) \quad j = 1, \cdots, N \tag{5.23}$$

- Away Step

  After the direct step, particle p and particle q are in contact. Further move along the previous direction would cause overlapping between the two particles, thus a change of direction is needed.

  First we need to decide which particle is in which particle's way in the current configuration. The volume taken by the motion of a sphere along a direct line is a cylinder. For example, the position of the center of particle q $\mathbf{r}_q = (r_{qx}, r_{qy}, r_{qz})$ and its direction to go $\mathbf{v}_q = (v_{qx}, v_{qy}, v_{qz})$ forms a ray. This ray is the axis of the cylinder formed by particle q, denoted as cylinder q. Cylinder q is of radius

$\frac{1}{2}\sigma_q$.

If any part of particle p is in cylinder q, it means particle p is in particle q's way, and vice versa. Denote the distance from the center of particle p to the axis of cylinder q as d_{pq}. d_{pq} is a point-to-line distance. If $d_{pq} < \frac{1}{2}(\sigma_p + \sigma_q)$, then particle p is in particle q's way. If $d_{pq} \geq \frac{1}{2}(\sigma_p + \sigma_q)$, then particle p is not in cylinder q so particle p is not in particle q's way. We can test whether particle q is in particle p's way by the same procedure.

Between the two colliding particles p and q, we decide which particle to move out of the other particle's way by the following procedure. If particle p is in particle q's way but particle q is not in particle p's way, we move particle p out of particle q's cylinder. If particle q is in particle p's way but particle p is not in particle q's way, we move particle q out of particle p's cylinder. If they are both in each other's way, we move whichever particle that is closer to its final position out of the other particle's way.

Suppose now we need to move particle p out of particle q's cylinder. The case of moving particle q out of particle p's cylinder is symmetrical. The configuration of the system is the updated $\mathbf{R}(t)$ after the previous direct step. Particle p and particle q are in contact. The distance from the center of particle p to the axis of cylinder q is d_{pq}. The minimum distance d that particle p needs to move in order to be totally out of cylinder q is $d = \frac{1}{2}(\sigma_p + \sigma_q) - d_{pq}$. The direction with this shortest distance is that particle p moving directly away from the axis of the cylinder, following the straight line perpendicular to the axis of the cylinder and going through the center of particle p.

When moving particle p out of the cylinder of particle q, what often happens is, another particle k may be in the way of particle p. In this situation, we calculate the distance needed to move particle k out of the cylinder of particle p and then move particle k accordingly. If another particle m is in particle k's

way of moving out of the cylinder of particle p, we apply the same procedure to calculate the distance that particle m needs to move and then move particle m accordingly. The iteration runs until there is no more particle in the way. For example, if particle n is in particle m's way, we move particle n by the distance calculated from the above procedure, and the iteration stops if there is no particle in particle n's way.

After this move of particle p and possibly some other particles such as particle k and particle m, we move particle q by a small distance. Particle p has been moved entirely out of the cylinder of particle q so we should have $d_{pq} \geq \frac{1}{2}(\sigma_p + \sigma_q)$. We move particle q in the direction of $\mathbf{v}_q$ to the point $\mathbf{q}'$ where the projection of the center of particle p on the axis of the cylinder q is. $\mathbf{q}'$ is the projection point of the point-to-line projection. Denoting the position of particle p as $\mathbf{r}_p = (r_{px}, r_{py}, r_{pz})$ and the axis of cylinder q as $\mathbf{v}_q = (v_{qx}, v_{qy}, v_{qz})$, the projection point $\mathbf{q}'$ is then $\mathbf{q}' = (\mathbf{r}_p \cdot \frac{\mathbf{v}_q}{|\mathbf{v}_q|}) \cdot \frac{\mathbf{v}_q}{|\mathbf{v}_q|}$. After this move the axis of particle q's cylinder is perpendicular to the line connecting the center of particle q and the center of particle p. $\mathbf{v}_q \perp (\mathbf{r}_q - \mathbf{r}_p)$. If there are some particles in the way while moving particle q, they are moved with the same procedure in the above paragraph.

All the above moves are counted as one step in the procedure. The step length is the distance between the new configuration and the old configuration right after the direct step.

An illustration of away step is given in Fig. 5.9.

- Path length

  A path is found when the collision time $\Delta t = t_{pq}$ is bigger than 1.0. Because in direct step, the time needed for the system to go from the current configuration to the end point with the assigned velocities is 1.0, so if $\Delta t > 1.0$, it means the system can go to the end point before having any collision. The system is

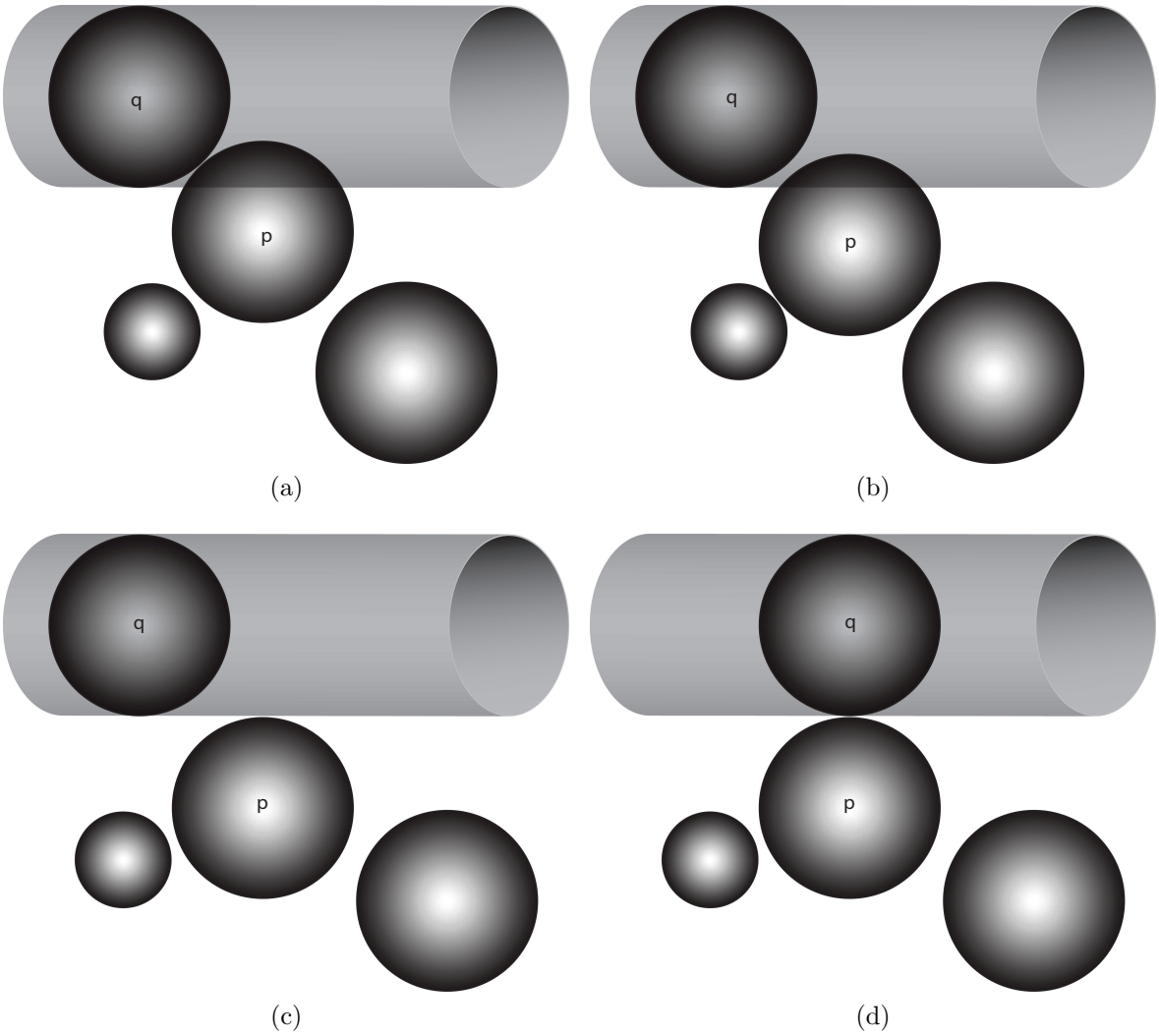

Figure 5.9: Illustration of away step. Particle q is the up left particle and cylinder q is shown. After a direct step, particle p and particle q are in contact, and a part of particle p is in cylinder q, shown in (a). The away step moves particle p out of cylinder q, moving other particles if necessary, shown in (b) and (c). Then particle q is moved to position $\mathbf{q}'$, shown in (d).

moved according to

$$\mathbf{r}_j(t+1) = \mathbf{r}_j(t) + 1.0 \cdot \mathbf{v}_j \quad j = 1, \cdots, N \tag{5.24}$$

This is the last step of the whole path. After this step, the system is at the second end point.

The path length l is the sum of the length of every successful steps (steps connecting two consecutive allowed configurations) along the path.

$$l = \sum_{t=0}^{t=P} |\mathbf{R}(t+1) - \mathbf{R}(t)| \tag{5.25}$$

where P is the total number of steps along the path, $\mathbf{R}(0) = \mathbf{R}_i$, $\mathbf{R}(P+1) = \mathbf{R}_f$.

For the binary hard sphere system, this method is able to find paths for packing fraction ϕ up to 0.45. It fails to generate paths most of the time at higher packing fractions.

5.2.2 Results

This section gives results with this path finding method. The procedure of setting up molecular dynamics and finding pairs of end points is the same as in Chapter 3. All the results below are averaged over 5 unoptimized paths.

Fig. 5.10 shows the convergence of $(\frac{\Delta R}{g})^2$ with respect to ΔR.

Fig. 5.11 compares the results of $(\frac{\Delta R}{g})^2$ from this old method and the new method in Chapter 3. The comparison demonstrates that the new method is better.

Fig. 5.12 shows the values of $(\frac{\Delta R}{g})^2$ for different N with this method. It shows this method does not work because the results do not converge with different system sizes N.

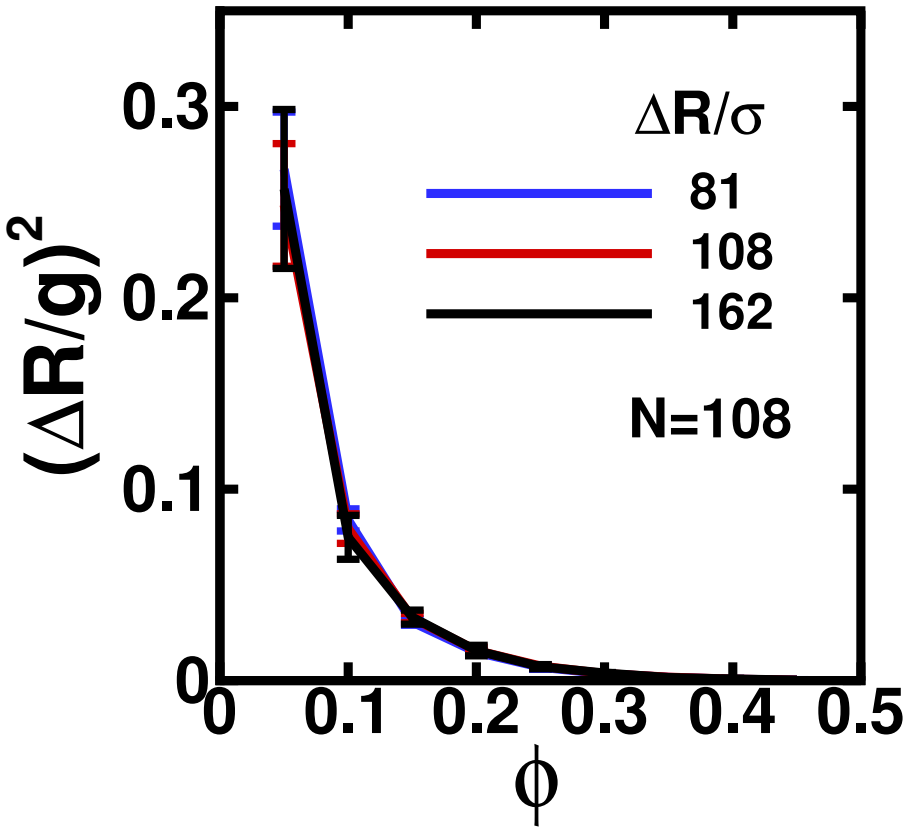

Figure 5.10: Convergence of $(\frac{\Delta R}{g})^2$ with respect to ΔR with the old path finding method for the binary hard sphere liquid. The packing fraction ϕ goes from 0.05 to 0.45. The results are averaged over 5 unoptimized paths of $N = 108$. The figure shows that $(\frac{\Delta R}{g})^2$ is converged with ΔR within fluctuation.

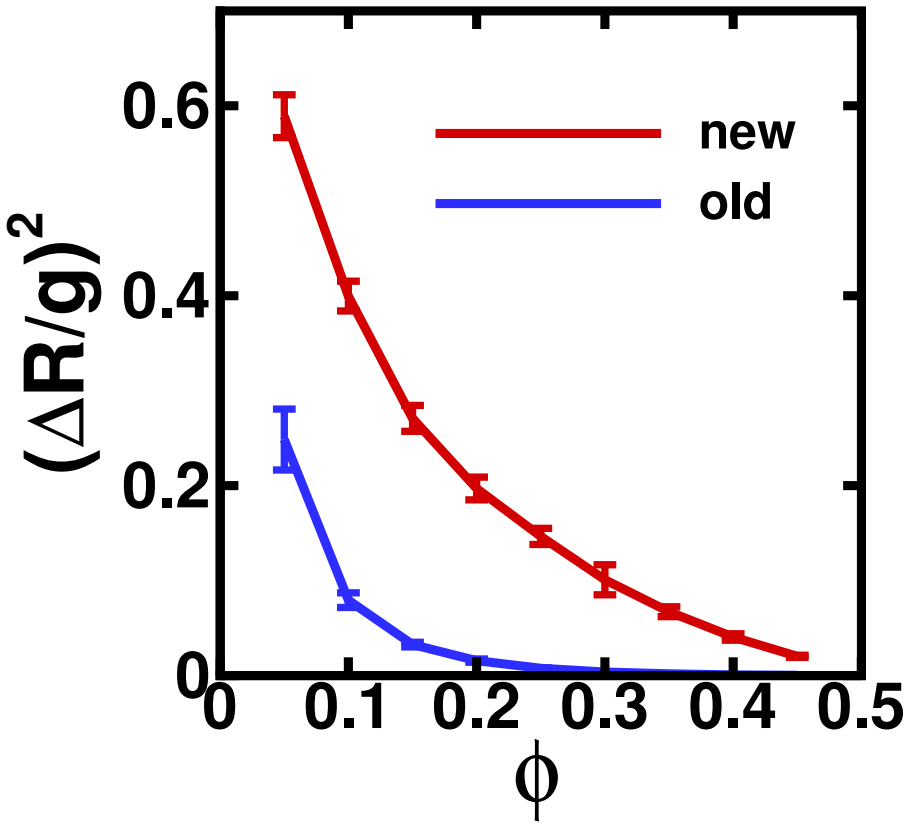

Figure 5.11: Comparison of $(\frac{\Delta R}{g})^2$ from this method and the new method for the binary hard sphere liquid. The packing fraction ϕ goes from 0.05 to 0.45. The results of both methods are averaged over 5 unoptimized paths of $N = 108$ and $\Delta R = 108\sigma$. The figure shows that paths generated by the new method in Chapter 3 are shorter. The new method is therefore better.

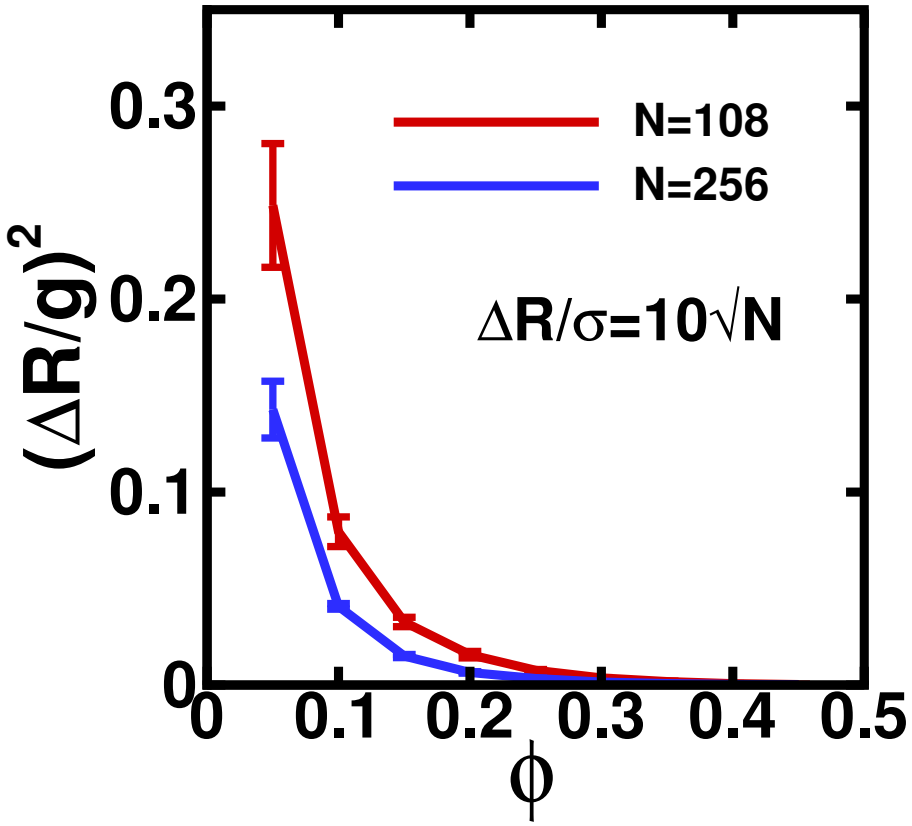

Figure 5.12: Comparison of $(\frac{\Delta R}{g})^2$ for different N with the old path finding method for the binary hard sphere liquid. The packing fraction ϕ goes from 0.05 to 0.45. The results are averaged over 5 unoptimized paths. The figure shows that the values of $(\frac{\Delta R}{g})^2$ are different for different N at the same density.

5.2.3 Analysis

From the procedure of finding a path in Section 5.2.1, we can see that the reason that this method does not work is that the motion is highly localized in the away step. The away step deals with one colliding pair at a time. Most of the system remains still in this step. So it is highly inefficient. The percentage of particles dealt with each time is smaller for bigger N. The increasing inefficiency for bigger N lead to longer paths and lower values of $(\frac{\Delta R}{g})^2$ for bigger N, which is what we see in Fig. 5.12. Fig. 5.13 shows that the participation ratio for different N, that bigger N has lower participation ratio, which shows that the paths generated by this method are more inefficient for bigger N.

The new method presented in Chapter 3, on the other hand, has both localized motion and macroscopic motion depending on the situation. The collision avoidance step in the new method can simultaneously deal with multiple overlaps, either multiple pairs of overlapping particles or any overlaps involving more than two particles. The ability of dealing with all the particles with overlaps at the same time of the collision avoidance step, without distinguishing among these overlaps, results in more efficient paths with major portions of particles participating in the overall path. The macroscopic motion in the overall path is shown in Fig. 5.14. In contrast to Fig. 5.13, the participation ratio does not change with different N with the new method.

Fig 5.15 shows the comparison of participation ratio n/N with this trial method and the new method for the binary hard sphere liquid. It shows that the new method has more efficient paths with a higher participation ratio.

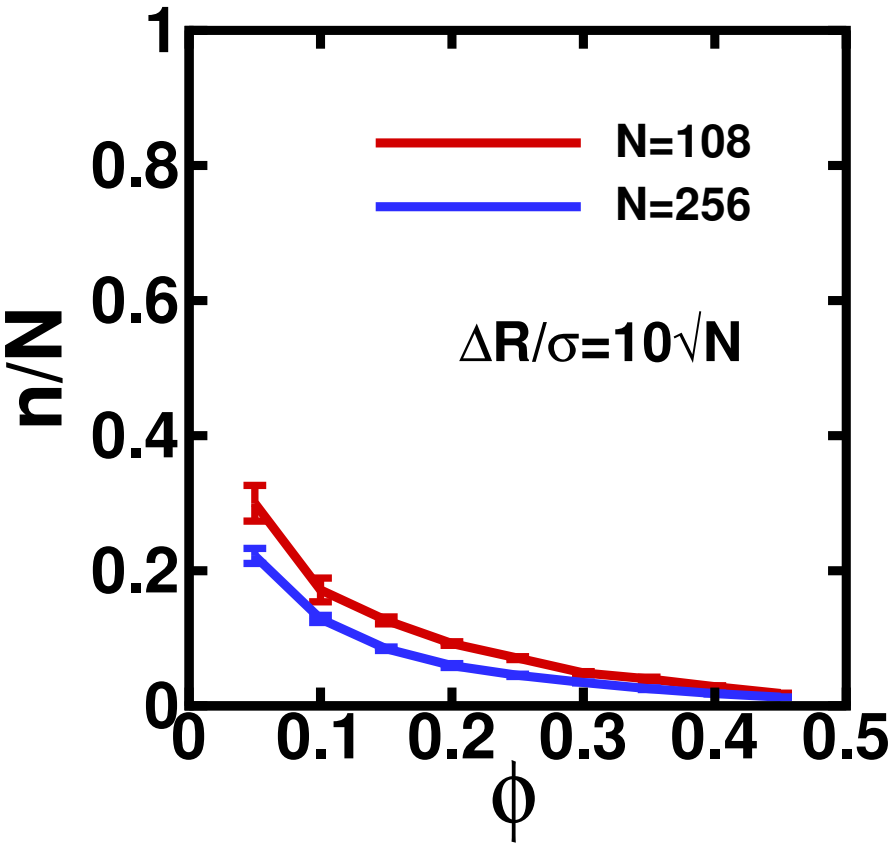

Figure 5.13: Comparison of participation ratios n/N for different N with the old path finding method for the binary hard sphere liquid. The packing fraction ϕ goes from 0.05 to 0.45. The results are averaged over 5 unoptimized paths. The figure shows that the participation ratio n/N is lower for bigger N with this method.

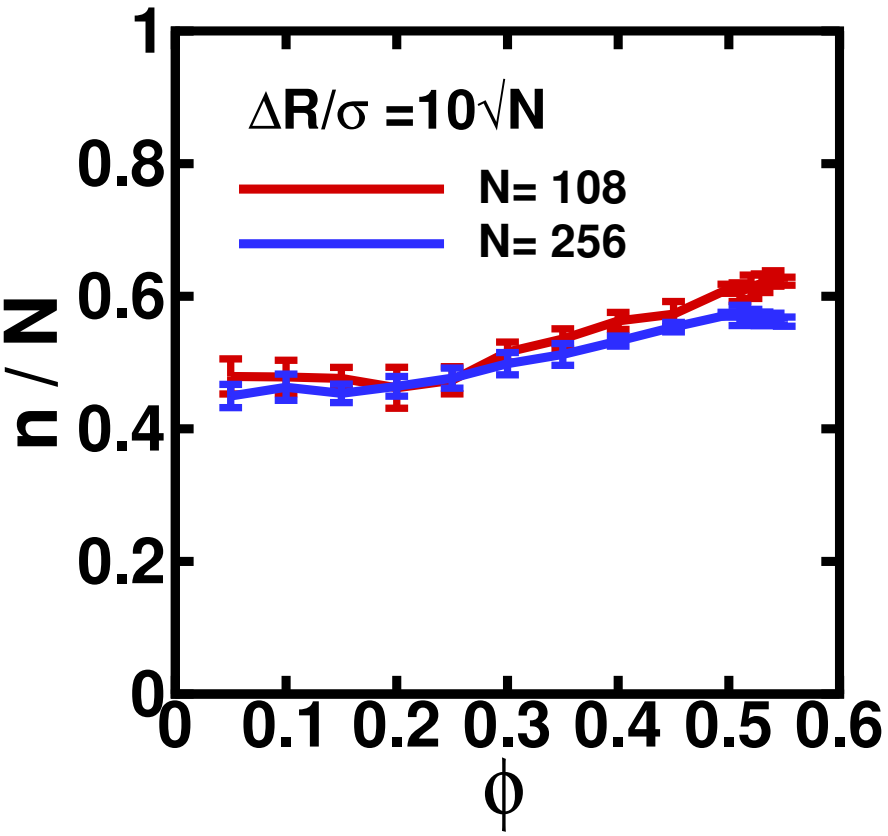

Figure 5.14: Comparison of participation ratios n/N for different N with the new path finding method shown in Chapter 3 for the binary hard sphere liquid. The figure is the same as Fig. 4.13 and is shown here for easy comparison. The packing fraction ϕ goes from 0.05 to 0.55. The results are averaged over 5 unoptimized paths. The figure shows that the participation ratio n/N does not depend on N with the new method.

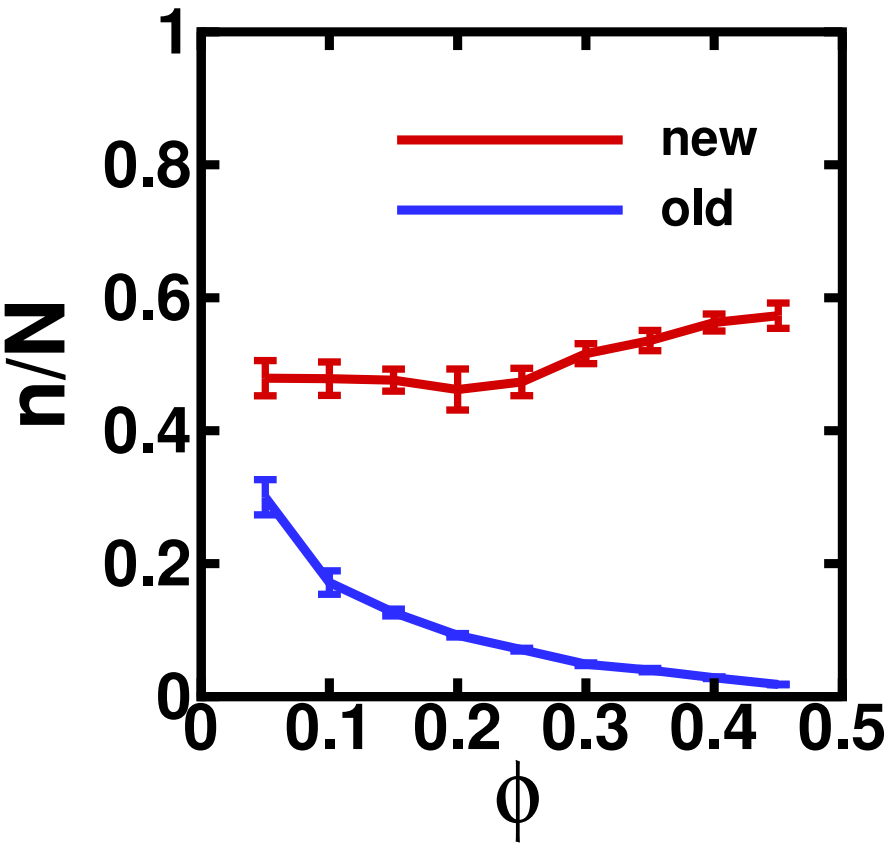

Figure 5.15: Comparison of participation ratios n/N from this method and the new method for the binary hard sphere liquid. The packing fraction ϕ goes from 0.05 to 0.45. The results are averaged over 5 unoptimized paths of $\Delta R = 108\sigma$ and $N = 108$ for both methods. The figure shows that the participation ratio n/N is higher with the new method.

Chapter 6

Concluding Remarks

What is intrinsic dynamics of a system? From the geodesic landscape perspective, geodesics are the inherent dynamics of a system. The principal path a system takes through the potential energy landscape becomes longer when the temperature drops for soft sphere liquids or the density increases for hard sphere liquids. The length of the principal path increasing is the cause of dynamics slowing down. The potential energy landscape ensemble provides us a useful tool to investigate paths through the potential energy landscape. Within this ensemble, the principal path a system takes is the shortest path with respect to the kinematical metric $g_{\mu\nu}$, and the potential energy along the path cannot exceed a certain landscape energy.

By studying the geodesics of hard sphere liquids, we have shown that geodesics explain why dynamics slows down for hard sphere liquids. It also contains information about other dynamic features such as dynamic heterogeneity. Previous study has shown that geodesics account for the dynamics slowing down for soft sphere liquids as well. But in the case of hard sphere liquids, there is absolutely no barrier-hopping in the potential energy landscape. The sole question is then whether the lengthier pathways account for slower dynamics. The answer is yes. The path length is all we need to explain the decrease in diffusion coefficients across multiple orders of magnitude for both soft and hard sphere liquids. The difference in the potential energy

landscapes between soft particle liquids and hard sphere liquids also reflects in the different details of the geodesics. The locality of the hard sphere potential energy leads to existence of both few-particle moves and many-particle moves in the geodesics of hard sphere liquids.

The traditional landscape approaches focus on the local minima and transitions between basins. But a potential energy landscape is more than the stationary points. By studying the hard sphere liquids, whose landscape does not have any local minima, we prove that what determines the rate of dynamics is the global topological feature - the shortest path lengths. Some other features of the landscape has been studied. In [17, 60], Kim, Chowdhary and Keyes emphasized the role of borders of basins in dynamics. In the point of view of geodesics, the reason that the borders are important is not the associated basins or saddle points, but is that the geodesics are close to the borders, because most configurations lie close to the boundaries in the potential energy landscape ensemble. Geodesics also provide insight into the phenomenon that the change of dynamic length scale is more pronounced than that of static length scale in glassy dynamics. While the static length scale focuses on the correlation between two static configuration points, the dynamic length scales focuses on the correlation between paths among configurations, and these paths are getting longer when system are deeper in glassy region.

The thesis has studied in detail the geodesics of hard sphere liquids and its implication for dynamics. Geodesic theory has been proven a useful tool to study liquid dynamics. The dynamical phenomena it predicts include dynamic slowing down [33, 61], dynamic heterogeneity [61], divergence of relaxation rates of translation and rotation [38], preferential solvation [39]. In future it could be applied to study other glassy problems such as percolation transition of configuration space and problems of other glassy systems.

Bibliography

[1] Andrea Cavagna. Supercooled liquids for pedestrians. *Physics Reports*, 476(4-6):51–124, June 2009.

[2] Elijah Flenner and Grzegorz Szamel. Dynamic heterogeneities above and below the mode-coupling temperature: evidence of a dynamic crossover. *The Journal of Chemical Physics*, 138(12):12A523, March 2013.

[3] Allen M.P. and Tildesley D.J. *Computer Simulation of Liquids*, chapter 2. Oxford University Press Inc., New York, 1987.

[4] Ludovic Berthier and Giulio Biroli. Theoretical perspective on the glass transition and amorphous materials. *Reviews of Modern Physics*, 83:587–645, June 2011.

[5] Michael Vogel and Sharon C. Glotzer. Spatially heterogeneous dynamics and dynamic facilitation in a model of viscous silica. *Physical Review Letters*, 92(25):255901, June 2004.

[6] Sharon C. Glotzer. Spatially heterogeneous dynamics in liquids: insights from simulation. *Journal of Non-Crystalline Solids*, 274(1-3):342–355, September 2000.

[7] Asaph Widmer-Cooper and Peter Harrowell. On the study of collective dynamics in supercooled liquids through the statistics of the isoconfigurational ensemble. *The Journal of Chemical Physics*, 126(15):154503, April 2007.

[8] D. Johnston. Stretched exponential relaxation arising from a continuous sum of exponential decays. *Physical Review B*, 74(18):184430, November 2006.

[9] Communication: Fast and local predictors of the violation of the Stokes-Einstein law in polymers and supercooled liquids. *The Journal of Chemical Physics*, 136(21):211101, June 2012.

[10] N. Lačević, F. W. Starr, T. B. Schrøder, and S. C. Glotzer. Spatially heterogeneous dynamics investigated via a time-dependent four-point density correlation function. *The Journal of Chemical Physics*, 119(14):7372, 2003.

[11] Gerold Adam and Julian H. Gibbs. On the temperature dependence of cooperative relaxation properties in glass-forming liquids. *The Journal of Chemical Physics*, 43(1):139–146, 1965.

[12] Magnus N. J. Bergroth, Michael Vogel, and Sharon C. Glotzer. Examination of dynamic facilitation in molecular dynamics simulations of glass-forming liquids. *The Journal of Physical Chemistry B*, 109(14):6748–53, April 2005.

[13] Claudio Donati, Jack F. Douglas, Walter Kob, Steven J. Plimpton, Peter H. Poole, and Sharon C. Glotzer. Stringlike cooperative motion in a supercooled liquid. *Physical Review Letters*, 80:2338–2341, Mar 1998.

[14] T. Keyes and J. Chowdhary. Inherent-structure dynamics and diffusion in liquids. *Physical Review E*, 64(3):032201, August 2001.

[15] B. Doliwa and A. Heuer. Energy barriers and activated dynamics in a supercooled Lennard-Jones liquid. *Physical Review E*, 67(3):030501, March 2003.

[16] Andreas Heuer. Exploring the potential energy landscape of glass-forming systems: from inherent structures via metabasins to macroscopic transport. *Journal of Physics. Condensed Matter*, 20(37):373101, September 2008.

[17] T. Keyes and J. Chowdhary. Potential energy landscape and mechanisms of diffusion in liquids. *Physical Review E*, 65(4):041106, April 2002.

[18] Thomas B. Schrøder, Srikanth Sastry, Jeppe C. Dyre, and Sharon C. Glotzer. Crossover to potential energy landscape dominated dynamics in a model glass-forming liquid. *The Journal of Chemical Physics*, 112(22):9834, 2000.

[19] David R. Reichman and Patrick Charbonneau. Mode-coupling theory. *Journal of Statistical Mechanics: Theory and Experiment*, 2005(05):P05013, 2005.

[20] Gary L. Hunter and Eric R. Weeks. The physics of the colloidal glass transition. *Reports on progress in physics. Physical Society (Great Britain)*, 75(6):066501, June 2012.

[21] Hans C. Andersen, John D. Weeks, and David Chandler. Relationship between the Hard-Sphere Fluid and Fluids with Realistic Repulsive Forces. *Physical Review A*, 4:1597–1607, Oct 1971.

[22] Ning Xu, Thomas K. Haxton, Andrea J. Liu, and Sidney R. Nagel. Equivalence of Glass Transition and Colloidal Glass Transition in the Hard-Sphere Limit. *Physical Review Letters*, 103:245701, Dec 2009.

[23] G. Brambilla, D. El Masri, M. Pierno, L. Berthier, L. Cipelletti, G. Petekidis, and A. Schofield. Probing the Equilibrium Dynamics of Colloidal Hard Spheres above the Mode-Coupling Glass Transition. *Physical Review Letters*, 102(8):085703, February 2009.

[24] Elijah Flenner, Min Zhang, and Grzegorz Szamel. Analysis of a growing dynamic length scale in a glass-forming binary hard-sphere mixture. *Physical Review E*, 83(5):051501, May 2011.

[25] Chaoming Song, Ping Wang, and Hernán A. Makse. A phase diagram for jammed matter. *Nature*, 453(7195):629–32, May 2008.

[26] Carolina Brito and Matthieu Wyart. Heterogeneous dynamics, marginal stability and soft modes in hard sphere glasses. *Journal of Statistical Mechanics: Theory and Experiment*, 2007(08):L08003–L08003, August 2007.

[27] Antina Ghosh, Vijayakumar Chikkadi, Peter Schall, and Daniel Bonn. Connecting Structural Relaxation with the Low Frequency Modes in a Hard-Sphere Colloidal Glass. *Physical Review Letters*, 107(18):188303, October 2011.

[28] Chandan Dasgupta and Oriol Valls. Free energy landscape of a dense hard-sphere system. *Physical Review E*, 59(3):3123–3134, March 1999.

[29] M. Schmiedeberg, T. K. Haxton, S. R. Nagel, and A. J. Liu. Mapping the glassy dynamics of soft spheres onto hard-sphere behavior. *EPL (Europhysics Letters)*, 96(3):36010, 2011.

[30] Thomas K. Haxton, Michael Schmiedeberg, and Andrea J. Liu. Universal jamming phase diagram in the hard-sphere limit. *Physical Review E*, 83:031503, March 2011.

[31] K. K. Mon. Hard sphere perturbation theory for thermodynamics of soft-sphere model liquid. *The Journal of Chemical Physics*, 115(10):4766–4769, 2001.

[32] Chengju Wang and Richard M. Stratt. Global perspectives on the energy landscapes of liquids, supercooled liquids, and glassy systems: the potential energy landscape ensemble. *The Journal of Chemical Physics*, 127(22):224503, December 2007.

[33] Chengju Wang and Richard M. Stratt. Global perspectives on the energy landscapes of liquids, supercooled liquids, and glassy systems: geodesic pathways through the potential energy landscape. *The Journal of Chemical Physics*, 127(22):224504, December 2007.

[34] L. Onsager and S. Machlup. Fluctuations and irreversible processes. *Phys. Rev.*, 91:1505–1512, September 1953.

[35] S. Machlup and L. Onsager. Fluctuations and irreversible process. ii. systems with kinetic energy. *Phys. Rev.*, 91:1512–1515, Sep 1953.

[36] Katharine L. C. Hunt and John Ross. Path integral solutions of stochastic equations for nonlinear irreversible processes: The uniqueness of the thermodynamic lagrangian. *The Journal of Chemical Physics*, 75(2):976–984, 1981.

[37] Paul M. Hunt, Katharine L. C. Hunt, and John Ross. Path integral solutions for fokkerplanck conditional propagators in nonequilibrium systems: Catastrophic divergences of the onsagermachluplaplace approximation. *The Journal of Chemical Physics*, 79(8):3765–3772, 1983.

[38] Daniel Jacobson and Richard M. Stratt. The inherent dynamics of a molecular liquid: geodesic pathways through the potential energy landscape of a liquid of linear molecules. *The Journal of Chemical Physics*, 140(17):174503, May 2014.

[39] Crystal N. Nguyen and Richard M. Stratt. Preferential solvation dynamics in liquids: how geodesic pathways through the potential energy landscape reveal mechanistic details about solute relaxation in liquids. *The Journal of Chemical Physics*, 133(12):124503, September 2010.

[40] Ashwin S S and Srikanth Sastry. Low-temperature behaviour of the Kob-Andersen binary mixture. *Journal of Physics: Condensed Matter*, 15(11):S1253, 2003.

[41] Søren Toxvaerd and Jeppe C. Dyre. Role of the first coordination shell in determining the equilibrium structure and dynamics of simple liquids. *The Journal of Chemical Physics*, 135(13):–, 2011.

[42] Walter Kob, Claudio Donati, Steven J. Plimpton, Peter H. Poole, and Sharon C. Glotzer. Dynamical heterogeneities in a supercooled Lennard-Jones liquid. *Physical Review Letters*, 79:2827–2830, Oct 1997.

[43] Claudio Donati, Sharon C. Glotzer, Peter H. Poole, Walter Kob, and Steven J. Plimpton. Spatial correlations of mobility and immobility in a glass-forming lennard-jones liquid. *Physical Review E*, 60:3107–3119, September 1999.

[44] Walter Kob and Hans C Andersen. Testing mode-coupling theory for a supercooled binary Lennard-Jones mixture I: The van Hove correlation function. *Physical Review E*, 51(5), May 1995.

[45] Walter Kob and Hans C. Andersen. Testing mode-coupling theory for a supercooled binary Lennard-Jones mixture. II. Intermediate scattering function and dynamic susceptibility. *Physical Review E*, 52:4134–4153, October 1995.

[46] Adby P. R. and Demspter M. A. H. *Introduction to Optimization Methods*, chapter 5. Chapman and Hall, London, 1974.

[47] Allen M.P. and Tildesley D.J. *Computer Simulation of Liquids*, chapter 3. Oxford University Press Inc., New York, 1987.

[48] Srikanth Sastry, Thomas M. Truskett, Pablo G. Debenedetti, Salvatore Torquato, and Frank H. Stillinger. Free volume in the hard sphere liquid. *Molecular Physics*, 95(2):289–297, 1998.

[49] Morrel H. Cohen and David Turnbull. Molecular transport in liquids and glasses. *The Journal of Chemical Physics*, 31(5):1164–1169, 1959.

[50] David Turnbull and Morrel H. Cohen. On the free volume model of the liquid glass transition. *The Journal of Chemical Physics*, 52(6):3038–3041, 1970.

[51] Martin Goldstein. Some thermodynamic aspects of the glass transition: Free volume, entropy, and enthalpy theories. *The Journal of Chemical Physics*, 39(12):3369–3374, 1963.

[52] Francis W. Starr, Srikanth Sastry, Jack F. Douglas, and Sharon C. Glotzer. What do we learn from the local geometry of glass-forming liquids? *Physical Review Letters*, 89:125501, August 2002.

[53] S. Williams and a. Philipse. Random packings of spheres and spherocylinders simulated by mechanical contraction. *Physical Review E*, 67(5):051301, May 2003.

[54] Allen M.P. and Tildesley D.J. *Computer Simulation of Liquids*, chapter 4. Oxford University Press Inc., New York, 1987.

[55] Elijah Flenner and Grzegorz Szamel. Relaxation in a glassy binary mixture: Comparison of the mode-coupling theory to a Brownian dynamics simulation. *Physical Review E*, 72(3):031508, September 2005.

[56] Allen M.P. and Tildesley D.J. *Computer Simulation of Liquids*, chapter 6. Oxford University Press Inc., New York, 1987.

[57] D Weaire and A. R. Williams. New numerical approach to the Anderson localization problem. *Journal of Physics C: Solid State Physics*, 9:461, 1976.

[58] Steven W. Smith, Carol K. Hall, and Benny D. Freeman. Molecular dynamics study of transport coefficients for hard-chain fluids. *The Journal of Chemical Physics*, 102(2):1057, 1995.

[59] H.Sigurgeirsson and D.M.Heyes. Transport coefficients of hard sphere fluids. *Molecular Physics*, 101(3):469–482, 2003.

[60] Joohyun Kim and T. Keyes. On the mechanism of reorientational and structural relaxation in supercooled liquids: the role of border dynamics and cooperativity. *The Journal of Chemical Physics*, 121(9):4237–45, September 2004.

[61] Qingqing Ma and Richard M. Stratt. Potential energy landscape and inherent dynamics of a hard-sphere fluid. *Physical Review E*, 90(4):042314, October 2014.